Dissertation

submitted to the

Combined Faculties of the Natural Sciences and Mathematics

of the

Ruperto-Carola-University of Heidelberg, Germany

for the degree of

Doctor of Natural Sciences

Put forward by

Alexander Egl

born in Aschaffenburg

Oral examination: April 22, 2020

High-Precision Laser Spectroscopy of the Fine Structure in $^{40}Ar^{13+}$ at ALPHATRAP

Referees:

Prof. Dr. Klaus Blaum
Prof. Dr. Selim Jochim

Hochpräzise Laserspektroskopie der Feinstruktur von hochgeladenem $^{40}Ar^{13+}$ an ALPHATRAP

Ziel des kryogenen Penningfallenexperimentes ALPHATRAP ist der Test der Quantenelektrodynamik gebundener Zustände (BS-QED) durch Messungen des magnetischen Moments (g-Faktor) von Elektronen in schweren hochgeladenen Ionen (HCI). Der g-Faktor im gebundenen Zustand wird mit der Doppelfallenmethode bestimmt, die auf dem kontinuierlichen Stern-Gerlach Effekt (CSGE) für eine nicht destruktive Detektion des Spinzustandes des Ions basiert. In dieser Arbeit werden zwei Ergebnisse präsentiert. Um die Genauigkeit zukünftiger Messungen zu erhöhen, ist die Implementierung von sympathetischem Laserkühlen geplant. Hierzu wurde ein Lasersystem in den bestehenden experimentellen Aufbau integriert und die Laserkühlung von $^{9}Be^{+}$ erstmalig in ALPHATRAP demonstriert. Für die axiale Temperatur eines einzelnen Berylliumions kann ein oberer Grenzwert von 69(30) mK gegeben werden. Dies bereitet den Weg für zukünftige Entwicklungen in Richtung von sympathetischem Laserkühlen an hochgeladenen Ionen. Darüber hinaus wurde der optische Zugang zur Falle für hochpräzise Laserspektroskopie an $^{40}Ar^{13+}$ genutzt. Die Absolutfrequenz des magnetischen Dipolübergangs der Feinstruktur im Grundzustand von borähnlichem Argon wurde mit einer unübertroffenen relativen Genauigkeit von 9.4×10^{-9} gemessen. Hierzu wurde eine neuartige Spektroskopiemethode verwendet, die den CSGE nutzt und keiner Fluoreszenzdetektion bedarf. Das hier gezeigte Prinzip kann auch auf andere Systeme angewandt werden und eröffnet somit neue Möglichkeiten zum Test von BS-QED in stärksten elektromagnetischen Feldern durch Untersuchung der Hyperfeinstruktur von schweren HCI im optischen Bereich mittels Laserspektroskopie.

High-Precision Laser Spectroscopy of the Fine Structure in $^{40}Ar^{13+}$ at ALPHATRAP

The cryogenic double Penning-trap experiment ALPHATRAP aims to test bound-state quantum electrodynamics (BS-QED) under extreme conditions by measuring the magnetic moment (g-factor) of electrons bound to the nucleus of heavy highly charged ions (HCIs). The bound electron g-factor is measured employing the double-trap technique which uses the continuous Stern-Gerlach effect (CSGE) for a nondestructive detection of the spin state of the ion. The result of this thesis is twofold.
In order to improve the achievable precision of future measurements the implementation of sympathetic laser cooling is envisaged. For this purpose a laser system was integrated into the existing setup and laser cooling of $^{9}Be^{+}$ was demonstrated for the first time at ALPHATRAP. For the axial temperature of a single beryllium ion an upper limit of 69(30) mK can be given. This demonstration paves the way for further developments towards sympathetic laser cooling of HCIs.
Furthermore, the optical access to the Penning trap was used for high-precision laser spectroscopy of the magnetic dipole fine structure transition in the ground state of boronlike argon $^{40}Ar^{13+}$ with an unsurpassed relative uncertainty of the absolute frequency of 9.4×10^{-9}. To this end, a novel spectroscopy scheme was demonstrated for the first time, which uses the CSGE and does not require a detection of fluorescence. This proof-of-principle method can be extended to other systems, opening up new possibilities to test BS-QED in the strongest electromagnetic fields by investigating the optical hyperfine structure in heavy HCI by means of laser spectroscopy.

Contents

List of Figures

List of Tables

1. Introduction

The Standard Model (SM) of physics is the most complete description of the universe we live in. Besides gravity, which is represented by general relativity and resists to be incorporated into the quantum field theoretical framework of the SM (to form a coherent theory describing all physical aspects of nature), three fundamental interactions, their symmetries, fundamental constants and all elementary particles are the base for the Standard Model. In the SM, the three different interactions of the electromagnetic, the weak, and the strong force between particles are described by quantum field theories, namely the quantum electrodynamic (QED), which is unified with the weak interaction to the electroweak interaction and the quantum chromodynamic (QCD). Although the SM is to the present day the most successful theory of particle physics, it falls short of explaining some observed phenomena. In particular, cosmological observations regarding the energy content of the universe, the unknown nature of dark matter and dark energy, as well as the asymmetry between matter and antimatter during baryogenesis [1] in the observed universe, are not adequately explained. Furthermore, the observation of neutrino oscillations [2] that give neutrinos a nonzero mass contradicts expectations from the SM. This motivates further tests of the validity of SM predictions and inspires a large range of experiments to challenge the SM in different regimes and conditions. One approach is to test theory by studying particle collisions at highest energies as done at the Large Hadron Collider at CERN. Another way is to test theory at low energies but with highest precision, which can be possible even with small scale or tabletop experimental setups.

Out of three quantum field theories of the SM, the most stringently tested one is the QED [3, 4]. Among the earliest success of the QED was the explanation of the observed Lamb shift in the fine structure of the $n = 2$ level in atomic hydrogen [5] and observed deviation [6, 7] of the electron g-factor from the value of exactly 2, as predicted by Dirac [8] for the case of a free point particle using relativistic quantum theory[1]. QED, which describes the interaction between light and matter, is verified to highest precision in different regimes and physical systems. In the framework of QED, the structure and properties of atoms and ions can be predicted with extraordinary precision. In order to test the theory, specific observables are particularly suitable for measurements.

One of them is the magnetic moment of the electron, either for a free electron, sec. 1.1.1 or for one bound to a nucleus in highly charged ions (HCIs), sec. 1.1.2. The determination of the magnetic moment of the bound electron with unrivaled precision and in a yet unexplored regime of heavy HCIs is the main goal of the Alphatrap experiment [9]. Alphatrap is a cryogenic double Penning-trap experiment, aiming for high-precision

[1] This is equivalent to 0^{th} order of perturbation theory of QED.

measurements of the magnetic moment of electrons bound in HCIs. The design of the experiment allows the external injection of ions produced by dedicated external sources, e.g. electron beam ion traps (EBITs). Having access to heavy highly charged ions extends the available electromagnetic field strength by two orders of magnitude compared to previous experiments, see left side of fig. 1.1. The comparison to the theory constitutes a rigorous test of the SM in extremely strong electromagnetic fields. Even though the magnetic moment of the bound electron differs significantly from the one of the free electron or in different HCI with respect to the achievable precision, the absolute value does not change severely over the whole periodic table, see right side of fig. 1.1. For example in hydrogenlike HCIs, the deviation from the free electron value is dominated by the interaction with the Coulomb potential of the nucleus, see sec. 1.1.2. This leads to values ranging from $g_J \approx 2.00$ for light ions such as $^{12}C^{5+}$ decreasing down to $g_J \approx 1.66$ for $^{238}U^{92+}$ [10].

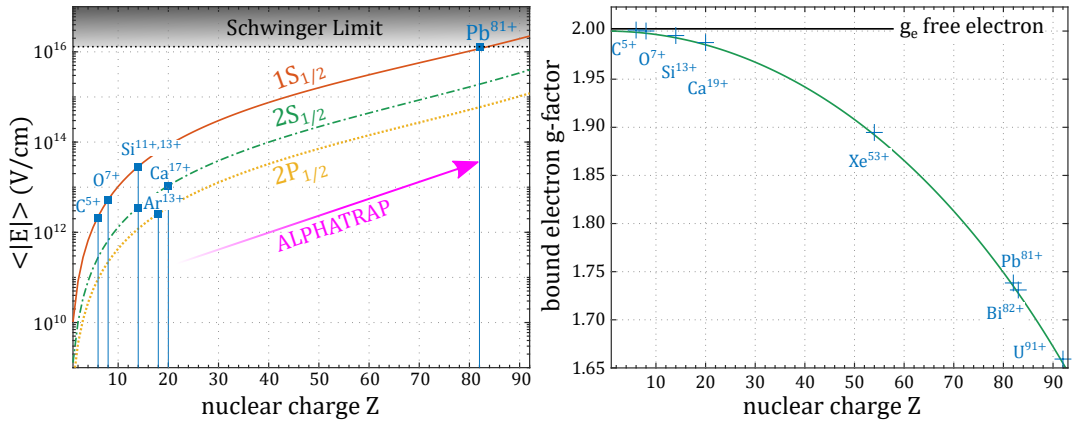

Figure 1.1.: Mean electric field strength and bound-state g-factor in hydrogenlike ions. **left** Expectation value for the electric field strength in different orbitals. Relativistic values are calculated according to [10, 11]. Highlighted are selected so far measured systems and the projected hydrogenlike lead $^{208}Pb^{81+}$, for which the expectation value reaches the Schwinger limit. **right** Bound state electron g-factor g_j for hydrogenlike ions. The markers show measured experimental values, taken from [12]. The solid line shows the prediction from the dominant Breit term, for details see text.

This situation is fundamentally different for a second type of observables, such as the transition energies between different electronic states in the ion. Here, transitions of different types exhibit a scaling behavior with the charge state $Z_i = Z - N_e$, given by the nuclear charge or proton number Z and the number of the remaining, bound electrons N_e. For few electron systems, energies of principal transitions are roughly proportional to Z_i^2 which shifts them to the extreme ultraviolet or x-ray regime and therefore can-

not be used for laser spectroscopy[2]. Similarly, also the transition energies of hyperfine structure (HFS) and fine structure (FS) transitions scale roughly with Z_i^3 and Z_i^4, respectively, cf. fig. 1.2 [12]. As a consequence, FS and HFS transitions become shifted

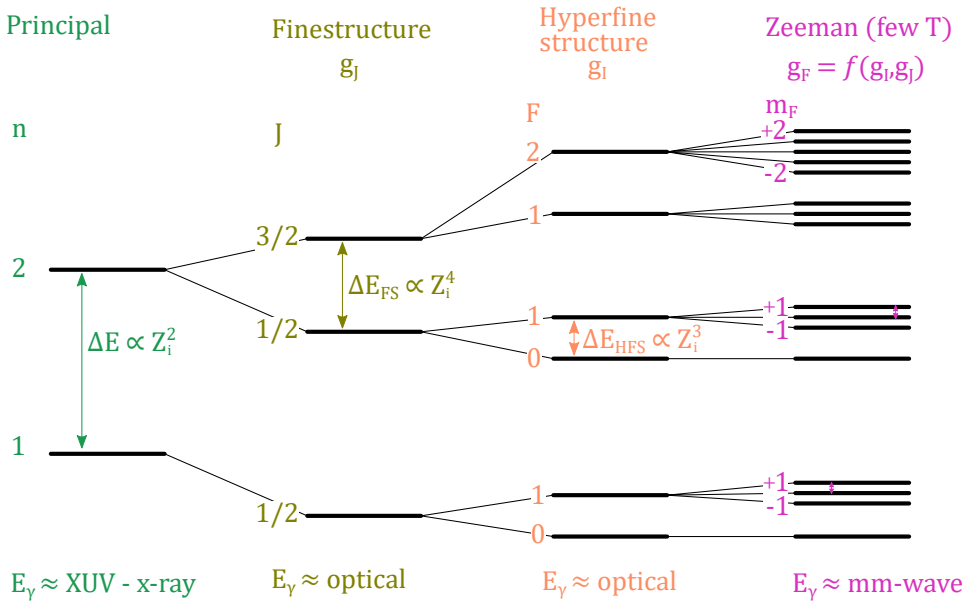

Figure 1.2.: Exemplary level scheme for a highly charged ion ($I = 1/2$) showing a hyperfine structure. The corresponding photon energies are stated at the bottom. Apart from the principal transition, they are all magnetic dipole (M1) transitions. Energy not to scale.

into the optical regime depending on the charge state of the HCI and are thus accessible for laser spectroscopy (see sec. 1.2). Because both of those transitions are electric dipole forbidden, the radiative lifetimes are long and the natural linewidth is narrow. In this thesis, a novel spectroscopy method is presented which allows to investigate such transitions.

1.1. Millimeter Wave Spectroscopy of HCI

The most precise measurements for tests of QED so far are done with either electrons [3] or ions [4] stored in Penning traps. By measuring the frequencies of the motion of the trapped particle with highest precision, information about the intrinsic properties or the quantum state of the particle can be interfered. Common to the type of measurements performed with electrons or ions in Penning traps is the use of electromagnetic

[2]However, those transitions are routinely measured with x-ray spectroscopy by observing discharges in plasmas or excitation of HCI using synchrotrons as light sources.

radiation for probing different transitions. In the case of the determination of the g-factor the relevant transition frequency is the Larmor frequency of the electron in the external magnetic trapping field. It is of order $\mathcal{O}(10 - 100$ GHz), whereas HFS and FS transition in certain HCI can be shifted into a frequency range accessible for lasers, $\mathcal{O}(100 - 1000$ THz). Even though the principles of these measurements are similar, the conclusions and physical effects which are addressed might be different, as it will be outlined in the following sections.

1.1.1. The Free Electron *g*-factor

The g-factor $g_{\mathrm{e}}^{\mathrm{free}}$ of the free electron relates the magnetic moment of the electron $\vec{\mu}_e$, in units of the Bohr magneton μ_{B}, to its intrinsic spin angular momentum $\vec{S}$:

$$\vec{\mu}_e = -g_{\mathrm{e}}^{\mathrm{free}} \frac{e}{2m_{\mathrm{e}}} \vec{S} = -g_{\mathrm{e}}^{\mathrm{free}} \mu_{\mathrm{B}} \frac{\vec{S}}{\hbar}, \tag{1.1}$$

where e is the elementary charge m_{e} the electron rest mass and $\hbar$ the reduced planck constant. The deviation compared to the value of exactly 2 from Dirac theory is referred to as the *anomalous magnetic moment* of the electron and can be expressed as $a_{\mathrm{e}} = (g-2)/2$. Within the SM, this value can be calculated with extraordinary precision and has contributions arising from QED, hadronic and electroweak interactions:

$$a_{\mathrm{e}} = \frac{g-2}{2} = \Delta a_{\mathrm{e}}^{\mathrm{QED}} + \Delta a_{\mathrm{e}}^{\mathrm{hadr}} + \Delta a_{\mathrm{e}}^{\mathrm{electroweak}}. \tag{1.2}$$

However, additional yet unknown interactions beyond the SM, $\Delta a_{\mathrm{e}}^{\mathrm{new}}$, could affect the anomalous magnetic moment, $\tilde{a}_{\mathrm{e}} = a_{\mathrm{e}} + a_{\mathrm{e}}^{\mathrm{new}}$. Within the achievable precision, this allows to search for effects not described by the SM. The first correction term of QED for the g-factor of the free electron was derived by Schwinger [13] and is due to the virtual emission and re-absorption of a photon by the electron. This effect is called Schwinger or vertex correction and besides the vacuum polarization, the creation of virtual electron and positron pairs, it is the dominant contribution. This and higher order corrections can be represented in Feynman diagrams, see fig. 1.3. The contribution of QED to the anomalous magnetic moment, $\Delta a_{\mathrm{e}}^{\mathrm{QED}}$, can be calculated perturbatively in a series expansion in orders of $\left(\frac{\alpha}{\pi}\right)$ [15]:

$$\Delta a_{\mathrm{e}}^{\mathrm{QED}} = \sum_{n=1}^{\infty} a_{\mathrm{e}}^{(2n)} \left(\frac{\alpha}{\pi}\right)^n. \tag{1.3}$$

The strength of the fundamental electromagnetic interaction between charged particles is given by the dimensionless fine-structure constant $\alpha = \frac{e^2}{4\pi\epsilon_0\hbar c} \approx \frac{1}{137.036}$, where ϵ_0 is the vacuum permittivity and c the speed of light in vacuum. The coefficients $a_{\mathrm{e}}^{(2n)}$ take the QED contributions from two other leptons, the muon (μ) and tau (τ) into account, which is reflected in a mass independent and lepton-mass dependent part [14]:

$$a_{\mathrm{e}}^{(2n)} = A_1^{(2n)} + A_2^{(2n)}\left(m_{\mathrm{e}}/m_\mu\right) + A_2^{(2n)}\left(m_{\mathrm{e}}/m_\tau\right) + A_3^{(2n)}\left(m_{\mathrm{e}}/m_\mu, m_{\mathrm{e}}/m_\tau\right). \tag{1.4}$$

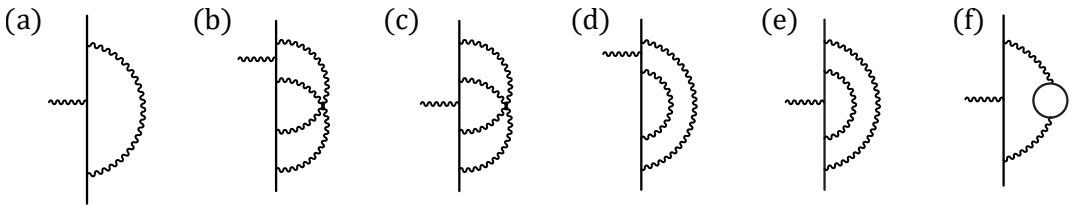

Figure 1.3.: Feynman diagram representation of different QED contributions to the free electron g-factor. The time axis is vertically orientated. The straight line represents the propagator for the free electron, virtual photons are represented by wavy lines. **a** Feynman diagram for the second order, one photon-loop correction of the electron. **b-f** All Feynman diagrams for the fourth-order corrections, including the time-reversal symmetric diagrams of (b) and (d). Figure modified from [14].

The coefficients $a_e^{(2n)}$ can be given analytically up to eighth-order, whereas higher orders need to be evaluated numerically. Up to now, these corrections have been calculated up to tenth order[3] [15]. The value of these calculations depends on the precise knowledge of the fine-structure constant α. The most precise values for α are currently measured in photon recoil experiments with rubidium [16, 17] or caesium atoms [18] :

$$\alpha_{\mathrm{Rb}}^{-1} = 137.035\ 998\ 995\ (85), \tag{1.5a}$$

$$\alpha_{\mathrm{Cs}}^{-1} = 137.035\ 999\ 046\ (27). \tag{1.5b}$$

Using these values and the contributions from the hadronic and weak interactions, cf. eq. (1.2), the theoretical value for a_e reads [19]:

$$a_e^{\mathrm{theo,Rb}} = 1\ 159\ 652\ 182.037\ (720)\ (11)\ (12) \times 10^{-12}, \tag{1.6a}$$

$$a_e^{\mathrm{theo,Cs}} = 1\ 159\ 652\ 181.606\ (229)\ (11)\ (12) \times 10^{-12}, \tag{1.6b}$$

where the uncertainties are due to the fine-structure constant α, the numerical evaluation of the tenth-order of eq. (1.3) and the hadronic contributions. These calculations are independently tested with highest precision in the famous electron $g-2$ Penning-trap experiment by Gabrielse *et al.* [3], yielding a value of:

$$a_e^{\mathrm{exp}} = 1\ 159\ 652\ 180.73\ (28) \times 10^{-12}. \tag{1.7}$$

This value deviates from theory, (1.6), by 1.7σ respectively 2.4σ of the combined uncertainties. However, eq. (1.2) can also be used to extract a value for α from the measured

[3]The number of Feynman diagram which need to be evaluated is growing dramatically with the order. For the tenth order, $a_e^{(10)} \left(\frac{\alpha}{\pi}\right)^5$, 12672 diagrams have to be calculated.

anomalous magnetic moment, eq. (1.7). Therefore, the Penning-trap measurement allows for an independent comparison of the experimental values for the fine-structure constant which results in [3]:

$$\alpha_{g-2}^{-1} = 137.035\,999\,084\,(51). \tag{1.8}$$

Even though experimental and theoretical values for the anomalous magnetic moment of the free electron agree to an astonishing precision, measurements of the g-factor of electrons bound in highly charged ions allow to address the question of the validity of QED in the regime of extremely strong electric and magnetic fields.

1.1.2. The Bound Electron *g*-factor

High-precision measurements of electron magnetic moments can also be performed under extreme conditions such as strong electric or magnetic fields. The strongest electromagnetic fields that can be found in a laboratory are in the vicinity of the nucleus of an atom. Therefore, electrons bound close to the nucleus experience the strongest fields that can be used in the laboratory up to date. The expectation value of the electric field strength experienced by an electron in the ground-state of hydrogen-, lithium- and boronlike HCI as a function of the nuclear charge Z is shown in fig. 1.1. As for the case of the free electron, the development of the bound-state quantum electrodynamic (BS-QED) allows calculation of the g-factor $g_\mathrm{e}^\mathrm{bound}$ of the electron bound in the Coulomb potential of a nucleus. The resulting contributions to the g-factor are then:

$$g_\mathrm{e}^\mathrm{bound} = g_\mathrm{Dirac}^\mathrm{bound} + \Delta g_\mathrm{BS\text{-}QED} + \Delta g_\mathrm{nucl} + \Delta g_\mathrm{int}, \tag{1.9}$$

where $g_\mathrm{Dirac}^\mathrm{bound}$ is the solution of the Dirac equation, $\Delta g_\mathrm{BS\text{-}QED}$ is the radiative correction in BS-QED and Δg_nucl includes all nuclear properties, such as the nuclear size, deformation, susceptibility, magnetic moment and recoil. Whereas the first three terms on the right hand side are sufficient for hydrogenlike systems, for few-electron systems an additional contribution from interelectron interactions, Δg_int, arises. The magnetic moment of the electron is not only altered by QED effects, but in addition the binding potential and properties of the nucleus will contribute to the overall value. The relative contributions are shown in fig. 1.4 and will be shortly summarized in the following sections. A detailed overview can be found e.g. in [10, 12].

For light ions up to $Z = 20$, g-factor measurements with hydrogen- and lithiumlike ions have been done at ALPHATRAP's predecessor experiment [4, 20–24] at the Johannes Gutenberg University Mainz, Germany. Since the ionization energy is $\propto Z^2$, the availability of the HCIs is limited by their production technique. At the Mainz experiment, the in-trap production did not allow to produce ions beyond lithiumlike calcium [25]. At ALPHATRAP, HCIs are externally produced in dedicated ion sources (sec. 3.1), which extends the accessible range towards heavy ions, enabling tests of QED at even higher field strengths [26]. In addition, at ALPHATRAP the g-factor in a boronlike system, $^{40}\mathrm{Ar}^{13+}$, has already been measured for the first time with high precision [27], allowing a test of many-electron, QED and nuclear-recoil contributions. The heaviest HCI projected to be measured in ALPHATRAP is hydrogenlike lead, $^{208}\mathrm{Pb}^{81+}$. In this system, the

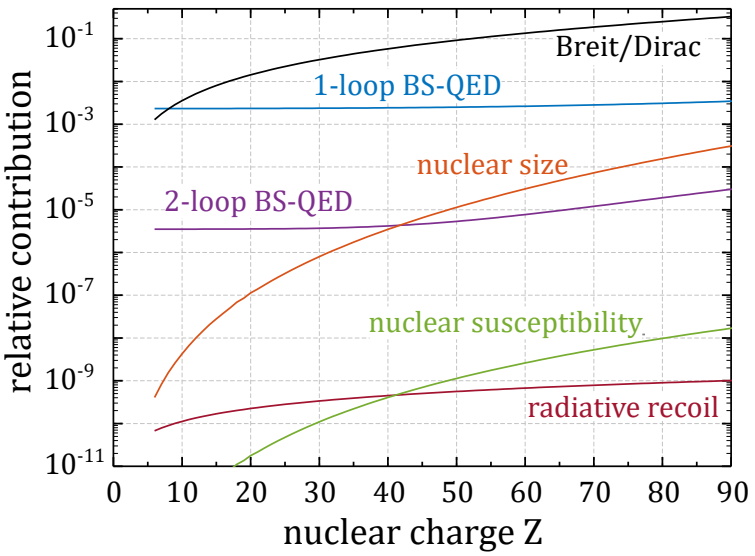

Figure 1.4.: Relative contributions to the g-factor of an electron bound in an hydrogenlike ion as function of the nuclear charge Z. For details, see text. Figure modified from [9].

mean electric field strength in the $1S_{1/2}$ ground state approaches the Schwinger limit. As predicted by Schwinger [28], at a homogeneous electric field of a critical strength $E_{\mathrm{crit}} = \frac{m_e c^3}{e\hbar} \approx 1.3{\times}10^{16}\mathrm{V/cm}$ spontaneous electron-positron pair production occurs[4]. As a major consequence of the binding to the nucleus, the coupling is now given by $(Z\alpha)$ instead of α only. Therefore, the perturbative approach, where a series expansion in orders of $(\frac{\alpha}{\pi})$ is done as for the free electron, breaks down for large Z. Depending on Z, two approaches turn out to be suitable:

1. In the low Z regime, such that $(Z\alpha) \ll 1$ still holds, a perturbative approach can be chosen similar to the case of the free electron, eq. (1.3). The QED interactions with the nucleus are taken into account separately, leading to a second series expansion in orders of $(Z\alpha)$ [9]. The convergence of this second series depends on the value of $Z\alpha$ and is mainly employed for low Z.

2. For larger Z, $Z\alpha \to 1$, this perturbative approximation breaks down and for the calculations all Feynman diagrams have to be evaluated[5]. For this ansatz, the QED propagator of the electron has to be a solution of the Dirac equation with an

[4] Whereas the critical value for $\langle |E_{\mathrm{crit}}| \rangle$ refers explicitly to homogeneous fields, this is not given in the Coulomb potential of the nucleus. This so-called supercritical field strength for nuclei is predicted to reach at $Z_{\mathrm{crit}} = 173$, see [29] and references therein.

[5] When talking about test of QED in strong fields, one typically refers to a regime in which the coupling $Z\alpha$ can no longer be considered a small perturbation.

added Coulomb potential caused by the charge distribution of the nucleus. This way an expansion in orders of $(Z\alpha)$ can be avoided. Even though this calculation is more complicated it is expected to be valid for all Z.

In addition, different corrections and contributions have to be taken into account:

Solution of the Dirac Equation with a Coulomb Potential – $g_{\mathbf{Dirac}}^{\mathbf{bound}}$

The analytic solution of the Dirac equation for an electron in the Coulomb potential of a hydrogenlike ion, in which the nucleus is assumed to be stationary (infinite mass) and pointlike, is referred to as the Furry picture [30]. It leads to a value $g_{\mathrm{Dirac}}^{\mathrm{bound}}$ for the electron magnetic moment significantly deviating from the Dirac value of $g_{\mathrm{Dirac}}^{\mathrm{free}} = 2$ for the free electron:

$$g_{\mathrm{Dirac}}^{\mathrm{bound}} = \frac{2}{3}\left[1 + 2\sqrt{1-(Z\alpha)^2}\right] = 2 - \frac{2}{3}(Z\alpha)^2 - \frac{1}{6}(Z\alpha)^4 - \mathcal{O}\left((Z\alpha)^{n\geq 6}\right). \tag{1.10}$$

This solution was first derived by Breit [31] and is therefore often called the *Breit term*. The Breit term makes up the largest contribution to the bound electron g-factor, see fig. 1.4. The leading term, $-\frac{2}{3}(Z\alpha)^2$, causes a deviation from the free electron g-factor of up to 15 % for hydrogenlike uranium ($Z = 92$), see fig. 1.1. The analytic solution for the ground state g-factor in lithiumlike $(2S_{1/2})$ and boronlike $(2P_{1/2})$ systems can be expanded analogously [12]:

$$g_{\mathrm{Dirac}}^{\mathrm{bound}}(2S_{1/2}) = 2 - \frac{1}{6}(Z\alpha)^2 - \frac{5}{96}(Z\alpha)^4 - \mathcal{O}\left((Z\alpha)^{n\geq 6}\right), \tag{1.11a}$$

$$g_{\mathrm{Dirac}}^{\mathrm{bound}}(2P_{1/2}) = \frac{2}{3} - \frac{1}{6}(Z\alpha)^2 - \frac{5}{96}(Z\alpha)^4 - \mathcal{O}\left((Z\alpha)^{n\geq 6}\right). \tag{1.11b}$$

Radiative Correction – $\Delta g_{\mathbf{BS\text{-}QED}}$

As for the free electron case, the Feynman diagrams representing the interaction of the electron can be adjusted taking also the interaction with the magnetic field into account. The diagrams can be grouped into different orders, reflecting the number of photon loops. The first six diagrams of the first order in $\left(\frac{\alpha}{\pi}\right)$ are shown in fig. 1.5. They are calculated to all orders of $Z\alpha$ within the Furry picture. Since each loop contributes another factor of α, higher orders contribute less. For the two-loop corrections of the second order, $\left(\frac{\alpha}{\pi}\right)^2$, 50 Feynman diagrams have to be evaluated, see fig. 21 in [10]. These diagrams are not completely calculated in all orders of $Z\alpha$ yet. For hydrogenlike ions they are calculated up to order $\alpha^2(Z\alpha)^5$ [32, 33] and constitute the dominant uncertainty of theoretical predictions.

Nuclear Effects – $\Delta g_{\mathbf{nucl}}$

While the nucleus in the above consideration was assumed to be pointlike and to have infinite mass, this approximation is no longer valid when going beyond the Furry picture of QED. In the Furry picture, a time-independent static external field is used to describe

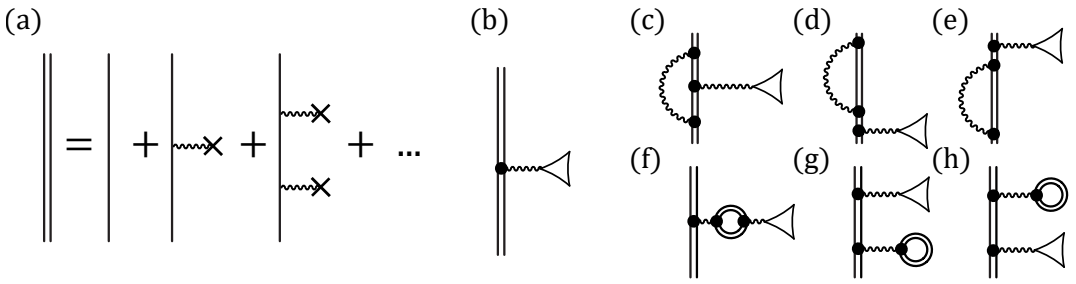

Figure 1.5.: Feynman diagrams for first order corrections of the bound electron. **a** The electron bound in the field of the nucleus is drawn as a double line. It is composed of the free electron propagator and the Coulomb interaction with the nucleus in all orders of $Z\alpha$. **b** The interaction with the external perturbing magnetic field of the nucleus is depicted by a triangle. Diagrams **c-e** show the one-loop self-energy corrections. The one-loop corrections due to vacuum polarization is shown in **f-h**. Figure modified from [9].

the binding to the nucleus. However, upon interaction with the electron, the nucleus will experience a recoil depending on the respective ratio between electron mass and nuclear mass, m_e/m_{nucl}. This can be calculated by using an expansion in orders of the product $(Z\alpha)\, m_e/m_{nucl}$ [34]. The effect of this mass shift was tested by measuring the g-factor in two different isotopes of lithiumlike calcium, $^{40,48}Ca^{17+}$ [23]. Since these two nuclei have very similar nuclear radii [35], the difference in the respective g-factors are almost entirely due to the recoil contribution [25], which is purely relativistic.

Furthermore the nucleus is not a point-charge and can be modeled with a charge distribution. From this distribution, the size of the nucleus can be defined by its root-mean-square radius, $r_{rms} = \sqrt{\langle r^2 \rangle}$, and determined experimentally. For heavy HCIs, which corresponds to larger r_{rms}, the nuclear size effect can be 10^{-4}, see fig. 1.4. The availability and uncertainty of data on nuclear charge radii impose severe limitations on such calculations [9]. Additionally, the charge distribution, and also especially for larger Z deviations from a spherical charge distribution, must be taken into account in the theorical calculations. Leading corrections of the nuclear shape effect reach a level of up to 10^{-6} in the high-Z regime [36].

Possible approaches to either differentiate between different nuclear effects or to cancel them are measurements with different isotopes [23] or to measure the specific difference of g-factors in the same ion but in different charge states (as proposed in [37, 38]).

Interelectronic Interaction – Δg_{int}

In the case of lithium- and boronlike systems, there is moreover an interaction between the electrons. This likewise increases the number of Feynman diagrams to be evaluated by those ones containing interelectron interactions. This can be by exchange of

photons between electrons (one-photon exchange corresponds to first order in $(1/Z)^1$, whereas two-photon exchange and higher terms to orders of $(1/Z)^{\geq 2}$). Feynman diagrams containing in addition self-energy or vacuum-polarization terms are summarized as screened QED corrections [39]. For details on the calculation of electron-correlations see [27, 40] and references therein. Currently, in the medium- to high-Z regime the overall uncertainty of the g-factor calculations is dominated by the uncertainty due to the contribution from the interelectronic interactions [9].

High-precision measurement of the bound state electron g-factor not only constitute one of the most stringent tests on QED but furthermore give access to fundamental constants, such as the electron's atomic mass [41] or the fine-structure constant α [37, 38]. The latter would allow an independent determination of α and a comparison to previous most precise values, see sec. 1.1.1.

1.2. Optical Spectroscopy of Highly Charged Ions

Another promising approach is to use HCIs as frequency standards or for tests of BS-QED by means of high-precision spectroscopy in the optical domain. In the scope of this ALPHATRAP has been equipped with laser systems, which allowed cooling of trapped ions as well as laser spectroscopic investigations on them. By demonstrating a novel measurement technique (chap. 5), unique opportunities for high-precision spectroscopy arise.

Due to the strong compression of orbitals with increasing nuclear charge Z in HCI, the respective energy scale of various well-known effects are shifted compared to atoms or singly charged ions. This way, fine structure and hyperfine structure transitions can be shifted into the optical regime. Furthermore, the ordering of filled orbitals in HCI is a function of the nuclear charge Z, and for specific combination of charge state and Z the energy difference between two crossing orbitals can be in the optical regime [42].

1.2.1. Optical Clocks and Variation of the Fundamental Constants

Because all these transition are dipole forbidden and their long excited state lifetimes lead to very high quality factors, they are excellent candidates for a new generation of optical clocks, with applications to frequency standards and test of fundamental physics [42], e.g. tests of a possible variation of fundamental constants such as the fine-structure constant α [12, 43, 44]. A variation of fundamental constants [45] is predicted by extensions of the Standard Model [46]. To date, the experimental upper bound for a variation[6] of α is set by clock comparisons[7] between atomic and/or ion clocks [47–49] and is: $(1/\alpha)\,(\mathrm{d}\alpha/\mathrm{d}t) \lesssim 10^{-17}/\text{year}$. Future experiments based on the nuclear transition to the first excited isomeric state of thorium-229, ^{229m}Th, are planned as another approach

[6] This bound applies to present day variations, whereas astronomical observations test variations of α in space and past times, depending on the redshift of the observed objects.

[7] For these tests, both atomic clocks and clocks based on singly charged ions, such as $^{171}Yb^+$, $^{27}Al^+$ or $^{199}Hg^+$, are compared with each other.

[50, 51]. HCI have a very low sensitivity to external perturbations and several proposals attest HCI-based clocks an achievable fractional inaccuracy $\leq 10^{-19}$, competing with the currently best clocks [52, 53]. In addition, some transitions in HCI can have an increased sensitivity to an α variation compared to presently used atoms or singly charged ions [42].

1.2.2. Studying BS-QED with HCI

Studies of the HFS optical transitions allow to test BS-QED predictions in the strong field regime of medium-to-high Z ions. As mentioned previously, $Z\alpha$ is not small in this regime, so QED corrections have to be calculated in all orders of $Z\alpha$. For nuclei with a nonzero nuclear spin, $\left|\vec{I}\right| = \sqrt{I(I+1)}\hbar \neq 0$, the nuclear angular momentum can couple with the magnetic field caused by the bound electrons and a hyperfine structure can be observed [54]. As for the electron, eq. (1.1), the magnetic dipole moment of the nucleus $\vec{\mu}_\mathrm{I}$ in units of the nuclear magneton μ_N is related to the nuclear spin $\vec{I}$ by:

$$\vec{\mu}_\mathrm{I} = g_\mathrm{I} \frac{e}{2m_\mathrm{p}} \vec{I} = g_\mathrm{I} \mu_\mathrm{N} \frac{\vec{I}}{\hbar}, \tag{1.12}$$

where g_I is the (nuclear) g-factor, m_p is the proton rest mass and $\vec{I}$ is the intrinsic nuclear spin angular momentum given in units of $\hbar$. Therefore, the hyperfine structure can be seen as a bridge between atomic and nuclear physics. An approximate value for the HFS splitting in hydrogenlike ions can be given by [55]:

$$\Delta E_\mathrm{HFS}^{1S_{1/2}} = \frac{4}{3}\alpha\,(Z\alpha)^3\, g_\mathrm{I} \frac{m_\mathrm{e}}{m_\mathrm{p}} \frac{2I+1}{2} m_\mathrm{e}c^2 \left[A_{1S_{1/2}}(Z\alpha)\left(1-\delta_{1S_{1/2}}\right)(1-\epsilon)+\chi_\mathrm{rad}\right], \tag{1.13}$$

where $A_{1S_{1/2}}(Z\alpha)$ is the relativistic correction, $\delta_{1S_{1/2}}$ is a correction factor for the nuclear charge distribution, ϵ corrects for the nuclear magnetization distribution and χ_rad is the radiative correction from QED. For precise calculations of the HFS, the nuclear magnetic field cannot be approximated as a pointlike dipole. The nucleus has a substructure, as it is a composite particle made up of nucleons or even quarks, a system which is very difficult to describe ab initio. Rather the magnetization inside the nucleus is distributed, giving rise to the so-called Bohr-Weisskopf effect (BWE) or hyperfine anomaly [56]. A similar relation for lithiumlike ions can be found in [57].

In fig. 1.6, the resulting wavelength for hyperfine transitions in the laser accessible regime is shown. The shrinking of the electron wave function in HCI increases the probability density of the electron to be in the nucleus, therefore electrons become very sensitive probes to nuclear properties and nuclear effects are dramatically enhanced. Experimentally, the nuclear magnetic moments are difficult to measure. For measurements in atoms, a diamagnetic correction factor σ_dia must be introduced to account for the electron structure around the nucleus. This has to be derived from atomic structure calculations. One common way of determining nuclear magnetic moments is by nuclear magnetic resonance (NMR). In those experiments the nucleus of interest is embedded in molecules dissolved in a solution. This leads to temperature or even concentration

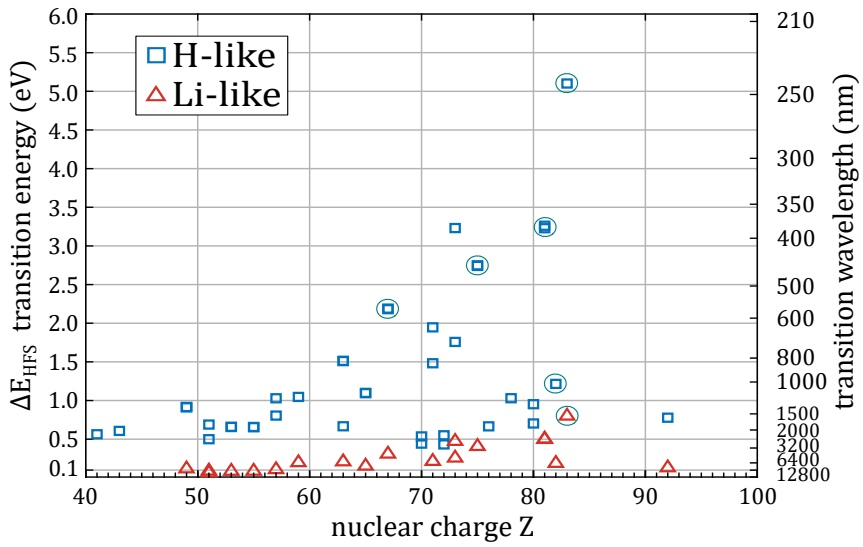

Figure 1.6.: Transition wavelengths for the HFS splitting in hydrogen- and lithium-like ions. Encircled are the transitions which were measured experimentally, see tab. 1.1. Data taken from [58, 59].

dependent paramagnetic chemical shifts σ_{chem}, which are theoretically hard to compute [10]. Tabulated values often contain old flawed values [10], which can cause significant disagreement between theoretical predictions and contemporary experimental observations, as in the case of the hyperfine structure measurements in hydrogen- and lithiumlike bismuth [60, 61].

Theoretical calculations of QED effects in the HFS are limited by the unprecise knowledge of the BWE, so nuclear contributions conceal the ones originating from QED effects. To circumvent this, it was proposed [62] to measure a specific difference of the hyperfine splitting in different charge states. This way tests of QED in the strongest magnetic fields become possible. By taking into account relativistic, nuclear and QED effects, HFS spectroscopy can also be used to directly measure nuclear dipole magnetic moments, which serve theoreticians and experimentalists as valuable input parameters. An overview of the HFS splittings in the ground state of hydrogenlike HCI measured by means of spectroscopy is given in tab. 1.1. So far these measurements with HCI are done either with electron beam ion traps (EBITs) or in storage rings. In an EBIT, the precision of such measurements is severly limited by the Doppler broadening of the observed lines, because of the high kinetic energy of the ions, that corresponds to temperatures of kK to MK. Also measurements in the storage ring are limited by the precise determination of the Doppler shift of the HCI. In order to determine precisely the relativistic velocity with which the ions are circulating, in-situ high-precision measurements of high voltages of $\mathcal{O}(10^5\ \text{V})$ used for the ion acceleration are required.

Table 1.1.: Overview of experimentally measured HFS transitions in HCI. Measurements are either performed in electron beam ion traps (EBITs) or inside a storage ring.

Ion	Measured in	wavelength (nm)	Ref.
$^{165}Ho^{66+}$	EBIT	572.64(15)	[63]
$^{185}Re^{74+}$	EBIT	456.05(3)	[64]
$^{187}Re^{74+}$	EBIT	451.69(3)	[64]
$^{203}Tl^{80+}$	EBIT	385.822(30)	[65]
$^{205}Tl^{80+}$	EBIT	382.184(34)	[65]
$^{207}Pb^{81+}$	storage ring	1019.7(2)	[66]
$^{209}Bi^{82+}$	storage ring	243.8221(44)	[61, 67]
$^{209}Bi^{80+}$	storage ring	1554.377(29)	[61, 67]

The excited states of forbidden transitions in HCI are long lived and this makes a fluorescence based detection experimentally challenging. The long lifetimes in turn result in very narrow natural linewidths and can be challenging to find, as one have to rely on theoretical calculations that have large uncertainties compared to the linewidths. For HCI binding energies easily reach the order of kV, so predicting atomic transitions, e.g. by level crossings, in the optical regime of few eV, with an fractional uncertainty of 10 %, requires a theory to achieve a fractional uncertainty in the order of 10^{-4}, which is a challenging task [42]. With the novel spectroscopy scheme presented in this thesis, the search and measurement of these transitions could be significantly facilitated.

1.3. Towards Sympathetic Laser Cooling at ALPHATRAP

One of the main limitations for high-precision measurements in Penning traps so far are energy and amplitude dependent frequency shifts [68]. In order to improve the achievable precision at ALPHATRAP, the implementation of sympathetic laser cooling of the stored HCI is planned. As mentioned earlier, HCIs do not have directly laser-accessible fast electric dipole transitions, which can be used for laser cooling. Therefore a sympathetic cooling scheme using a laser cooled auxiliary ion has to be employed. For the case of ALPHATRAP, this is done with singly charged beryllium. In this thesis a first step towards sympathetic laser cooling is presented, which was the first demonstration of a single laser cooled $^{9}Be^{+}$ at ALPHATRAP, see sec. 4. Cooling trapped ions leads to a compression of the spatial and momentum coordinate in the phase space and thus a narrower confinement of the particle. The smaller the amplitudes of the ions motion, the fewer residual anharmonicities of the trapping field are experienced by the ions. By storing two ions in the same trapping potential laser cooling of them leads to the formation of Coulomb Crystals, which opens up a new approach for measurements of g-factor difference of two ions stored next to each other at almost identical positions

inside the magnetic field of the trap, see [9]. A decreased particle's momentum reduces velocity dependent energy shifts from the second-order Doppler effect and relativistic mass increase.

The detection of a spin state transition using the continuous Stern-Gerlach effect is more difficult for heavy ions. The difference in the axial frequency scales inversely to the mass of the ion and therefore a spin state transition is more difficult to resolve. Fluctuations in the cyclotron energy of the ion cause axial frequency shifts because of the strong magnetic inhomogeneity used for the spin state analysis. The attainable signal-to-noise ratio for an unambiguous spin state identification will be increased due to the decreased energy in the radial mode [69], which is especially important for heavy HCI, e.g. lithiumlike bismuth.

Besides the anticipated improvement on the spin state spectroscopy, also the achievable precision for the determination of the motional frequencies using the phase sensitive technique PnA is expected to improve by the possibility to prepare the ion in a lower initial temperature and additionally the measurement time will be reduced [70]. Also the results presented in thesis on high-precision laser spectroscopy (chap. 5) will benefit by a lower particle energy, since the first order Doppler broadening of the resonance due to the finite temperature of the ion constitutes the main limitation of this proof-of-principle measurement.

Even though for the reasons stated above HCI are appealing candidates, laboratory experiments are exacerbated by the difficulties to produce, decelerate, trap and control HCIs. However, at ALPHATRAP all necessary key components and knowledge are available to handle HCI routinely. Recently, microwave studies of ground state electron g-factor [27] and optical spectroscopy on long lived fine structure states in $^{40}Ar^{13+}$ [71] were carried out. The latter is, besides the demonstrated laser cooling of $^{9}Be^{+}$, subject of this thesis. The structure of this thesis is as follows:

Chapter 2 gives an introduction to the used experimental techniques and methods which are used to control, manipulate and observe the ions inside the Penning trap. In chapter 3, the ALPHATRAP apparatus is presented. Together with the devices used for the production, transport and trapping of the ions, also the laser systems used for spectroscopic investigations and laser cooling of the stored ions are described. The results are presented in two separate chapters. In chapter 4 the results obtained for the laser cooling of a single beryllium ion are discussed. The main result of this thesis, the laser spectroscopy of the fine structure in highly charged argon is outlined in chapter 5. These results are summarized in chapter 6 and the last sections therein are focused on the possibilities that open up with the demonstrated techniques.

2. Penning-Trap Physics

This chapter provides an introduction to the theory and basics of Penning traps and the used methods and techniques. It will give the reader enough understanding of the performed experiments contained in this thesis, however, it is not intended to be a complete compendium of Penning-trap physics – which can be found e.g. in [72–74].

All traps for charged particles make use of the electromagnetic forces that the trapping fields can exert on a charged particle. Earnshaw's theorem [75] proves that for a point-shaped confinement of charged particles in a three-dimensional stable stationary equilibrium neither purely static magnetic nor purely static electric fields can be used. This can be circumvented by using a combination of static (DC) and alternating (AC) electric fields as done in a radio-frequency quadrupole or Paul trap [76]. These can be tuned to give a pseudopotential with a local minimum in space and time which allows to confine particles in all three dimensions. Another way is to use a combination of static magnetic and electric fields as done in Penning traps and discussed in the following.

2.1. The Ideal Penning Trap

Centerpiece of the ALPHATRAP experiment is a Penning trap optimized for storage and manipulation of highly charged ions. In such a trap, a superposition of a strong homogeneous magnetic field $\vec{B} = (0, 0, B_0)$ and a static quadrupole electric field $\vec{E} = -\vec{\nabla}\Phi$ created by a potential

$$\Phi = \frac{V_\mathrm{r} C_2}{2d^2}\left(z^2 - \frac{x^2}{2} - \frac{y^2}{2}\right) = k\left(2z^2 - x^2 - y^2\right) = k\left(2z^2 - \rho^2\right), \tag{2.1}$$

is used. V_r is the trapping voltage applied to the ring electrode, C_2 is a trap geometry dependent and dimensionless parameter and $d = \sqrt{\frac{1}{2}\left(z_0^2 + \frac{\rho_0^2}{2}\right)}$ is the characteristic trap length, (see fig. 2.2). The magnetic field ensures radial confinement via the Lorentz force in the plane perpendicular to the z-axis, similar to a cyclotron motion. At the center of the trap, the electric field has a minimum in the axial z-direction and a maximum in the radial ρ-direction. This results in a confining axial force and a repulsion in the radial direction, which has to be counterbalanced by the inward directed magnetic force. In addition, the superposition of electric and magnetic field causes a slow $\vec{E} \times \vec{B}$ drift. Therefore, the radial motion in the x-y-plane can be separated into a fast cyclotron motion arising mainly from the magnetic field and a slow drift due to the perpendicular arrangement of the electric and magnetic field[1]. The resulting force on a particle with

[1] Under the assumption the electric field is weaker than the magnetic field.

charge q, mass m and position $\vec{r} = (x, y, z)$ in such an electromagnetic field can be calculated from $\vec{F} = m\ddot{\vec{r}} = q\left(\vec{E} + \dot{\vec{r}} \times \vec{B}\right)$ and yields the following equation of motion (eom) in the nonrelativistic case:

$$\ddot{x} = \frac{q}{m}\left(kx + B_0\dot{y}\right), \tag{2.2a}$$

$$\ddot{y} = \frac{q}{m}\left(ky - B_0\dot{x}\right), \tag{2.2b}$$

$$\ddot{z} = \frac{q}{m}\left(-2kz\right). \tag{2.2c}$$

In the axial direction, eq. (2.2c) can be identified as a harmonic motion decoupled from the radial motion. This results in an axial angular frequency[2] ω_z of

$$\omega_z = \sqrt{\frac{2kq}{m}} = \sqrt{\frac{qV_\mathrm{r}C_2}{md^2}}. \tag{2.3}$$

In the radial coordinates the eoms are coupled differential equations. By using the complex-valued ansatz $u(t) = x(t) + iy(t)$, they can be solved and eq. (2.2a) and (2.2b) are combined to:

$$\ddot{u} = \frac{q}{m}\left(ku - iB_0\dot{u}\right) = \frac{\omega_z^2}{2}u - i\omega_c\dot{u}. \tag{2.4}$$

Here, ω_c is the cyclotron frequency an ion would have in a purely magnetic field:

$$\omega_c = \frac{qB_0}{m}. \tag{2.5}$$

By using $u(t) = \hat{u}_0 \exp(-i\omega t)$, eq. (2.4) yields a quadratic equation

$$\omega^2 - \omega\omega_c + \frac{\omega_z^2}{2} = 0, \tag{2.6}$$

with the solutions

$$\omega_\pm = \frac{1}{2}\left(\omega_c \pm \sqrt{\omega_c^2 - 2\omega_z^2}\right). \tag{2.7}$$

In order to have a stable trajectory, the square root in eq. (2.7) has to be real and therefore $\omega_c^2 - 2\omega_z^2 > 0$. We can identify the aforementioned fast cyclotron-like motion with ω_+, which is therefore termed the modified cyclotron frequency. The slow motion arising from the $\vec{E}\times\vec{B}$ drift can be assigned to ω_- and is named magnetron frequency. For typical trapping parameters, a hierarchy of frequencies is established, $\omega_- \ll \omega_z \ll \omega_+ < \omega_c$, see also tab. A.1 in the case of ALPHATRAP. By combining eq. (2.3) and eq. (2.7) the following useful relations between the three eigenfrequencies can be derived:

$$\omega_+ + \omega_- = \omega_c, \tag{2.8a}$$

$$2\omega_+\omega_- = \omega_z^2, \tag{2.8b}$$

$$\omega_+^2 + \omega_-^2 + \omega_z^2 = \omega_c^2. \tag{2.8c}$$

[2] ω denotes the angular frequency which is related to the physical frequency ν typically measured in the experiment by $\omega = 2\pi\nu$. Throughout this thesis both notations will be used interchangeably.

Eq. (2.8c) is referred to as the *Brown-Gabrielse invariance theorem* [74]. Unlike eq. (2.8a) and eq. (2.8b), it holds true even for certain unavoidable imperfections which real Penning traps have, see sec. 2.2. The radial eom, eq. (2.4), has as a general solution which is the superposition of two independent harmonic motions with the frequencies ω_+ and ω_- and respective radii[3] ρ_+ and ρ_-:

$$x(t) = \rho_+ \cos(\omega_+ t + \phi_+) + \rho_- \cos(\omega_- t + \phi_-), \tag{2.9a}$$

$$y(t) = -\frac{q}{|q|} \left[\rho_+ \sin(\omega_+ t + \phi_+) + \rho_- \sin(\omega_- t + \phi_-)\right], \tag{2.9b}$$

$$z(t) = \rho_z \cos(\omega_z t + \phi_z). \tag{2.9c}$$

In fig. 2.1, the general solution and thus the trajectory of a particle in a Penning trap is illustrated. The three eigenmotions are independent from each other and can be

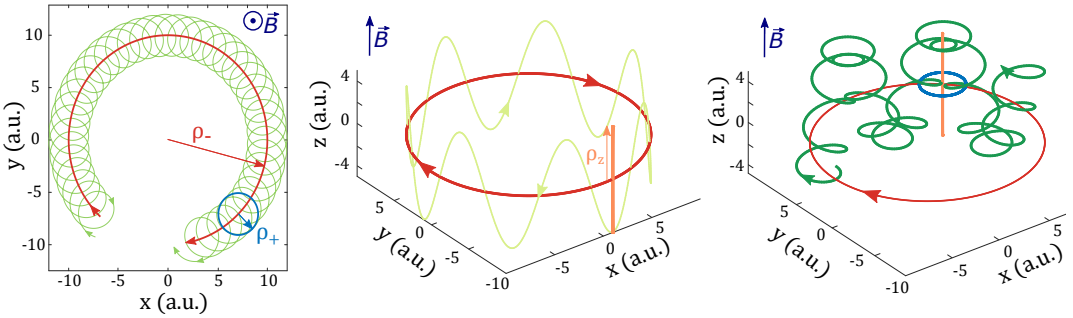

Figure 2.1.: **left** Projection of the ion's motion into the radial x-y plane. The combined motion (green) of cyclotron (blue) and magnetron (red) motion is shown. **middle** Combined motion (green) of the magnetron (red) and axial (orange) mode. **right** Resulting trajectory (green) of a positively charged ion in a Penning trap. For this visually good and qualitative representation, the ratios of frequencies and radii for the plots are: $\omega_- : \omega_z : \omega_+ = 1:7:49$ and $\rho_- : \rho_z : \rho_+ = 10:2:5$.

considered as independent harmonic oscillators with each mode having a certain kinetic and potential energy[4]. As a peculiarity, the magnetron motion is metastable [74], since most of its energy is potential. An increase in magnetron energy leads to a decrease of the magnetron radius. The total time-averaged energy $\langle E_{\text{tot}} \rangle$ of a spinless charged particle in the Penning trap can then be given as the sum of kinetic $\langle E_{\text{k}} \rangle$ and potential energy $\langle E_{\text{p}} \rangle$ [72]:

$$\langle E_{\text{tot}} \rangle = \underbrace{\frac{1}{4} m\omega_z^2 \rho_z^2 + \frac{1}{2} m\omega_+^2 \rho_+^2 + \frac{1}{2} m\omega_-^2 \rho_-^2}_{\langle E_{\mathbf{k}} \rangle} + \underbrace{\frac{1}{4} m\omega_z^2 \left(\rho_z^2 - \rho_+^2 - \rho_-^2\right)}_{\langle E_{\text{p}} \rangle}. \tag{2.10}$$

[3] Amplitude and radius of a harmonic motion is used interchangeable here. Typically radius, which is constant, is used for motions in the radial plane, whereas for the oscillatory axial motion typically amplitude is used.

[4] As shown in sec. 2.6, a temperature can be assigned an energy distribution.

By using eq. (2.8b), the equation above can be arranged to the sum of energies in the individual modes and also be expressed in a quantum mechanical description of harmonic oscillators, see fig. 2.7:

$$\langle E_{\mathrm{tot}}\rangle = \underbrace{\frac{1}{2}m\omega_z^2\rho_z^2}_{\langle E_z\rangle=\left(\langle n_z\rangle+\frac{1}{2}\right)\hbar\omega_z} + \underbrace{\frac{1}{2}m\omega_+\left(\omega_+-\omega_-\right)\rho_+^2}_{\langle E_+\rangle=\left(\langle n_+\rangle+\frac{1}{2}\right)\hbar\omega_+} + \underbrace{\frac{1}{2}m\omega_-\left(\omega_--\omega_+\right)\rho_-^2}_{\langle E_-\rangle=\left(\langle n_-\rangle+\frac{1}{2}\right)\hbar\omega_-}. \tag{2.11}$$

However, the typical parameters the experiments are operated at yield large quantum numbers n_i larger than 100 000. This shows that a purely classical description is justified here.

2.2. The Real Penning Trap

The previously discussed electric potential, eq. (2.1), can be realized by a suitable geometry of electrodes. The two most commonly used geometries are hyperbolical shaped [74, 77, 78] electrodes, with their contours following the hyperbolic equipotential surfaces of the trapping potential, or cylindrical ring electrodes. ALPHATRAP uses a Penning-Malmberg type [79] trap geometry, with cylindrical electrodes and open endcaps (see fig. 2.2). In contrast to hyperbolic traps, this design has the advantage of having axial access along the magnetic field axis. It allows both the injection of highly charged ions from one side and electromagnetic radiation, such as millimeter waves or laser beams from the opposite end – a very important feature as will be apparent later on. Furthermore, manufacturing cylindrical electrodes is easier and feasible with lower mechanical tolerances than hyperbolic electrodes.

Whereas in the previous section the idealized Penning trap was discussed, this section summarizes some effects that occur in a real Penning trap used for high-precision experiments. Differences from the ideal case arise mainly due to deviations from a harmonic potential for the case of the electric field or from a homogeneous magnetic field and misalignment between the axes of electric and magnetic field or relativistic effects [80]. These imperfections will lead to systematic frequency shifts and the proper calculation and thoughtful treatment of those in the conception of a measurement and an evaluation of the data is decisive. In the following some selected effects are discussed.

2.2.1. Electric Field

A design with cylindrical electrodes has proven to be very well suited to produce a harmonic electrostatic trapping potential at the center of the trap [79, 81]. By choosing a suitable ratio of length and radius of the electrodes and using additional correction electrodes [82], the harmonicity of the trapping field can be improved. The trap electrodes forming the Penning trap have to be arranged symmetrically around a central, so called ring electrode (RE). The ring electrode is encompassed by one or two pairs of lower and upper correction electrodes (UC/LC) and a pair of upper and lower endcap electrodes (UE/LE), yielding a 5- or 7-electrode configuration, respectively, see fig. 2.2.

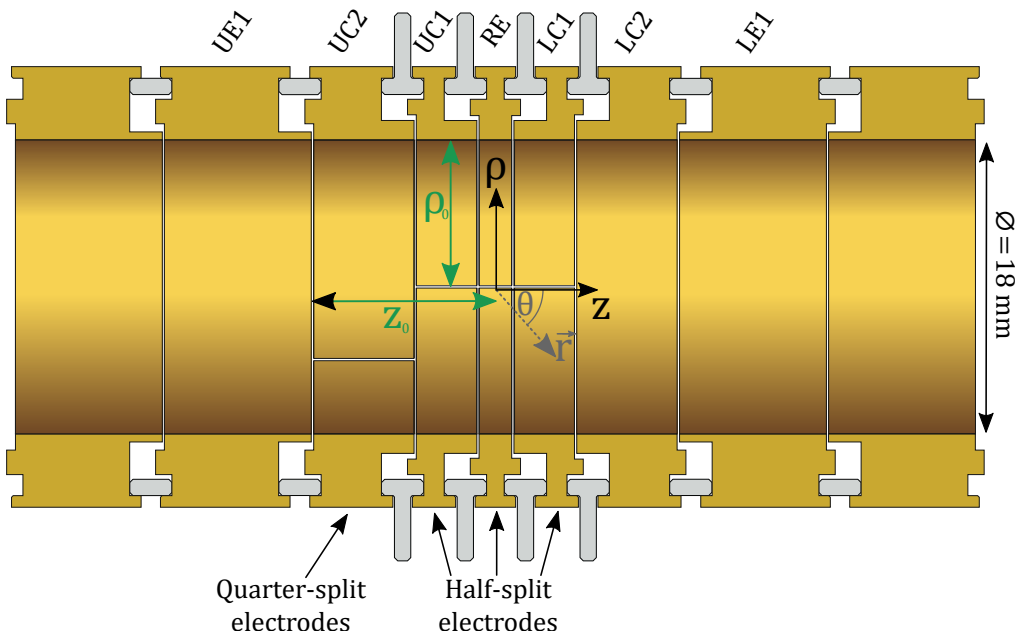

Figure 2.2.: Schematic drawing of the precision trap (PT) of ALPHATRAP. In its conception as a 7-electrode trap, the central ring electrode (RE) is encompassed by two pairs of correction electrodes (UC/LC 1&2) and a pair of endcap electrodes (UE/LE 1). By applying suitable voltages, typically symmetrically around *RE*, the trap can be made orthogonal and compensated, for details see text. Adapted from [9].

The potential at the center ($r/\rho_0 \ll 1$, for $r = |\vec{r}| = \sqrt{\rho^2 + z^2}$ being the distance from the trap center) of this configuration can be expressed by a series expansion [72, 74]:

$$\Phi(\rho, z, \theta) = \frac{V_\mathrm{r}}{2} \sum_{n=0}^{\infty} C_n \left(\frac{r}{d}\right)^n P_n(\cos(\theta)). \tag{2.12}$$

P_n are Legendre polynomials of order n, θ is the polar angle, $\cos(\theta) = \frac{z}{r}$, and C_n are dimensionless expansion coefficients. The anharmonicity of the potential can thus be characterized by the C_n coefficients. Typically for the given axial mirror symmetry, odd C_n are vanishing [83, 84]. Comparison to eq. (2.1) shows that the ideal harmonic potential has only $C_2 \neq 0$ and all other even $C_{n>2} = 0$. In the comprehensive review [68], the first order shifts in frequency $\Delta\omega_i$ arising from cylindrical imperfections are

derived and can be written as[5]:

$$\frac{\Delta\omega_z}{\omega_z} = \frac{C_4}{C_2}\frac{3}{4d^2}\left(\rho_z^2 - 2\rho_+^2 - 2\rho_-^2\right), \tag{2.13a}$$

$$\frac{\Delta\omega_\pm}{\omega_\pm} = \mp\frac{C_4}{C_2}\frac{3}{2d^2}\frac{\omega_+\omega_-}{\omega_+ - \omega_-}\left(2\rho_z^2 - \rho_\pm^2 - 2\rho_\mp^2\right). \tag{2.13b}$$

As a consequence, the eigenmotions in a real Penning trap are not independent and shifts in the eigenfrequencies will depend on the radii and thus energies of all modes. In order to reduce these frequency shifts, the voltages symmetrically applied to the correction electrodes V_{Ci} can be set such that the even terms up to C_{10} vanish for a 7-electrode trap with carefully chosen dimensions. Such a trap is called compensated[6]. For this purpose, the tuning ratio TR_i can be defined through the ratio of the voltages applied to the correction and the ring electrode $TR_1 = \frac{V_{C1}}{V_r}$, respectively $TR_2 = \frac{V_{C2}}{V_r}$. Inside the trap, the potentials from different electrodes add up and the resulting $\tilde{C}_n$ is [40]:

$$\tilde{C}_n = C_n + D_n^{\text{comb}} = C_n + D_{n1}\,TR_1 + D_{n2}\,TR_2. \tag{2.14}$$

The D parameters describe the effect of the applied correction voltage and are geometry dependent [81]. For an improved operation of the trap, fulfillment of the orthogonality criterion is of importance, which means that the axial frequency is independent of changes in the tuning ratio, $\frac{\mathrm{d}\omega_z}{\mathrm{d}TR} = 0$. For the 7-electrode trap, the double orthogonality $D_{21} = D_{22} = 0$ cannot be fulfilled at the same time [25], but for the combined orthogonality, as defined in eq. (2.14), $D_2^{\text{comb}} = D_{21}\,TR_1 + D_{22}\,TR_2 = 0$ can be met which yields a constant ratio of the correction voltages, $\frac{V_{C1}}{V_{C2}}$.

2.2.2. Magnetic Field

A strong homogeneous magnetic field, generated by a superconducting magnet, is used (see sec. 3.3). The magnet is equipped with shim coils [85] to improve the homogeneity of the magnetic field after energization of the magnet main coil. The experimental setup exhibits unavoidably a nonzero magnetic susceptibility, which causes inhomogenieties of the magnetic field after insertion of the setup into the bore of the magnet. Analogous to the treatment of electrostatic field imperfections, also the magnetic field can be expanded into a series of multipoles [84, 86]:

$$\vec{B}(\rho, z) = B_0\vec{e}_z + B_1\left[z\,\vec{e}_z - \frac{1}{2}\rho\,\vec{e}_\rho\right] + B_2\left[\left(z^2 - \frac{1}{2}\rho^2\right)\vec{e}_z - z\rho\,\vec{e}_\rho\right] + \mathcal{O}(B_{n>2}). \tag{2.15}$$

As derived in [87], already the linear gradient B_1 will cause a second order shift in the modified cyclotron frequency:

$$\frac{\Delta\omega_+}{\omega_+} \cong -\frac{1}{2}\left(\frac{B_1}{B_0}\right)^2\left[\left(\frac{\omega_+}{\omega_z}\right)^2 - \frac{1}{2}\right]\rho_+^2 \propto E_+. \tag{2.16}$$

[5] For typical experiment parameters the motional amplitudes are comparably small. Since the shifts scale $\propto C_n\rho^n$, contributions by C_4 are thus dominant.

[6] Originally this term was applied for 5-electrode trap, which is compensated if $C_4 = C_6 = 0$.

Frequency shifts due to quadratic B_2 inhomogeneities can be expressed by [68]:

$$\frac{\Delta\omega_z}{\omega_z} = \frac{B_2}{4B_0}\frac{\omega_+ + \omega_-}{\omega_+\omega_-}\left(\rho_-^2\omega_- + \rho_+^2\omega_+\right), \tag{2.17a}$$

$$\frac{\Delta\omega_\pm}{\omega_\pm} = \pm\frac{B_2}{2B_0}\frac{\omega_+ + \omega_-}{\omega_+ - \omega_-}\left[\rho_z^2 - \rho_\mp^2\left(1 + \frac{\omega_\mp}{\omega_\pm}\right) - \rho_\pm^2\right]. \tag{2.17b}$$

The main contribution to the finite B_2-value in the homogeneous trapping region of the precision trap (PT) is the residual nonhomogeneous field of the ferromagnetic ring of the analysis trap (AT) extending into this region (see sec. 2.5.1). For this purpose a compensation ring of the same ferromagnetic material was installed that compensates this effect and suppresses the field inhomogeneities by about one order of magnitude [40].

Besides spatial inhomogeneities also temporal variations in the magnetic field will compromise high-precision measurements. Depending on the amplitude and time scale of fluctuations with respect to the finite measurement time, scaling strongly with the applied technique [40, 83], this will ultimately limit the achievable measurement precision. Therefore, exhaustive characterization of the magnetic field stability were performed for different time scales [9, 40, 84]. Currently the effectiveness of temperature and pressure stabilization of cryogenic liquid reservoirs of cryostat and magnet (see sec. 3.3) are investigated [88].

In general, shifts of the eigenfrequencies due to changing motional energies respectively radii are unwanted. However they can also be used deterministically in certain methods, e.g. by measuring energy dependent frequency shifts. An energy distribution of a mode can be measured and a temperature for this mode can be derived, see sec. 4.4.1 and 5.4.

2.2.3. Misalignment and Ellipticity

Even though extensive care is taken in the mechanical design and mounting structures of the trap setup [9, 84], in reality, a misalignment between the magnetic field and electric field axis is unavoidable. In addition, also the electric field can have an asymmetry, e.g. caused by a misalignment of the electrodes with respect to each other, by patch potentials on the surface or by accumulation of unwanted charges [89, 90]. In general, the misalignment of the magnetic field axis with respect to the electrostatic field axis can be described by the polar angle θ and azimuthal angle ϕ, whereas the ellipticity of the electric potential can be defined via a single asymmetry parameter ϵ [89]:

$$\vec{B} = B_0\sin\theta\cos\phi\,\vec{e}_x + B_0\sin\theta\sin\phi\,\vec{e}_y + B_0\cos\theta\,\vec{e}_z, \tag{2.18a}$$

$$\Phi = k\left[2z^2 - \left(x^2 + y^2\right) - \epsilon\left(x^2 - y^2\right)\right]. \tag{2.18b}$$

These imperfections will couple the eigenmodes and the motional frequencies ω_i will depend on the misalignment and ellipticity, $\omega_i \to \tilde{\omega}_i = \tilde{\omega}_i(\theta, \phi, \epsilon)$ [89, 91]. Theorem eq. (2.8c) is invariant against the two aforementioned imperfections [89], so $\omega_+^2 + \omega_-^2 + \omega_z^2 = \omega_c^2 = \tilde{\omega}_+^2 + \tilde{\omega}_-^2 + \tilde{\omega}_z^2$ yields exactly the free cyclotron frequency as calculated from the ideal eigenfrequencies. This constitutes a very powerful property of the Penning trap that enables high-precision measurements.

2.3. Electronic Detection of an Ion

Key part of the measurements performed in Penning traps is the determination of the motional frequencies of the different eigenmodes. For this purpose different techniques were developed over the course of time [72]. In the following section, a method to determine the ion's motional frequency will be discussed which is also used at ALPHATRAP. The technique is nondestructive, which allows to perform continuous repeated measurements on the same ion for an extended period of time. This can be achieved by detecting the image current that is induced by the ion in the trap electrodes [92, 93]. It is based on the method of image charges [94], which describes how a (point) charge next to a boundary surface, e.g. a conducting surface, can alter the surface-charge density.

2.3.1. Image Current

Since the ion is oscillating in the trap, the induced image charges on the electrodes will exhibit a periodic change in time as well, which can be seen as an image current of typically a few fA. By choosing a suitable electrode arrangement or geometry, this current can be picked up and measured by using a bolometric detection scheme as proposed in [92] and first demonstrated in [95]. The following derivation will focus on the axial motion of the ion only.

In the simplest picture, the trap and ion can be modeled with equivalent electronic circuits, see fig. 2.3. The induced image current I_{ic} is determined by the charge q and

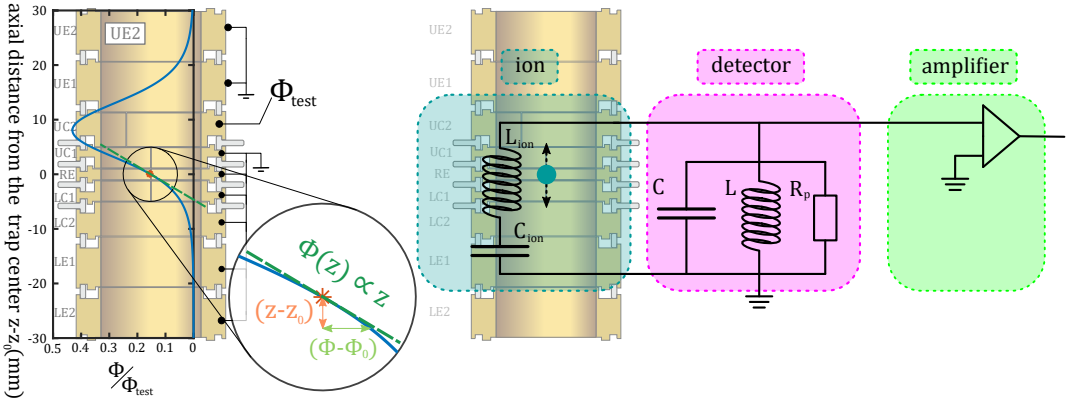

Figure 2.3.: **left** Exemplary potential configuration for the determination of d_{eff}. **right** Equivalent circuit representation of the ion-detector system. The tank circuit is a parallel RLC circuit. The ion can be modeled as a LC-series circuit. For details see text.

the velocity $\dot{z}(t)$ of the ion and the effective electrode distance d_{eff} [96]:

$$I_{\mathrm{ic}} = \frac{q}{d_{\mathrm{eff}}}\dot{z}(t) \overset{(2.9c)}{=} \frac{q}{d_{\mathrm{eff}}}\rho_z\omega_z \sin\left(\omega_z t + \phi_z\right). \tag{2.19}$$

The effective electrode distance d_{eff} quantifies the strength of the interaction between the ion and the electrode selected as pickup electrode for detection. If there were a voltage V_{test} applied to this electrode, while all other electrodes were grounded, the ion would experience an electric field E_{test} caused by the potential of this electrode. For small oscillation amplitudes of the ion, the change of potential $\Delta\Phi$ around its center of motion z_0 can be approximated linearly:

$$\Delta\Phi(z) = \frac{\partial\Phi}{\partial z}(z - z_0) = -E_{\text{test}}(z - z_0). \tag{2.20}$$

This allows to define the trap geometry dependent effective electrode distance d_{eff}:

$$d_{\text{eff}} = \frac{V_{\text{test}}}{E_{\text{test}}}. \tag{2.21}$$

The induced image current can be measured by attaching an impedance $Z(\omega)$ to the pickup electrode, which translates the image current into a time-dependent voltage

$$V_{\text{ic}}(\omega) = Z(\omega) I_{\text{ic}}, \tag{2.22}$$

that can be measured upon amplification.

2.3.2. Parallel RLC-Circuit

The necessary impedance can be realized by a superconducting parallel tank circuit (resonator) of a very high quality factor Q. It consists of a helical coil[7] of inductance L and a parallel parasitic capacity C [9, 84]. This capacity originates from the nonzero capacity of the connected trap electrode, the coil, the amplifier and cabling. In addition, typical losses of the whole circuit [96] are modeled as an equivalent parallel resistance R_p, see fig. 2.3. The resulting impedance of an RLC parallel circuit Z_{RLC} can be calculated from the individual impedances Z_i of its constituents:

$$\frac{1}{Z_{\text{RLC}}(\omega)} = \sum_{j=R,L,C} \frac{1}{Z_j} = \underbrace{i\omega C}_{1/Z_{\text{C}}} - \underbrace{\frac{i}{\omega L}}_{1/Z_{\text{L}}} + \underbrace{\frac{1}{R_{\text{p}}}}_{1/Z_{\text{R}}} = \frac{i\omega}{L\omega_{\text{r}}^2} - \frac{i\omega_{\text{r}}^2 C}{\omega} + \frac{1}{R_{\text{p}}}, \tag{2.23}$$

where $\omega_{\text{r}} = \frac{1}{\sqrt{LC}}$ [97] is the resonance frequency[8] of this resonator. In order to describe the damping of the oscillator, the quality factor Q can be used. It can be defined via the ratio of its resonance frequency ω_{r} to the resonance width $\Delta\omega$ at a level of $-3\,\text{dB}$ below the maximum, so $Q = \omega_{\text{r}}/\Delta\omega$ (see fig. 2.4). Alternatively, the Q factor of a parallel RLC circuit can be also given by [97]:

$$Q = R_{\text{p}}\sqrt{\frac{C}{L}} = \frac{R_{\text{p}}}{\omega_{\text{r}} L} = \omega_{\text{r}} R_{\text{p}} C, \tag{2.24}$$

[7] In the specific design of ALPHATRAP.

[8] The nonzero resistance will shift this resonance frequency, but for typical resonator parameters this shift is negligible.

which allows to rewrite eq. (2.23):

$$\frac{1}{Z_{\mathrm{RLC}}(\omega)} = \frac{1}{R_\mathrm{p}}\left[1 + iQ\left(\frac{\omega}{\omega_\mathrm{r}} - \frac{\omega_\mathrm{r}}{\omega}\right)\right] \xrightarrow{\omega=\omega_\mathrm{r}} \frac{1}{Z_{RLC}(\omega_\mathrm{r})} = \frac{1}{R_\mathrm{p}}. \tag{2.25}$$

On resonance, $\omega = \omega_\mathrm{r}$, the frequency-dependent impedance $Z_{RLC}(\omega)$ of a parallel RLC circuit is entirely real-valued $Z_{RLC}(\omega_\mathrm{r}) = R_\mathrm{p}$ and maximal [97].

2.3.3. Interaction Between Ion and Resonator

In the previous section, it was discussed how the ion induced image current I_ic is converted to a voltage V_ic making use of a parallel RLC circuit. In turn this voltage leads to a back action onto the ion. The change in the electric potential V_ic will cause a change of the electric field E_z and therefore effectively exert a force on the ion:

$$F_z = -qE_z \overset{(2.21)}{=} -q\frac{V_\mathrm{ic}}{d_\mathrm{eff}} \overset{(2.22)}{=} -q\frac{\Re\left(Z_{\mathrm{RLC}}(\omega)\right) I_\mathrm{ic}}{d_\mathrm{eff}}. \overset{(2.19)}{=} \underbrace{-\frac{q^2\Re\left(Z_{\mathrm{RLC}}(\omega)\right)}{d_\mathrm{eff}^2}}_{:=\gamma m}\dot{z}. \tag{2.26}$$

This additional force can now be added to the eom eq. (2.2c), which leads to an eom of a damped harmonic oscillator,

$$\ddot{z} = -\omega_z^2 z - \gamma\dot{z}. \tag{2.27}$$

In typical experiment conditions, the axial potential depth of the trap is tuned such that the axial frequency of the ion, eq. (2.3), coincides with ω_r. This way the energy E of the ion's motion will be dissipated into the RLC circuit[9] most efficiently [72, 98]:

$$\frac{\mathrm{d}\left\langle E\right\rangle}{\mathrm{d}t} = -\Re\left(Z_{\mathrm{RLC}}(\omega)\right)\left\langle I^2\right\rangle \overset{(2.19)}{=} -\frac{\Re\left(Z_{\mathrm{RLC}}(\omega)\right)q^2}{md_\mathrm{eff}^2}\left\langle E\right\rangle, \tag{2.28}$$

which shows an exponential decay of the energy on a characteristic time scale called the cooling time constant τ:

$$E(t) = E_0\exp\left(-t/\tau\right), \tag{2.29a}$$

$$\tau(\omega) = \frac{md_\mathrm{eff}^2}{\Re\left(Z_{RLC}(\omega)\right)q^2}. \tag{2.29b}$$

Whereas the real part of $Z_{\mathrm{RLC}}(\omega)$ causes resistive dissipation of the ion's energy, the imaginary part of $Z_{\mathrm{RLC}}(\omega)$ results in a shift $\Delta\omega_\mathrm{ic}$ of the ion's frequency via an image current[10]. This effect is also termed frequency pulling, for which an analytical formula was derived in [102].

[9] Only the real value of the complex impedance $Z_{RLC}(\omega)$ will cause ohmic dissipation [97].

[10] Not to be mistaken for the image charge shift, which is resonator independent and caused by the induced image charges on the trap electrodes also causing frequency shifts, for details see [99–101].

By using eq. (2.19) and eq. (2.22), above eom can be rewritten into a form that gives a relation to the induced current and voltage:

$$\dot{I}_{\mathrm{ic}} = -\omega_z^2 \int_t I_{\mathrm{ic}} \mathrm{d}t + \frac{q^2 \Re\left(Z_{\mathrm{RLC}}(\omega)\right)}{d_{\mathrm{eff}}^2 m} I_{\mathrm{ic}} \overset{(2.22)}{=} -\omega_z^2 \int_t I_{\mathrm{ic}} \mathrm{d}t + \frac{q^2 V_{\mathrm{ic}}}{d_{\mathrm{eff}}^2 m}. \tag{2.30}$$

By rearranging this formula, one can see that the induced voltage V_{ic} has two contributions which can be identified as a voltage caused by an inductance L_{ion} and a capacitance C_{ion} [97]:

$$V_{\mathrm{ic}} = \frac{\omega_z^2 d_{\mathrm{eff}}^2 m}{q^2} \int_t I_{\mathrm{ic}} \mathrm{d}t + \frac{m d_{\mathrm{eff}}^2}{q^2} \dot{I}_{\mathrm{ic}} = \frac{1}{C_{\mathrm{ion}}} \int_t I_{\mathrm{ic}} \mathrm{d}t + L_{\mathrm{ion}} \dot{I}_{\mathrm{ic}}. \tag{2.31}$$

Eq. (2.31) has the same structure as the differential equation of an undamped LC series circuit. This means that the ion can be equivalently modeled as such a circuit and the whole system of ion interacting with the resonator can be considered as an LC series circuit coupled to an RLC parallel circuit, see fig. 2.3. A capacitance C_{ion} and inductance L_{ion} can be assigned to the ion:

$$C_{\mathrm{ion}} = \frac{q^2}{\omega_z^2 d_{\mathrm{eff}}^2 m}, \tag{2.32a}$$

$$L_{\mathrm{ion}} = \frac{m d_{\mathrm{eff}}^2}{q^2}. \tag{2.32b}$$

The resonance frequency of an LC circuit is given by $1/\sqrt{LC}$ which in this case yields exactly the ion's axial frequency, $\omega_z = 1/\sqrt{L_{\mathrm{ion}} C_{\mathrm{ion}}}$. In the following section it will be discussed how the expected signal of this system looks like.

2.3.4. Signal Form

The ion is coupled to the electron gas in the conducting elements of the resonator and the electron gas acts as a heat bath for the ion. It is thermalized to the ambient temperature of the resonator and the environment, which in the case of ALPHATRAP is cooled down by a liquid helium reservoir (see sec. 3.3), anchoring the resonator roughly to the temperature of the boiling point of liquid helium of 4.2 K at normal atmospheric pressure [103]. The temperature of the ion[11] converges on timescales of the cooling time constant τ towards the noise equivalent temperature of the resonator, which is under ideal conditions the thermal temperature of the electron gas in the resonator of 4.2 K.

The signal of the detection circuit without ion and at a finite temperature T is the thermal noise spectrum of the detection system itself. Even if there is no voltage applied to a conductor, there will be a measurable voltage noise only depending on the temperature T and ohmic resistance $\Re(Z)$ of the conductor. This is named Johnson-Nyquist noise, after Johnson who measured it first [104, 105] and Nyquist who gave the theoretical explanation for it [106]. The latter derived following relation for the root-mean-square voltage V_{rms} in a frequency bandwidth $\Delta\nu$:

$$V_{\mathrm{rms}} = \sqrt{\langle V^2 \rangle} = \sqrt{4 k_{\mathrm{B}} T \Re(Z) \Delta\nu}, \tag{2.33}$$

[11] A definition for the temperature of a single ion is given in sec. 2.6

where k_B is the Boltzmann constant. For the measurement of frequencies it is advantageous to look at the signal in frequency space after a Fast Fourier Transformation (FFT), see fig. 2.4.

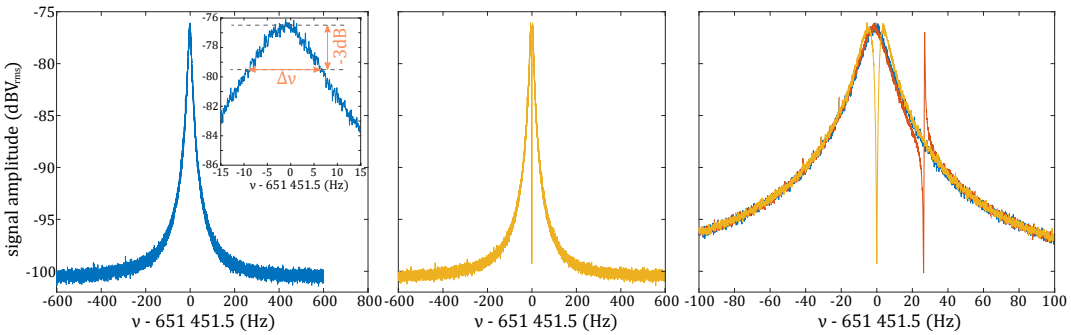

Figure 2.4.: **left** Thermal noise spectrum of the resonator without ion. In the inset the FWHM of the resonator is depicted. **middle** The signal of a single $^{40}Ar^{13+}$ ion close to the resonator center frequency, $\omega_z = \omega_r$, exhibits the distinct dip shape. **right** For the case $\omega_z \neq \omega_r$, the dip signal line shape becomes dispersive. For details see text.

Analog to eq. (2.23), the total impedance Z_t of the ion-resonator system (fig. 2.3) can be calculated as a circuit consisting of the ion's series LC equivalent circuit (2.32) parallel to the RLC circuit (2.23) of the resonator:

$$\frac{1}{Z_t(\omega)} = \frac{1}{Z_{RLC}} + \frac{1}{Z_{ion}} = \underbrace{i\omega C - \frac{i}{\omega L} + \frac{1}{R_p}}_{1/Z_{RLC}} \underbrace{-i\left(\frac{\omega}{\omega_z^2 C_{ion}} - \frac{\omega_z^2 L_{ion}}{\omega}\right)^{-1}}_{1/Z_{ion}}. \tag{2.34}$$

The voltage induced by the ion as described above will add to the thermal noise voltage of the detection circuit, however they are phase-shifted[12] by π [72, 83]. The ion equivalent LC-circuit has its minimal impedance at the ion's axial frequency ω_z and shortens the thermal noise of the resonator. This causes the amplitude in the thermal noise spectrum to approach zero in thermal equilibrium. This behavior leaves a signature in the FFT of the detected signal and is termed a *dip*, see fig. 2.4 middle. For a single ion the width of this dip ($-3\,$dB from its maximum) can be calculated by:

$$\delta\nu_{dip} = \frac{1}{2\pi\tau} = \frac{R_p q^2}{2\pi m d_{eff}^2}. \tag{2.35}$$

This relation also allows to determine the number of thermalized ions of the same kind. The width of the dip for multiple ions, $\delta\nu_{dip}^N$, scales linearly with the number N of ions,

[12] If they were not, the incoherent thermal noise of the resonator would excite the ion.

$\delta\nu_{\mathrm{dip}}^{N} = N\delta\nu_{\mathrm{dip}}$, for small N and as long as the the dip width is smaller than the width of the resonator.

If the ion's motional frequency does not coincide with the resonator resonance frequency, $\omega_z \neq \omega_{\mathrm{r}}$, the dip has a dispersive line shape (fig. 2.4 right). In case the ion is not thermally equilibrated with the resonator, a *peak* signal instead of a dip is observed.

While in this treatment the explicit case of axial motion was considered, the same principle can also be applied to the modified cyclotron motion of the ions. For the detection of the motion in the radial plane, a radially split cylindrical electrode has to be used instead.

2.4. Excitation and Coupling of Modes

Certain measurement schemes, such as phase sensitive methods (see sec. 5.6) or the manipulation and preparation of the ion's motional state, require a method for addressing and coupling different modes. As described earlier, the trajectory of the ion in the trap is a superposition of three (almost) independent eigenmotions of different frequencies. For the derivation of the sought-after free cyclotron frequency via the Brown-Gabrielse invariance theorem, (2.8c), a measurement of all three eigenfrequencies is necessary. To this end, different techniques based on time-varying oscillating electric potentials applied to suitable electrodes that allow to couple and excite the states of the ion's motion were developed. As explained in sec. 2.2.1, the total electrical field can be decomposed into its multipole components. The most frequently used excitations are of dipolar and quadrupolar shape. In the following sections those will be discussed, as they are routinely used in the lab and for the measurements presented in chap. 4 and 5.

2.4.1. Dipole Excitation

The dipole excitation uses a time-dependent electric field with an, ideally, purely dipolar contribution. The excitation strength depends on the electric field at the position of the ion $\vec{E}_D$ which causes a force $\vec{F}_D$ on the ion, eq. (2.21). A dipolar excitation in axial direction[13] D_{z} can be realized by applying the voltage $V_{D_{\mathrm{z}}}(t)$ to an axially off-centered electrode, e.g. a correction or endcap electrode. This AC voltage has a frequency ω_{rf} and phase ϕ_{rf} with respect to the ion's eigenmotion and exerts a force on the ion:

$$\vec{F}_{D_{\mathrm{z}}}(t) = q\vec{E}_{D_{\mathrm{z}}(t)} = -q\frac{V_{D_{\mathrm{z}}}(t)}{d_{\mathrm{eff}_z}}\sin\left(\omega_{\mathrm{rf}}t + \phi_{\mathrm{rf}}\right)\vec{e}_z. \tag{2.36}$$

Following the approach of sec. 2.3.3, the eom (2.2c) is now modified and an analogy to a driven harmonic oscillator can be drawn [107]. Depending on the initial conditions, such as the phase relation, $\phi_z - \phi_{\mathrm{rf}}$, between the ion motion and the driving excitation field and the frequency difference $\omega_z - \omega_{\mathrm{rf}}$, the ion exhibits a transient response before reaching a steady state. The phase shift between the oscillation of the ion and the

[13] The same holds true for radial modes. In that case, the excitation has to be applied by a split or segmented ring electrode.

driving field depends on $\omega_z - \omega_{\mathrm{rf}}$, which in case of $\omega_z = \omega_{\mathrm{rf}}$ amounts to $\pi/2$. A phase is, therefore, imprinted to the ion's motion, that is used in phase-sensitive techniques, see sec. 5.6.

2.4.2. Quadrupole Excitation

Another excitation is the quadrupole excitation. The excitation field contains predominantly contributions of a quadrupolar field configuration and the resulting force on the ion can be written analogous to eq. (2.36):

$$\vec{F}_{Q_{\mathrm{xz}}}(x,z,t) = q\vec{E}_{Q_{\mathrm{xz}}(x,z,t)} = -q\frac{V_{Q_{\mathrm{xz}}}(x,z,t)}{d^2_{\mathrm{eff}_{\mathrm{xz}}}}\sin\left(\omega_{\mathrm{rf}}t+\phi\right)\left[z\,\vec{e}_x + x\,\vec{e}_z\right]. \tag{2.37}$$

Here, the force in the x-direction depends on the z-position and vice versa, which couples the radial and axial motion. This can be used to exchange [74, 108] energy between the modes[14] and therefore allows addressing also the radial modes even if only one axial resonator is used. An in depth derivation and discussion of the dynamics of this coupled system can be found in [74, 109, 111]. In the following paragraph a more general summary will be given.

The coupled eom resulting from the application of a quadrupolar field, resembles the time-dependent Schrödinger equation used for describing the dynamics of a quantum mechanical two-level system (e.g. an atom) perturbed by an oscillating electric field (e.g. light) [112]. As in the quantum mechanical case[15] (e.g. the interaction between a two level atom and light), under the condition of resonance this system also exhibits Rabi oscillations and a shift of the energy levels (dressed states and avoided crossing).

In the following the exemplary case of coupling between the axial and modified cyclotron respectively magnetron mode will be discussed.

Coupling at the red sideband, $\omega_{\mathbf{rf}} = \omega_+ - \omega_z$ resp. $\omega_{\mathbf{rf}} = \omega_- + \omega_z$:

During the coupling of the radial modes and axial motion at the red sideband, the amplitude of the motions is modulated by the Rabi frequency Ω [86]:

$$\rho_z(t) = \rho_{z,0}\,\sin\left(\frac{\Omega}{2}t\right)\sin\left(\omega_z t\ +\phi_z\right), \tag{2.38a}$$

$$\rho_\pm(t) = \rho_{\pm,0}\cos\left(\frac{\Omega}{2}t\right)\sin\left(\omega_\pm t+\phi_\pm\right). \tag{2.38b}$$

By the Rabi oscillations energy between the two coupled modes is exchanged with a rate Ω which describes the strength of the coupling:

$$\Omega = \frac{qV_{Q_{xz}}}{2md^2_{\mathrm{eff}_{\mathrm{xz}}}\sqrt{\omega_z\omega_+}}. \tag{2.39}$$

[14] More strictly speaking in the classical picture action $\oint p\mathrm{d}q$ is exchanged between the modes [109]. In the quantum mechanical picture, energy quanta of motion can be exchanged [110].

[15] As can be seen the occurrence of such a phenomena is not exclusive restricted to the realm of quantum mechanics but can also be found in such a classical system, see also [113].

If one mode of the ion is kept in thermal contact with the resonator and at the same time the quadrupole coupling drive is applied continuously, the energy content in both modes thermalizes with the resonator. Thereby both modes can be cooled and entropy is extracted from the system [110, 114]. This goes under the name of *sideband cooling*.

Because the magnetron mode is metastable and has inverted (negative) energy Landau levels (see fig. 2.7), the "red" sideband referring to the sideband that decreases the mode amplitude appears here at a coupling frequency, which is the sum of the axial and magnetron frequency, $\omega_{\mathrm{rf}} = \omega_- + \omega_z$. The energy of the magnetron motion is negative and the radius of the magnetron motion can be reduced by "pushing" the ion up the repulsive potential hill of the magnetron motion by increasing the ion's total magnetron energy [74]. Therefore, the resistive cooling introduced in sec. 2.3.3 does not work for the magnetron motion. However, applying the rf-coupling frequency at $\omega_- + \omega_z$ couples the magnetron and axial mode and therefore can be used to reduce the magnetron radius. In the thermal equilibrium between the two coupled modes, the time-averaged quantum numbers are equal [25, 74, 86], $\langle n_z \rangle = \langle n_\pm \rangle$, which by using eq. (2.11) yields for the energies the following relation:

$$\langle E_\pm \rangle = \pm \frac{\omega_\pm}{\omega_z} \langle E_z \rangle \,. \tag{2.40}$$

The modulation of the axial oscillation by $\frac{\Omega}{2}$ gives rise to a splitting of the axial dip signal [109] which leads a signal form called *double dip*, see fig. 2.5. The analogon in

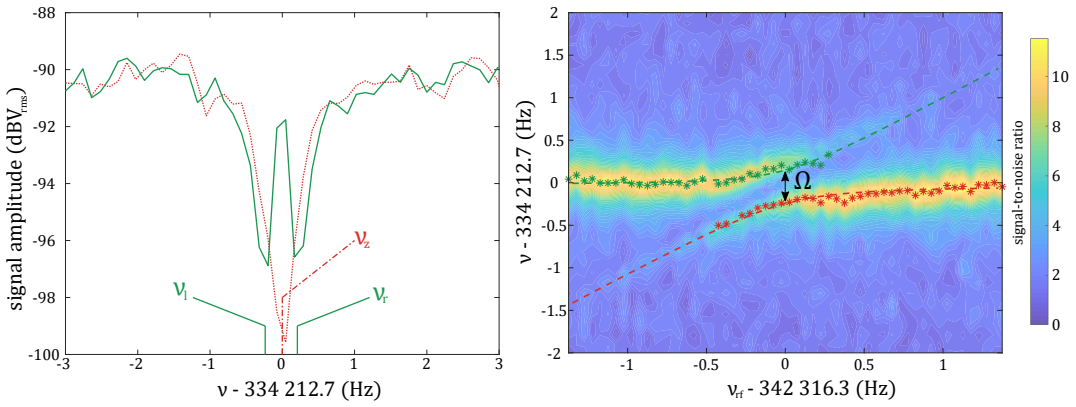

Figure 2.5.: **left** Single (red dotted) and magnetron double dip (green solid) for a $^9Be^+$ ion in the beryllium trap, see sec. 4.2. **right** Avoided crossing for the same ion. The difference at the minimal distance between the two curves corresponds to the strength of the coupling given by Ω. The dotted line is a fit according to eq. (2.41).

the two level atom-light interaction picture are repelling dressed states or an avoided crossing. The minimal splitting at resonance, $\omega_{\mathrm{rf},0} = \omega_\pm \mp \omega_z$ is equal to Ω. In case the

applied rf-frequency is detuned by δ from the optimal coupling frequency, $\omega_{\mathrm{rf}} = \omega_{\mathrm{rf},0} + \delta$, then the Rabi frequency Ω will be modified to $\tilde{\Omega} = \sqrt{\Omega^2 + \delta^2}$. The position of left and right double dip $\omega_{l,r}$ are shifted [86] (see also fig. 2.5, right):

$$\omega_{l,r} = \omega_z - \frac{1}{2}\left(\delta \pm \tilde{\Omega}\right) = \omega_z - \frac{1}{2}\left(\delta \pm \sqrt{\Omega^2 + \delta^2}\right). \tag{2.41}$$

As ω_{rf} is known and $\omega_{\mathrm{l,r}}$ and ω_z[16] can be determined from a single dip and a double dip spectrum, the above mentioned relation allows deriving the frequency of the radial mode to which the axial mode was coupled:

$$\omega_- = \omega_{\mathrm{rf}} + \omega_z - \omega_{\mathrm{l}} - \omega_{\mathrm{r}}, \tag{2.42a}$$

$$\omega_+ = \omega_{\mathrm{rf}} - \omega_z + \omega_{\mathrm{l}} + \omega_{\mathrm{r}}. \tag{2.42b}$$

Summarizing, this method allows measuring the radial frequencies or to exchange energy between two modes for cooling.

Coupling at the blue sideband, $\omega_{\mathrm{rf}} = \omega_z + \omega_+$ resp. $\omega_{\mathrm{rf}} = \omega_z - \omega_-$

If the coupling is chosen to be at the blue sideband, after a transient response to the drive, the amplitudes of the two coupled modes are exponentially increasing [115]. An explanation for this behavior can be derived by looking at the cooling and heating rates for two coupled quantum mechanical harmonic oscillator, as can be found in [25, 86]. After interaction with a photon of energy $E = \hbar(\omega_z \pm \omega_\pm)$, for an ion in an initial state with quantum number $|n_z, n_\pm\rangle$ a transition to the state $|n_z+1, n_\pm+1\rangle$ or $|n_z-1, n_\pm-1\rangle$ is possible, cf. fig. 2.7. The first transitions heats, whereas the second one cools the ion. The rates are proportional to the matrix element of the corresponding raising and lowering operators[17], $\left|\langle n_z+1, n_\pm+1|\, \hat{a}_z^\dagger \hat{a}_\pm^\dagger\, |n_z, n_\pm\rangle\right|^2 = (n_z+1)(n_\pm+1)$ respectively $|\langle n_z-1, n_\pm-1|\, \hat{a}_z \hat{a}_\pm\, |n_z, n_\pm\rangle|^2 = n_z n_\pm$. Because the rate for heating, which is proportional to $(n_z+1)(n_\pm+1)$ is larger than the cooling rate, $\propto n_z n_\pm$, the heating will dominate and due to the scaling with the quantum numbers n_i, an exponential growth of the radius is expected. The amplification of the amplitude of a mode under conservation of the phase information [108] is used in the phase-sensitive "PnA" technique [70]. There, the cyclotron and axial mode are coupled at the blue sideband and the final axial phase after such an exponential growth of axial amplitude depends on the initial phase of the cyclotron mode and the coupling pulse.

2.5. Continous Stern-Gerlach Effect

The previous sections described how to access the motional frequencies of the ion in the Penning trap, however, also the determination of the Larmor frequency is of crucial

[16] In order to mitigate drifts of ω_z due to fluctuations or drifts of the trapping voltage, a single dip for ω_z could be measured before and after a double dip spectrum, see [40].

[17] The raising and lowering operators are defined as $\hat{a}_i^\dagger |n_i\rangle = \sqrt{n_i+1}\, |n_i+1\rangle$ respectively $\hat{a}_i |n_i\rangle = \sqrt{n_i}\, |n_i-1\rangle$, where $i = [z, +, -]$.

importance. In the highly charged-ion systems typically used, namely hydrogenlike [4, 20, 21], lithiumlike [22, 23] or boronlike ions [27, 71], there is only one "valence"-like electron in the $1\,^2S_{1/2}$, $2\,^2S_{1/2}$ or $2\,^2P_{1/2}$ orbital[18]. Depending on the orbital the electrons occupy, the combination $\vec{j}$ of orbital angular momentum $\vec{l}$ and intrinsic spin angular momentum $\vec{s}$ will vary [54]. The projection value of the overall magnetic moment of the ion onto the magnetic field axis,

$$\mu^z = \mu_j^z + \mu_\rho^z = \underbrace{|\vec{\mu}_l + \vec{\mu}_s|^z}_{\text{spin-orbit coupling}} + \underbrace{\mu_+^z + \mu_-^z}_{\text{radial motion}}, \tag{2.43}$$

has different contributions. On the one hand, the motion of the ion in the radial plane creates a magnetic moment $\mu_\rho^z = \mu_+^z + \mu_-^z = \frac{q}{2m}\left(L_+^z + L_-^z\right)$ [86] depending on the axial component of the angular momenta $L_\pm^z = \omega_\pm \rho_\pm^2$ [72]. On the other hand, there is a magnetic moment $\mu_j^z = |\vec{\mu}_l + \vec{\mu}_s|^z$ [54] associated to a total angular momentum $\vec{j}$ resulting from the spin orbit coupling between the orbital angular momentum of the electron $\vec{l}$ and its intrinsic spin angular momentum $\vec{s}$. The projection value of the total magnetic moment μ_j^z onto the quantization axis defined by an external magnetic field[19] can only take the values:

$$\mu_j^z = -g_j m_j \mu_\mathrm{B}/\hbar, \tag{2.44}$$

where g_j is the bound electron (Landé) g-factor, μ_B is the Bohr magneton and m_j is the magnetic quantum number assigned to the $2j+1$ magnetic Zeeman sublevels in the range of $m_j = -|j|, -|j|+1, \ldots, j-1, j$. The energy degeneracy of the different eigenstates is lifted by the magnetic field and the energy difference between the Zeeman levels can be expressed by the Larmor frequency ω_L:

$$\Delta E = \hbar\omega_\mathrm{L} = g_j \mu_\mathrm{B} B. \tag{2.45}$$

Instrumental for the continuous Stern-Gerlach effect (CSGE) is that the coupling of the magnetic moment to the axial magnetic field B^z gives an additional magnetic potential $\Phi^\mathrm{mag} = -\mu^z B^z$. This alters the axial eom, eq. (2.2c), which leads to a superposition of forces acting on the ion arising from an electrostatic potential Φ^el, eq. (2.1), and a magnetostatic potential Φ^mag:

$$\ddot{z} = -\frac{q}{m}\nabla_z \Phi^\mathrm{el} - \frac{1}{m}\nabla_z \Phi^\mathrm{mag} = -\frac{q}{m} 2kz - \mu^z \nabla_z B^z. \tag{2.46}$$

If there is a magnetic inhomogeneity such that the gradient of the axial magnetic field component $\nabla_z B^z \to \nabla_z B^z(z)$ becomes a function of the axial position of the ion, the axial frequency ω_z will be different for different μ^z and therefore for different spin eigenstates of the electron, see eq. (2.44).

This force, as a consequence of the quantization of the spatial orientation of angular momentum, was for the first time observed in the famous Stern-Gerlach experiment

[18] Following the commonly used spectroscopic notation: $N\,^{2s+1}L_j$, where N is the principal quantum number, s is the total spin quantum number, L denotes the orbital angular quantum number and j refers to the total angular momentum quantum number.

[19] In laboratory colloquial terms often denoted as "spin up" or "spin down" for a $S_{1/2}$ or $P_{1/2}$ state.

[116]. The concept was adopted to measure the spin orientation of free electrons in a Penning trap by Dehmelt [117, 118]. In reference to the Stern-Gerlach experiment, he named this technique the continuous Stern-Gerlach effect (CSGE). It was later on also demonstrated for ions in the experiments at the University of Mainz [119]. For this purpose, a magnetic field inhomogeneity is superimposed onto the homogeneous trapping field $\vec{B} = (0, 0, B_0)$ in the shape of a magnetic bottle,

$$\vec{B}(z,\rho) = B_0 - 2B_1\vec{e}_z + \underbrace{B_2\left(\left(z^2 - \frac{\rho^2}{2}\right)\vec{e}_z - \rho z\vec{e}_\rho\right)}_{\text{magnetic bottle term}}. \tag{2.47}$$

It can be created by replacing the material of the central ring electrode of the trap by a ferromagnetic material with a high saturation magnetization [12], see fig. 2.6. The shift $\Delta\omega_z$ in axial frequency due to this interaction of magnetic moment and the magnetic bottle can be given by the following expression [84]:

$$\Delta\omega_z \approx \frac{B_2}{\omega_z m}\left(\Delta\mu_z^\rho + \Delta m_j g_j \mu_B\right). \tag{2.48}$$

By irradiating the ion with an electromagnetic radiation at the Larmor frequency that separates two spin states, transitions between these states can be driven resonantly, see fig. 2.6.

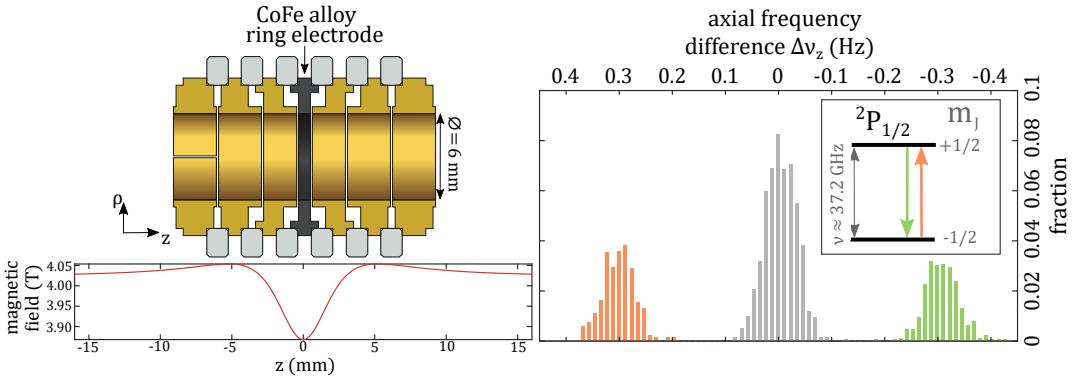

Figure 2.6.: **left** Schematic view of the analysis trap (AT) with the absolute value of the magnetic field $\left|\vec{B}\right|$ plotted along its center. **right** Histogram of axial frequency differences between subsequent axial frequency measurements upon rf-irradiation. Whereas $\Delta\nu_z = 0\,\text{Hz}$ indicates that no spin state transitions occurred, the two distributions around $\pm 300\,\text{mHz}$ correspond to spin state transitions between the two magnetic Zeeman substates of the $^2P_{1/2}$ manifold in the ground state of $^{40}Ar^{13+}$, see inset.

2.5.1. Double Trap Technique

As discussed in sec. 2.2.2, the presence of a B_2 component causes unwanted energy dependent frequency shifts and interferes with a precise determination of the motional frequencies. Therefore, the so-called double trap technique was introduced [120]. By using two different traps, distinct and spatially separated regions can be created. In one region the motional frequencies can be determined with highest precision while simultaneously to these measurements the frequency of the spin state transition is probed. In the second region the read-out (or analysis) and preparation of the spin state via the CSGE is performed. Hence, these two traps are typically named precision trap (PT) and analysis trap (AT), see fig. 3.2. For measurements in the respective traps, the ion can be transported adiabatically[20] between them [9]. A typical g-factor measurement scheme looks as follows:

1. The spin state is determined in the AT by back-to-back measurements of the axial frequency upon irradiation with a rf-frequency close to the Larmor frequency ω_L.

2. After a transport of the ion into the PT, the motional frequencies are measured to derive ω_c, eq. (2.8c), while simultaneously a single probing rf-frequency ω_rf in the vicinity of the Larmor frequency is irradiated. Since both the ω_c and ω_L are $\propto B_0$, the magnetic field dependency cancels in the ratio $\Gamma = \frac{\omega_\mathrm{rf}}{\omega_c}$.

3. Transport back into the AT where now the determined spin state is compared to the initial one of step 1 before probing in the PT.

4. Repeating step 1-3 multiple times while varying ω_rf allows to sample a distribution of frequency ratios $\Gamma^* = \frac{\omega_\mathrm{rf}}{\omega_c}$. By fitting a known model for the expected line shape of this resonance, $\Gamma = \frac{\omega_\mathrm{L}}{\omega_c}$ and therefore the g-factor can be derived. For details see e.g. [25, 40, 83].

Since the frequency shift $\Delta\omega_z$ due to a spin state transition, eq. (2.48), scales unfavorably with[21] the inverse mass, resolving those transitions[22] especially for heavy HCIs can be challenging and a magnetic bottle, given by its curvature B_2, is wanted to be as strong as possible. For the detection of $\Delta\omega_z$, a high resolution and stability in the axial frequency is required, imposing strict specifications on the used voltage sources [121] and also the usage of phase-sensitive methods becomes a necessity, see sec. 5.6. Furthermore, also the temperature in the radial modes, especially the cyclotron mode, see eq. (2.43), has to be as low as possible so that changes in the cyclotron mode causing axial frequency shifts does not mimic a spin flip. The heating rate in the cyclotron mode itself scales with the cyclotron energy. The latter reason among others triggered the implementation of sympathetic laser cooling, presented in sec. 2.7.3 and chap. 4.

[20] For the transport of the ion axially along the electrodes, adiabaticity is fulfilled if the rate of change of the transport voltages on the electrodes is much slower than the eigenfrequencies of the ion. In this case the classical action is conserved and the entropy does not change [72], see also sec. 2.7.1.

[21] Keeping the same axial frequency ω_z for different ions

[22] In the colloquial laboratory language often referred to as a “spin flip”.

2.6. Temperature of a Trapped Ion

In the context of high-precision measurements it is essential to have a detailed knowledge about the state parameters of the ion during the measurements. Such a parameter is the kinetic energy that relates to the temperature and amplitudes of motions, which can affect the achievable precision and also cause systematic uncertainties in the measurement, e.g. energy dependent frequency shifts, the line shape of g-factor resonances [122] or Doppler broadening of transitions, see 5.9.2. Therefore, in the following section, the concept of temperature for a single ion is first introduced and then the general idea of how to measure temperature is outlined. At the end, common techniques to alter the ion temperature are explained.

In classical statistical physics the temperature is typically introduced as an intensive state variable for an ensemble of a large number of N interacting constituents, such as atoms or molecules in a gas. This picture is difficult to maintain when assigning a temperature to a single trapped particle. However, it is possible to give a similar intuitive interpretation. As in the case for a gas where the temperature measures the mean kinetic energy $\langle E_{\mathrm{kin}} \rangle$, such as translational, rotational and vibrational energy of its constituents, a similar relation can be found between the total energy of the ion in a trap and its temperature and degrees of freedom. Of notice, as a major difference for the particle in the ideal Penning trap (sec. 2.1), the three eigenmodes are uncoupled and as a consequence different temperatures can be assigned to every mode independently. This degeneracy is lifted in a nonideal (real) Penning trap and a coupling between the modes exists (sec. 2.2). However, this coupling is on the one hand not strong enough to sufficiently redistribute energy between the modes by itself, but on the other hand it can be used for a measurement of a temperature in the single modes [123]. In sec. 2.3.3 and 2.3.4, the interaction between the ion and resonator was described. There it was stated that the ion is in thermal contact with the electron gas of the detector circuit and the interaction strength is characterized by the time constant τ, eq. (2.29b). In case of thermal equilibrium, typically reached after a time $t \gg \tau$, both should have the same temperature[23]. At this point the assumption of ergodicity of the system takes effect. Many repeated measurements of an observable O of a single particle equals one measurement of an ensemble of a large number of N particles, so the time-averaged $\langle O \rangle_t$ and ensemble-averaged $\langle O \rangle_N$ values are the same. If the system is ergodic, then the repeatedly measured energies of a single particle in thermal equilibrium with its environment of temperature T will follow a thermal Boltzmann distribution, $E \propto e^{-E/k_{\mathrm{B}}T}$, see fig. 2.7. From the Boltzmann distributed values a temperature T_i of the mode i (fig. 2.7) for the single ion can be derived. In addition, this can also be linked to the mean occupation number $\langle n_i \rangle$ in the description of a quantum harmonic oscillator, cf. eq. (2.11) [72]:

$$\langle n_i \rangle = \frac{1}{\exp\left(\frac{\hbar\omega_i}{k_{\mathrm{B}}T_i}\right) - 1}. \tag{2.49}$$

[23] Assuming no further heat source such as the intrinsic thermal noise of the detection electronics and amplifiers [25, 84]

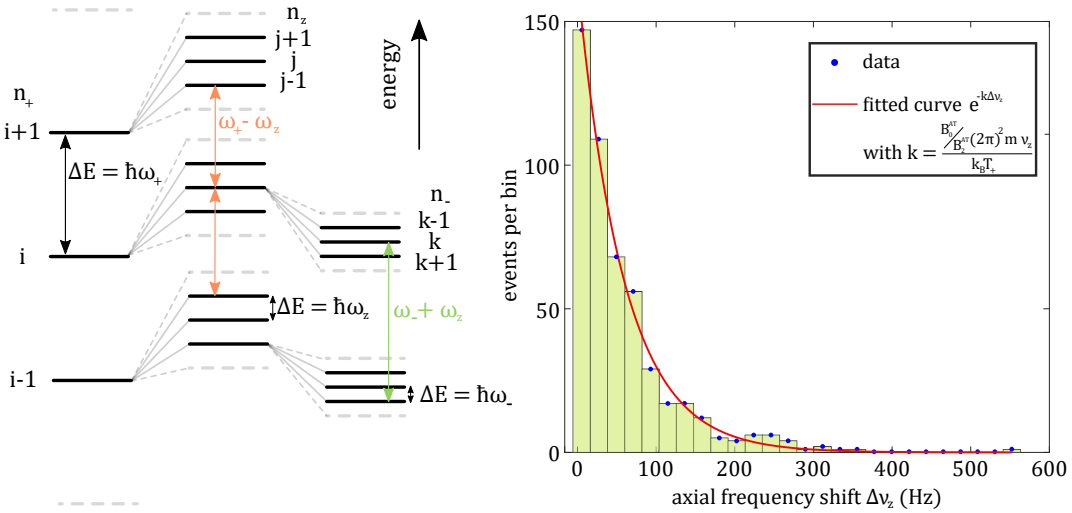

Figure 2.7.: **left** Energy level scheme of the harmonic oscillators for the eigenmotion of an ion in a Penning trap (not to scale). **right** Histogram of axial frequency shifts in the analysis trap caused by the thermally fluctuating amplitude of the cyclotron mode. This leads to a sizable axial frequency shift in the AT depending on the thermal radius of the cyclotron mode and the strength of the B_2^{AT}. The red solid line is a fitted Boltzmann distribution [123].

For this harmonic oscillator the classical relationship between the mean energy $\langle E \rangle$ and temperature T_i can be deduced as

$$T_i = \frac{\langle E_i \rangle}{k_\mathrm{B}}. \tag{2.50}$$

Furthermore, then the thermal amplitude $\rho_{\mathrm{th},i}$ can be given as the root-mean-square of the amplitude $\rho_{0,i}$:

$$\left\langle \rho_{0,i}^2 \right\rangle = \rho_{\mathrm{th},i}^2. \tag{2.51}$$

Using eq. (2.50) and eq. (2.51) together with the expression for the total energies in the respective modes, eq. (2.11), the thermal amplitudes read[24]:

$$\rho_{\mathrm{th},z/+} = \sqrt{\frac{2k_\mathrm{B}T_{z/+}}{m\omega_{z/+}^2}} \qquad \rho_{\mathrm{th},-} = \sqrt{-\frac{4k_\mathrm{B}T_-}{m\omega_z^2}} \tag{2.52}$$

As presented in sec. 2.4.2, coupling of modes via suitable rf-excitations can be used to transfer action between the modes in order to thermalize both coupled modes to the

[24] Because the magnetron motion is not stable, an increase in energy leads to a reduction of radius. From a thermodynamical point of view the entropy in the magnetron mode increases for decreasing energy, leading to a negative temperature [25].

resonator. Equivalent to relation (2.40) and by using eq. (2.8b), (2.11) and (2.52), the temperatures respectively thermal amplitudes in the respective modes for a coupling between axial and radial modes are given as:

$$T_{\pm} = \pm\frac{\omega_{\pm}}{\omega_z} T_z, \tag{2.53a}$$

$$\rho_{\mathrm{th},+} = \sqrt{\frac{\omega_z}{\omega_+}}\rho_{\mathrm{th},z} = \rho_{\mathrm{th},-} = \sqrt{\frac{2\omega_-}{\omega_z}}\rho_{\mathrm{th},z}. \tag{2.53b}$$

A more detailed discussion on how the temperature can be measured will be given in sec. 4.4.1 and 5.4 in which two different types of temperature measurements were actually performed on $^{9}\mathrm{Be}^{+}$ and $^{40}\mathrm{Ar}^{13+}$.

2.7. Further Cooling Methods

With techniques presented so far the achievable temperature is limited to around the temperature of the electron gas in the resonator and the connected detection circuitry. Besides the bolometric cooling introduced in sec. 2.3.3, further techniques are available that allow reducing the ion temperature even further. In the following section, three of these methods will be introduced. The adiabatic cooling, sec. 2.7.1, and negative feedback cooling, sec. 2.7.2, were used during the fine structure laser spectroscopy of $^{40}\mathrm{Ar}^{13+}$ (chap. 5). There they helped to reduce the achieved uncertainty of the optical transition frequencies. The third one is the laser cooling, whose implementation and demonstration of was another objective of this thesis (chap. 4).

2.7.1. Adiabatic Cooling

As can be seen from eq. (2.10) and (2.11) and also known from the mechanics of the one dimensional harmonic oscillator, the energy of a confined particle depends on the potential energy. Changing the potential energy is easiest for the axial mode, where the confinement is given solely by the electrostatic field and therefore also the trapping frequency $\omega_z \propto \sqrt{V_\mathrm{r}}$ only depends on the trapping voltage V_r, compare eq. (2.3). Assuming this potential is changed, e.g. lowered[25], by a factor of ξ to $\tilde{V}_\mathrm{r} = V_\mathrm{r}/\xi$, then the frequency changes accordingly to $\tilde{\omega}_z = \omega_z\sqrt{1/\xi}$. If the change of the trapping voltage is adiabatic, meaning that the change of the trapping frequency takes much longer than the period of an oscillation [72]

$$\left|\frac{1}{\omega_z}\frac{\mathrm{d}\omega_z}{\mathrm{d}t}\right| \ll \omega_z, \tag{2.54}$$

then the entropy is not changing, so $\tilde{n}_z = n_z$. It can be shown, that the axial component of the total angular momentum

$$L_z = \omega_z \rho_z^2 \tag{2.55}$$

[25] Lowered refers here to the trapping potential depth. Since V_r is negative for positively charged ions, it means V_r is increased absolutely, becoming less negative.

is an adiabatic invariant under adiabatic potential changes [72].

Because $\tilde{L}_z = L_z$ or $\tilde{n}_z = n_z$ and by using $E_z = \frac{1}{2} m\omega_z L_z$ or relation (2.11) and eq. (2.50) it can be seen that the temperature and energy of the ion is decreased by $\xi^{1/2}$, whereas the radius increases by $\xi^{1/4}$. This method was successfully applied for the optical spectroscopy of the fine structure transition in $^{40}Ar^{13+}$ as presented in sec. 5.9.2.

2.7.2. Negative Feedback Cooling

In sec. 2.3.4 it was shown that the ion can thermalize with the detector circuit via resistive dissipation of energy. The achievable temperature is therefore limited by the noise equivalent temperature of the detection circuit including amplifier, see fig. 2.3. As proposed in [124–126] and discussed in detail in [83, 127], by feeding back the detected signal with suitable amplitude and phase to the ion (fig. 2.8), the effective temperature of the ion can be brought below the thermal temperature of the resonator, at the cost of an increased cooling time constant [127]. Another way to manipulate the ion's motion is to apply a signal to the resonator itself instead of to one of the electrodes [84]. The

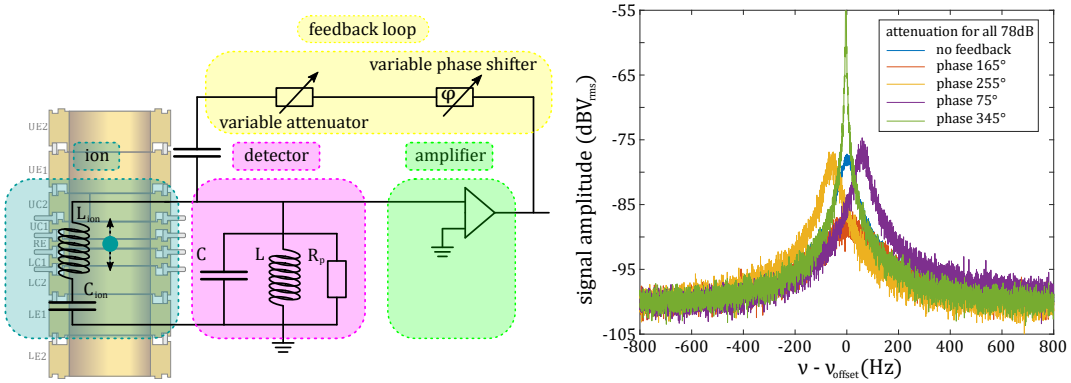

Figure 2.8.: **left** Schematic circuit diagram of the feedback loop. **right** Detector signal for different phases but same attenuation of the applied feedback. Four distinct cases can be identified: the SNR can be increased or decreased without changing the resonator frequency for two phases differing by 180° (red, green). The other two extremal cases differing by ±90° from the previous cases shift the resonance frequency of the resonator by the largest amount possible (yellow, purple).

lowest possible temperature achieved with this method is intrinsically limited by noise added from the feedback loop, dominated by the amplifier noise.

Using a newly developed ultra-low noise amplifier, with a voltage noise well below the thermal Johnson noise of the resonator, this method was successfully implemented in the predecessor experiment at the University of Mainz [83]. The signal is picked up after the first cryogenic amplifier and then fed back with a variable attenuation and

adjustable phase to the detection circuit via a capacitive coupling to the resonator circuit. By adjusting the feedback phase, the effective parallel resistance and capacitance of the detection circuit can be changed. Depending on the phase of feedback signal the resonance frequency of the resonator is slightly shifted, typically by a few resonator widths as demonstrated in [83, 84] and the signal-to-noise ratio (SNR) or Q-factor of the resonator is changed, see fig. 2.8. For negative feedback, the ion temperature can be below the thermal Johnson-Nyquist noise temperature of the resonator. The applicable negative feedback strength is limited by the voltage noise of the amplifier in the feedback loop. For a detailed discussion of electronic feedback see [83, 86, 127].

Same as for the adiabatic cooling, this technique was employed for the first time at ALPHATRAP in the optical spectroscopy measurements of $^{40}Ar^{13+}$ as presented in chap. 5.

2.7.3. Laser Cooling

The aforementioned methods are limited in the reachable temperatures or they are not applicable in every experimental situation. A commonly used technique to achieve lowest temperatures in atomic physics is laser cooling, typically applied to alkali atoms[26]. Because of the drastically changed scaling of electronic structure of HCI, they lack suitable transitions for laser cooling. Therefore, the method of sympathetic laser cooling is used, in which laser cooled auxiliary ions can be used to also cool the HCI under investigation. In the following paragraph, the general principle of laser cooling will be discussed and then expanded to application to an ion confined in a harmonic potential of a Penning trap and for sympathetic cooling.

Principle of Laser Cooling

Even though it was known before that light can cause a momentum change of massive particles, it took until the invention of the laser, that these narrow-band light sources allowed using this effect to alter the velocity distribution of a particle ensemble in order to cool it. In 1975, laser cooling was first independently suggested by Hänsch and Schawlow [128] for free atoms and by Wineland and Dehmelt [129] for trapped ions. The first demonstration of cooling ions stored in traps was shown in 1978. Neuhauser *et al.* at Heidelberg University [130] demonstrated laser cooling for an ensemble of <50 Ba^+ ions in a rf-quadrupole trap and Wineland *et al.* [131] at National Bureau of Standards, now National Institute of Standards and Technology (NIST), for Mg^+ ions in a Penning trap. Both succeeded soon after to cool a single trapped ion [132, 133]. In the following, the principal laser cooling techniques for Doppler laser cooling is outlined, mainly following [72, 112, 134, 135]. In order to give a qualitative description the following simplified assumptions are made:

- The ion is modeled as a two level system with ground state $|g\rangle$ and excited state $|e\rangle$ forming a closed cooling cycle transition. This is not the case for the later used

[26] In ion trapping experiments often singly charged ions of alkaline earth metals are used, e.g. Be^+, Mg^+, Ca^+, Sr^+ and Ba^+, but also Al^+, Hg^+, Yb^+,...

$^9Be^+$. The nucleus of ^9Be carries a nuclear moment of 3/2 which gives rises to a hyperfine structure, which is in addition altered by the strong magnetic field, details see sec. 4.1.

- The ion bound in the harmonic potential of the trap is in the so called *weak binding regime*, in which the natural linewidth of the transition Γ is much larger than the frequency of oscillation ω_i, $\Gamma \gg \omega_i$, and the Lamb-Dicke parameter $\eta = \left|\vec{k}\right| \rho = \frac{2\pi}{\lambda}\rho \gg 1$ [72]. This means that the lifetime of the excited state $\tau = \frac{1}{2\pi\Gamma}$ is much shorter compared to one period of oscillation and the ion-light interaction can be considered to be instantaneous and equivalent to the case of a free ion [134]. The parameter η describes the ratio between the wavelength λ of the laser light and the amplitude of motion ρ or rather the spatial extent of the motional wave function of the ion. In this case, sidebands are not resolved. In typical experiments with laser cooled trapped ions, for efficient cooling fast, short-lived, dipole transitions are used in the first stage of cooling and condition above holds true. This is also referred to as Doppler cooling regime. If one would like to approach the motional ground state, typically a second stage of cooling is needed in which either electromagnetically induced transparency (EIT) or stimulated Raman transitions or narrow dipole forbidden transitions are used [135]. The weak binding criterion is fulfilled for the axial laser cooling of $^9Be^+$, however it is not fulfilled for the spectroscopy of the dipole forbidden fine structure transition in $^{40}Ar^{13+}$, where $\Gamma \ll \omega_i$ which gives rise to a sideband structure as discussed in sec. 5.3.

Considering the current design of ALPHATRAP (fig. 3.2), strong geometrical constraints for laser access are given. At the time the experiment was performed, it was only possible to bring in the laser beam from the bottom, aligned with the vertical trap axis and parallel to the axial motion of the ion. Therefore, in the following discussion we will restrict the explanation of the laser cooling to the axial dimension[27]. Using the assumptions above, following simplified picture can be given:

The ion has a resonant fast electric dipole transition, $|g\rangle \leftrightarrow |e\rangle$, separated by an energy of $\hbar\omega_0$ in the eigenframe of the ion. The laser light is modeled as a monochromatic classical plane wave with frequency ω and wave vector $\vec{k}$, $\left|\vec{k}\right| = \frac{\omega}{c} = \frac{2\pi}{\lambda}$, with c being the speed of light. In order to excite the transition resonantly, the laser frequency has to match the transition in the proper rest frame of the ion, e.g. in case it is moving at a velocity v_z in the axial direction parallel to the laser beam, then the resonance condition reads:

$$\omega + \delta = \omega_0 + k_z v_z. \tag{2.56}$$

So for an ion moving towards the laser beam the laser detuning δ has to be negative towards the lower (red) frequency side of the transition. For a free ion (weak binding) moving at velocity $\vec{v}$ one scattering event, consisting of absorption of a photon with momentum $\hbar k$ and re-emission of a photon with wave vector $\vec{k}_s$, will change the velocity

[27] Which is sufficient for explaining the principle. Other geometrical arrangements are then discussed in the paragraph afterwards

of the ion to $\vec{v}'$. Energy and momentum must be conserved which yields for the change of the ion velocity $\Delta\vec{v}$ and energy ΔE in the nonrelativistic limit ($\frac{v}{c} \ll 1$) [72, 136]:

$$\Delta\vec{v} = \vec{v}' - \vec{v} = \frac{\hbar\left(\vec{k} - \vec{k}_s\right)}{m}, \tag{2.57a}$$

$$\Delta E = \frac{1}{2}m\left(\vec{v}'\right)^2 - \frac{1}{2}m\vec{v}^{\,2} = \frac{\hbar^2\left(\vec{k} - \vec{k}_s\right)^2}{2m} + \hbar\left(\vec{k} - \vec{k}_s\right)\vec{v}, \tag{2.57b}$$

$$\Delta E \overset{|\vec{k}|\approx|\vec{k}_s|}{\simeq} R\left(\hat{k}^2 - 2\hat{k}\hat{k}_s + \hat{k}_s^2\right) + \hbar\left(\vec{k} - \vec{k}_s\right)\vec{v}. \tag{2.57c}$$

For the last equation it was assumed $|\vec{k}| \approx |\vec{k}_s| = k$. The recoil energy $R = \frac{\hbar^2 k^2}{2m}$ is the kinetic energy a particle at rest gains upon absorption of a photon. $\hat{k} = \frac{\vec{k}}{k}$ and $\hat{k}_s = \frac{\vec{k}_s}{k}$ denotes the units vectors.

From eqs. (2.57) it can be seen that for stimulated emission in which the re-emitted photon is collinear with the incoming photon $\vec{k} = \vec{k}_s$, no net momentum is transferred. In the case of spontaneous emission, the net momentum transfer averaged over many scattering events is $\hbar k$ per photon in the direction of the laser beam. The ion velocity is consequently reduced each time by the recoil velocity $\Delta v_r = \frac{\hbar k}{m}$.

Even though initially a two-level ion was assumed, in practice this can only be approximately true. One possible realization, which is the case also in the Penning trap, is to have a strong magnetic field, so that the Zeeman splitting between adjacent magnetic sublevels is much larger than the natural linedwidth or the Doppler broadening of the used transition. This way, pairs of individual magnetic sublevels can form effectively a two-level system. Due to selection rules for optical transitions [54], different magnetic sublevels can be addressed by choosing an appropriate polarization. The probability P_s[28] for re-emission into a solid angle $\mathrm{d}\Omega$ in the direction of $\hat{k}_s$ for a dipole transition is given by [72, 136]:

$$P_s(\hat{k}_s)\mathrm{d}\Omega = \frac{3}{8\pi}\sum_i \int \left|\hat{d}_{ge}\hat{\epsilon}_i\left(\hat{k}_s\right)\right|^2 \mathrm{d}\Omega, \tag{2.58}$$

where the orientation of the electric dipole moment of the transition is $\vec{d}_{ge} = \langle g|\,\vec{d}\,|e\rangle$ with unit vector $\hat{d}_{ge} = \frac{\vec{d}_{ge}}{|\vec{d}_{ge}|}$ and $\hat{\epsilon}_i$ are the two unit vectors of polarization. For linear polarized light ($\Delta M = 0$) the angular distribution becomes $P_s(\hat{k}_s) = \frac{3}{8\pi}\sin^2(\theta_s)$ and for circular polarized light ($\Delta M = \pm 1$) $P_s(\hat{k}_s) = \frac{3}{16\pi}\left(1 + \cos^2(\theta_s)\right)$, with θ_s defined as angle between the magnetic field $\vec{B}$ and $\vec{k}_s$, so that $\cos(\theta_s) = \hat{B}\cdot\hat{k}_s$. Because of the symmetry $P_s(\hat{k}_s) = P_s(-\hat{k}_s)$ and using eq. (2.57c) the average net change of energy per scattering event can be given by:

$$\langle\Delta E\rangle = R\left(1 + f_s\right) + \hbar\vec{k}\vec{v},\ f_s = \int P_s(\hat{k}_s)\hat{k}_s^2\mathrm{d}\Omega. \tag{2.59}$$

[28] Normalzied as $\int P_s(\hat{k}_s)\mathrm{d}\Omega = 1$

The rate of scattering events $\Gamma\rho_{ee}$ is given by the rate of spontaneous decay Γ and the probability of being in the excited state $\rho_{ee} = \langle e|\,\hat{\rho}\,|e\rangle$ [112]:

$$\rho_{ee}(v) = \frac{S/2}{1 + S + \left[2\left(\omega - \omega_0 - \vec{k}\vec{v}\right)/\Gamma\right]^2}, \tag{2.60}$$

where $S = \frac{2|\Omega_R|^2}{\Gamma^2}$ is the saturation parameter with Ω_R being the on-resonance Rabi frequency. Combining eq. (2.59) and (2.60) a cooling rate can be given as a function of an effective average scattering force $F_a = \hbar k \Gamma \rho_{ee}$ [72, 135]:

$$\left\langle \left.\frac{\mathrm{d}E}{\mathrm{d}t}\right|_{\mathrm{cool}} \right\rangle = \langle \Gamma\rho_{ee}\Delta E\rangle = \langle F_a v\rangle = \Gamma \frac{S/2\left[R\,(1+f_s) + \hbar\vec{k}\vec{v}\right]}{1 + S + \left[2\left(\omega - \omega_0 - \vec{k}\vec{v}\right)/\Gamma\right]^2}. \tag{2.61}$$

For small velocities v (close to the final temperature) it can be expanded [135]:

$$\left\langle \left.\frac{\mathrm{d}E}{\mathrm{d}t}\right|_{\mathrm{cool}} \right\rangle = \langle \hbar k \Gamma \rho_{ee}(v) v\rangle \overset{v\to 0}{\simeq} F_0\left(\langle v\rangle + \kappa\left\langle v^2\right\rangle\right) = F_0\kappa\left\langle v^2\right\rangle, \tag{2.62}$$

with the scattering force $F_0 = \hbar k \Gamma \rho_{ee}(v=0)$ and the friction coefficient $\kappa = \frac{8k\Delta/\Gamma^2}{1+S+(2\delta/\Gamma)^2}$. In the last step, $\langle v\rangle = 0$ was used that applies to an ion confined in a trap.

In reality, the cooling does not reach zero energy and temperature. Each re-emission gives a change $\Delta\vec{p}_s$ in momentum of $\hbar\vec{k}_s$ and therefore the ion undergoes a random walk in momentum space, which is referred to as the photon recoil limit. Due to the symmetry of the emission process, the average change of momentum $\langle\Delta\vec{p}_s\rangle = 0$, but as known from other diffusion processes[29] for large number of recoils N, the mean square displacement[30] $\left\langle(\Delta\vec{p}_s)^2\right\rangle \neq 0$ and $\left\langle(\Delta\vec{p}_s)^2\right\rangle \propto \hbar^2\vec{k}_s^2 N$ [135]. For $v\to 0$, this can be expressed in a heating rate, taking the geometrical re-emission pattern into account:

$$\left.\frac{\mathrm{d}E}{\mathrm{d}t}\right|_{\mathrm{heat}} = \frac{\hbar^2k^2}{2m}\Gamma\rho_{ee}(v=0)\,(1+f_s)\,. \tag{2.63}$$

The lowest achievable temperature is reached when the cooling and heating rates are equal and one can show [72, 135] that the achievable final mean energy is

$$\langle E\rangle_{t\to\infty} = \frac{\hbar\Gamma}{8}\,(1+f_s)\left[(1+S)\,\frac{\Gamma}{4\,(\omega_0-\omega)} + \frac{(\omega_0-\omega)}{\Gamma}\right] = \frac{1}{2}k_BT, \tag{2.64}$$

which is minimal at a detuning of $(\omega_0 - \omega) = \frac{\Gamma}{2}\sqrt{1+S}$ and the final minimal equilibrium temperature $T_{\min}$ is [135]:

$$T_{\min} = \frac{\hbar\Gamma\,(1+f_s)}{4k_B}\sqrt{1+S}. \tag{2.65}$$

[29] Assuming the transition is driven weakly, $S \ll 1$, so that absorption and emission are uncorrelated, otherwise the diffusion will be altered.

[30] The mean kinetic energy can be written as as $\langle E_{\mathrm{kin}}\rangle = \frac{1}{2}k_{\mathrm{B}}T = \frac{\langle\Delta p^2\rangle}{2m}$

The condition that cooling and heating rate reach a steady state is only given in the direction of the laser beam, e.g. the axial direction in our case. This means the motions perpendicular to it, the radial modes, do not get cooled and are even heated by the recoil after re-emission. Therefore, to obtain cooling in all modes the arrangement of the laser beam has to be different [136] or mode coupling techniques have to be used. How this situation for laser cooling in a Penning trap can be improved will be discussed in the subsequent section.

Laser Cooling in Penning Traps

In the previous section, the restricted case of laser cooling along one dimension (here in the axial direction of motion of the ion) was discussed. An extension of this description to other beam alignment configurations using a similar formalism as in eq. (2.57)-(2.59) can be found in [136] and is here summarized shortly. As mentioned before, cooling should refer here to a reduction of the motional amplitudes, which means for the axial and cyclotron mode to reduce also the energy, whereas for the magnetron mode to increase the energy. In order to address also the radial modes, the laser beam needs a component with nonvanishing projection value on the radial plane. This can be done by using more than one laser beam, e.g. one beam in axial and another one in the radial plane, or by using a single laser beam which is not parallel to only the axial or radial directions and hitting the ion under an oblique angle [136] as first demonstrated in [133, 137]. For a reduction of the magnetron amplitude, the ion has to gain energy in the magnetron mode. That is why the ion is supposed to scatter the photons primarily when receding from the laser beam. The opposite is the case for the cyclotron mode, which should scatter the photons when propagating against the direction of the laser beam. Having a look at the solutions of the eom, eq. (2.9), magnetron and cyclotron motion have the same direction of rotation. Therefore this condition can only be met when the intensity of the laser beam is higher on the side of motion in which the magnetron mode recedes from the laser beam [133, 136]. This means that for beams with a symmetric Gaussian intensity distribution typically used, the beam needs to be offset with respect to the center of ion motion, which requires a very well control over the size and positioning of the beam inside the trapping region.

Another possibility is to use a suitable combination of laser cooling and mode coupling techniques (similar to sec. 2.4.2). It was discussed in [138, 139] and demonstrated [140, 141], such that cooling of both radial modes can also be obtained with one laser beam directed through the center of the trap.

Sympathetic Cooling

Because directly accessible laser cooling transitions (fast dipole allowed optical transitions) are not present in HCI, laser cooling can only be accomplished via one or several auxiliary ions. The basic idea is that one kind of species, that is cooled efficiently, is in thermal contact with another one and exchanges energy so that the overall system is cooled down to an equilibrium state. Using this principle with laser cooled ions has

already been demonstrated in the first experiments with few laser cooled ions[31] in a Penning trap by Coulomb collisions between different isotopes of the same ion species [137] or different ion species [143] in the same trap potential. The interaction between the ions is based on the mutual Coulomb interaction. For this, they do not necessarily have to be stored in the same trapping potential. As discussed in sec. 2.3 the ion exhibits also an interaction with the trap electrodes via induced image currents, which cannot only be used for detection but also for coupling two different ion species stored in separate trap potentials [144]. Therefore, one can distinguish between two cases:

A The interaction is mediated indirectly via shared trap electrodes, typically an endcap of two adjacent traps.

B The mixture of two ion species in the same potential well where they directly interact via Coulomb forces which can even lead to the phenomenon of Coulomb crystallization.

Case A — Coupling via shared electrode

The idea goes back to a proposal of "coupled traps", discussed in [144]. In this scheme, ions are in two separate traps next to each other, but share the same endcap electrode. As shown in sec. 2.3, the two ions can exert forces on each other via their image currents induced on the shared endcap electrode. Because the ions share the same endcap, they are then axially coupled. This system can be mathematically described as two coupled oscillators and in the equivalent electric circuit picture the coupling is modeled by a parallel capacitance C_T [144, 145]. In this description the capacitance $C_{\mathrm{ion},j}$, eq. (2.32a), which can be assigned to the ions[32] ($j=1$ or 2) is reduced by the coupling to

$$C'_{\mathrm{ion},j} = \frac{C_{\mathrm{ion},j} C_\mathrm{T}}{(C_{\mathrm{ion},j} + C_\mathrm{T})}, \tag{2.66}$$

which changes also the frequency of the ions to $\omega'_{zj} = \left(L_{\mathrm{ion},j} C'_{\mathrm{ion},j}\right)^{-1/2}$. The strength of the coupling K can be parametrized by $K = \left(L_{\mathrm{ion},1} L_{\mathrm{ion},2} C_\mathrm{T}^2\right)^{-1/2}$, where $L_{\mathrm{ion},j}$ is the inductance of ion j. The general solution of the eom is oscillating at a frequency given by:

$$\Omega_{1,2}^2 = \frac{1}{2}\left[\left(\omega'_{z1}\right)^2 + \left(\omega'_{z2}\right)^2\right] \pm \frac{1}{2}\left[\left(\left(\omega'_{z1}\right)^2 - \left(\omega'_{z2}\right)^2\right)^2 + 4K^2\right]^{1/2}. \tag{2.67}$$

The two ions can be easily brought into resonance by adjusting the trapping potential such that $\omega'_{z1} = \omega'_{z2} = \omega'_z$. If additionally $K \ll \omega_z$, then $\bar{\Omega} = (\Omega_1 + \Omega_2)/2 \simeq \omega'_{z1} \simeq \omega'_{z2}$ and the energy is exchanged at a rate

$$\Omega_{ex} = \frac{1}{2}(\Omega_1 - \Omega_2) \simeq \frac{\bar{\Omega}\sqrt{C'_{\mathrm{ion},1} C'_{\mathrm{ion},2}}}{2C_\mathrm{T}} \simeq \frac{1}{2\bar{\Omega} C_\mathrm{T} \sqrt{L_1 L_2}} \overset{(2.32)}{=} \frac{|q_1 q_2| \sqrt{N_1 N_2}}{2C_\mathrm{T} \omega_z d_{\mathrm{eff}1} d_{\mathrm{eff}2} \sqrt{m_1 m_2}}. \tag{2.68}$$

[31] Other prominent example is the cooling of protons or antiprotons with electrons in a nested trap [126, 142]

[32] For a number of N ions in one trap, eqs. (2.32) change and $L_\mathrm{i}^N = L_\mathrm{i}/N_\mathrm{i}$ and $C_\mathrm{i}^N = C_\mathrm{i} N_\mathrm{i}$

If one ion species is now laser cooled, the ions in the second trap, e.g. HCIs can thermalize with the laser cooled ions which effectively then act as heat sink for the HCIs. The description given above was derived for the axial mode of the ions motion. However, as shown in sec. 2.4.2, different modes can be parametrically coupled, allowing also re-thermalization of the other modes and eventually cooling them. Implementation of this method is currently pursued at the proton g-factor experiment at the University of Mainz [145, 146].

Case B — Coupling in same trap potential and Coulomb Crystallization

In an alternative approach, the sympathetically and directly cooled ions can be stored in the same trapping potential. The ions exchange momentum directly via Coulomb forces and this way can reach a state of thermal equilibrium. If the temperature of the ions in the trap is high, the motion of the ions are uncorrelated. The ions follow their individual trajectories and Coulomb collisions between the ions happen at random times [72].

If the temperature is low enough or the particle density high enough, the description as independent particles breaks down and the ions can undergo a phase transition from a gaseous phase to an ordered crystalline like structure [147], called a *Coulomb crystal*. In this conformation the ion motion is strongly correlated and their positions are fixed in space with respect to each other in a crystal-like manner. Coulomb crystals of HCI in a Penning trap were first observed for Xe^{44+} ions sympathetically cooled by laser cooled $^9Be^+$ [148].

Even though larger Coulomb ion crystals are of interest to a wider community for the implementation of a quantum simulator in these crystalline structures [149–151], the envisaged scheme [9, 69] for ALPHATRAP would require a two ion crystal consisting of a HCI and a $^9Be^+$ ion. The inter-ion spacing depends on the ratio of trapping potentials and Coulomb repulsion. For a configuration of a two-ion crystal (of a laser cooled ion and a HCI), the ions are arranging such that the potential energy in the trapping field is minimized. The Coulomb crystal formed by two ions can take two distinct different orientations, depending on the trap parameters. For a strong axial confinement ($6\omega_z^2 > \omega_c^2$), corresponding to a large trapping voltage, the crystal will be oriented in the radial plane and rotate about the center-of-mass close to the magnetron frequency. For a lower trapping voltage, such that $6\omega_z^2 < \omega_c^2$, the two-ion crystal can align in axial direction [152]. In the case of a crystal orientated parallel to the axial direction, the total potential energy E_{pot} of the two ions is altered by the mutual Coulomb repulsion and reads [153]:

$$E_{\mathrm{pot}} = \frac{1}{2} m_1 \omega_{z_1}^2 z_1^2 + \frac{1}{2} m_2 \omega_{z_2}^2 z_2^2 + \frac{q_1 q_2}{8\pi\epsilon_0 |z_1 - z_2|}. \tag{2.69}$$

For the equilibrium position E_{pot} is minimized, $\frac{\partial E_{\mathrm{pot}}}{\partial \rho_{z_1}} = \frac{\partial E_{\mathrm{pot}}}{\partial \rho_{z_2}} = 0$, so that inter-ion distance z_{12} can be calculated by:

$$|z_1 - z_2|\, z_{12} = \left(\frac{(q_1 + q_2)\, d^2}{8\pi\epsilon_0 V_{\mathrm{r}} C_2} \right)^{1/3}. \tag{2.70}$$

The production of ion Coulomb crystals with only two $^{40}Ca^{+}$ ions was demonstrated [154, 155] and the conditions for the creation treated in [152]. In the configuration as two-ion Coulomb crystal, the equilibrium distance between a laser cooled $^{9}Be^{+}$ and a HCI is typically only a few ten µm, so that the magnetic field difference resulting from residual magnetic field inhomogeneities at the locations of the ions is drastically reduced. This enables ultra-precise determination of g-factor differences [9, 69].

3. Experimental Setup

In this chapter the setup of the ALPHATRAP apparatus used in this thesis is described. The idea to build the ALPHATRAP experiment originated from the g-factor experiment at the University of Mainz, see sec. 1.1.2. There the production of HCIs was done by an in-trap electron beam ion source (EBIS) [156] attached to the lower end of the Penning-trap tower [25, 83], which was inside a hermetically sealed cryogenic vessel. The production of lithium- or hydrogenlike HCIs was therefore limited by the achievable ionization energies reachable by the EBIS. The maximum electron beam energy was around 5.5 keV [25], allowing the production of HCIs up to lithiumlike calcium $^{40,48}Ca^{17+}$ [23]. In order to extend the successful g-factor measurements from the Mainz experiment [4, 20–23] to even heavier HCIs, the idea of ALPHATRAP emerged [157].

For ALPHATRAP many design ideas and experience from the Mainz experiment were incorporated and evolved. A distinct feature of ALPHATRAP is the possibility to inject HCIs from external ion sources. HCIs are typically produced in electron beam ion traps (EBIT) or accelerator based facilities, like the HITRAP facility at GSI [158, 159], Darmstadt. Such EBITs [160–162] are also available in the group of J. Crespo, part of the neighboring division of Prof. Pfeifer at the Max-Planck-Institut für Kernphysik (MPIK), Heidelberg. As a logical consequence the ALPHATRAP apparatus was built at MPIK, close to these ion sources. This chapter will give an overview of the experimental setup, a more in depth description or additional information can also be found in [9, 40, 84].

3.1. Ion Sources

ALPHATRAP enables the injection of arbitrary ions from external ion sources via a room temperature ultra-high vacuum beamline (fig. 3.1). As ion sources, two EBITs and one laser ablation ion source are connected to the beamline. These sources give potentially access to all possible charge-to-mass ratios of all elements ultimately up to hydrogenlike lead $^{208}Pb^{81+}$ from the Heidelberg-EBIT [160, 161].

3.1.1. Electron Beam Ion Trap (EBIT)

In an electron beam ion trap HCI are readily produced which is elsewise only possible in accelerator based facilities. The target material for ionization is typically injected as a gas into a high-energy and -intensity electron beam. Ionization occurs by electron impact and the created ions are trapped in a structure of cylindrical electrodes (drift tubes) on which a strong magnetic field is superimposed. By applying suitable voltages to those drift tubes the ions can be stored in the axial direction. The radial confinement is ensured by the strong magnetic field and by space-charge of the electron beam crossing the

trapping region. The continuous beam of electrons is compressed to a smaller diameter by the magnetic field in order to achieve a higher current density. It goes through the trap and ionizes the ions to higher charge states. This process stops once the required energy for the next ionization step is larger than the electron energy or until ionization and recombination rates are equal [163]. By switching the drift tubes on one side of the trap to lower potentials the ions can be ejected into a beamline and guided towards different experimental stations, among others the Penning-trap experiment. Because the ejected ion bunch contains a variety of charge-over-mass states, q/m, a selection of the q/m is done by using either a Wien filter [164] placed behind the HC-EBIT, or a 90° separator magnet which is installed behind the Heidelberg-EBIT.

Heidelberg Compact-EBIT

The Heidelberg Compact-EBIT (HC-EBIT) [162] uses permanent magnets for the creation of the magnetic field. This allows low-cost fabrication and operation as well as a small footprint of less than $0.4\,\mathrm{m} \times 0.4\,\mathrm{m}$. It is operated at room temperature and requires low maintenance. The NdFeB magnets are stacked around the trapping center region on a soft iron yoke, which focuses the magnetic flux into the trapping region, giving a maximum magnetic field strength of about 0.74 T. Typical parameters of operation are an electron beam current of $<8\,\mathrm{mA}$ and the voltages applied to the cathode emitting the electron beam are typically around $-1.5\,\mathrm{kV}$ and around $2\,\mathrm{kV}$ for the drift tubes. These settings allow the production of HCI from argon and xenon gas up to $^{40}\mathrm{Ar}^{16+}$ and $^{129}\mathrm{Xe}^{37+}$ [162, 165]. The device operated at ALPHATRAP is a prototype of several HC-EBITs currently operating in other experiments [42, 166, 167]. The $^{40}\mathrm{Ar}^{13+}$ used in the first measurement campaign [27, 40] of ALPHATRAP and also reported on in this thesis (chap. 5) are produced by this HC-EBIT.

Heidelberg-EBIT

The uniqueness of ALPHATRAP lies in the connection of the experimental setup to a potent ion source like the Heidelberg-EBIT [160, 161], which will be the main source of HCI in the future. Its design includes a projected electron beam energy up to 150 keV and an electron beam current $>500\,\mathrm{mA}$, being able to produce HCI up to hydrogenlike lead, $^{208}\mathrm{Pb}^{81+}$. In contrast to the smaller HC-EBITs, the Heidelberg EBIT employs a superconducting magnet structure producing a central magnetic field of up to 9 T. At the present stage, the Heidelberg-EBIT is in its re-commisioning phase and beam energies of 70 keV were reached. Even though currently operating below the final goal of producing hydrogenlike lead, the currently achieved beam energy enables a plethora of intriguing and unique measurements with HCI, e.g. hydrogenlike HCI up to $^{132}\mathrm{Xe}^{53+}$ or lithiumlike bismuth $^{209}\mathrm{Bi}^{80+}$, not accessible for high-precision Penning-trap experiments before.

3.1.2. Laser Ion Source

As third ion source, a laser ablation ion source (LIS) was developed and built in the group [9, 168] based on earlier designs [169]. By using a high-intensity laser pulse from a frequency double Nd:YAG laser system, atoms can be ablated from a solid target material and ionized in a plasma fume around the ablation spot. For this process to occur, the applied power density has to be $>1\times10^8\,\mathrm{W/cm^2}$ [168], which can be easily fulfilled by the laser system exhibiting a maximum pulse energy of 35 mJ at 532 nm, a pulse length of about 7 ns and a focal spot size <250 µm. Ions can be extracted from the plasma and accelerated with a three stage electrode system, which allows to have an adjustable time-focal-point [170]. For beam focusing and guiding, einzel lenses and deflector electrodes are incorporated into the LIS. A motorized stage allows to translate the target holder and change the produced ion species in situ. So far the production of singly charged carbon, aluminium and beryllium ions were demonstrated [168]. The $^9Be^+$ ions necessary for the experiments of sympathetic laser cooling are delivered by the LIS.

3.2. Beamline

The transport of the HCI from their sources to the Penning trap is done in an ultra-high vacuum (UHV) beamline. A residual gas pressure as low as possible is in fact necessary not only for the measurements with HCI, but also for the transport of the HCIs to the Penning-trap system. The lifetime of a HCI depends on its charge state [171] and therefore a range of measures is taken to ensure superb vacuum conditions to inhibit the loss of a HCI due to recombination with rest gas atoms. For the production of such vacuum conditions different kinds of vacuum pumps, such as turbomolecular, ion-getter and non-evaporative getter pumps, are employed. All materials used in the beamline are selected to allow for an in-situ bake out of the beamline to temperatures of 300 °C. The largest partial pressure in the remaining residual gas is from hydrogen that outgasses from stainless steel parts. The content of hydrogen gas is reduced by a diligent selection of steel grades, which are in addition vacuum fired (950 °C at $<1\times10^{-5}$ mbar for >1.5 h).

For guiding the bunched ion beam through the beamline, ion optical elements like segmented einzel lenses [172] and two quadrupole 90° benders [173] are used (fig. 3.1). For the diagnosis and visualization of the beam microchannel plate (MCP) detectors are used, mounted together with Faraday cups on a retractable stage which can be moved into the beam [9]. Because the extraction potential from the EBITs is typically several kV, stopping the ions would require potentials of the same magnitude inside the trap, which is not possible. Therefore the ions are decelerated to energies of about $q\cdot150\,\mathrm{V}$ by a pulsed drift tube located in the vertical section above the magnet (fig. 3.1). The slowed down ions can then be caught in the capture trap.

Due to the cryopump and cryo-adsoprtion effect in the cryogenic trapping region, the residual gas pressure is $<1\times10^{-17}$ mbar [9, 84] and thus orders of magnitude lower than in the directly connected beamline. Such low pressures are reached in other cryogenic trap experiments, however they have a trapping region hermetically sealed by either a

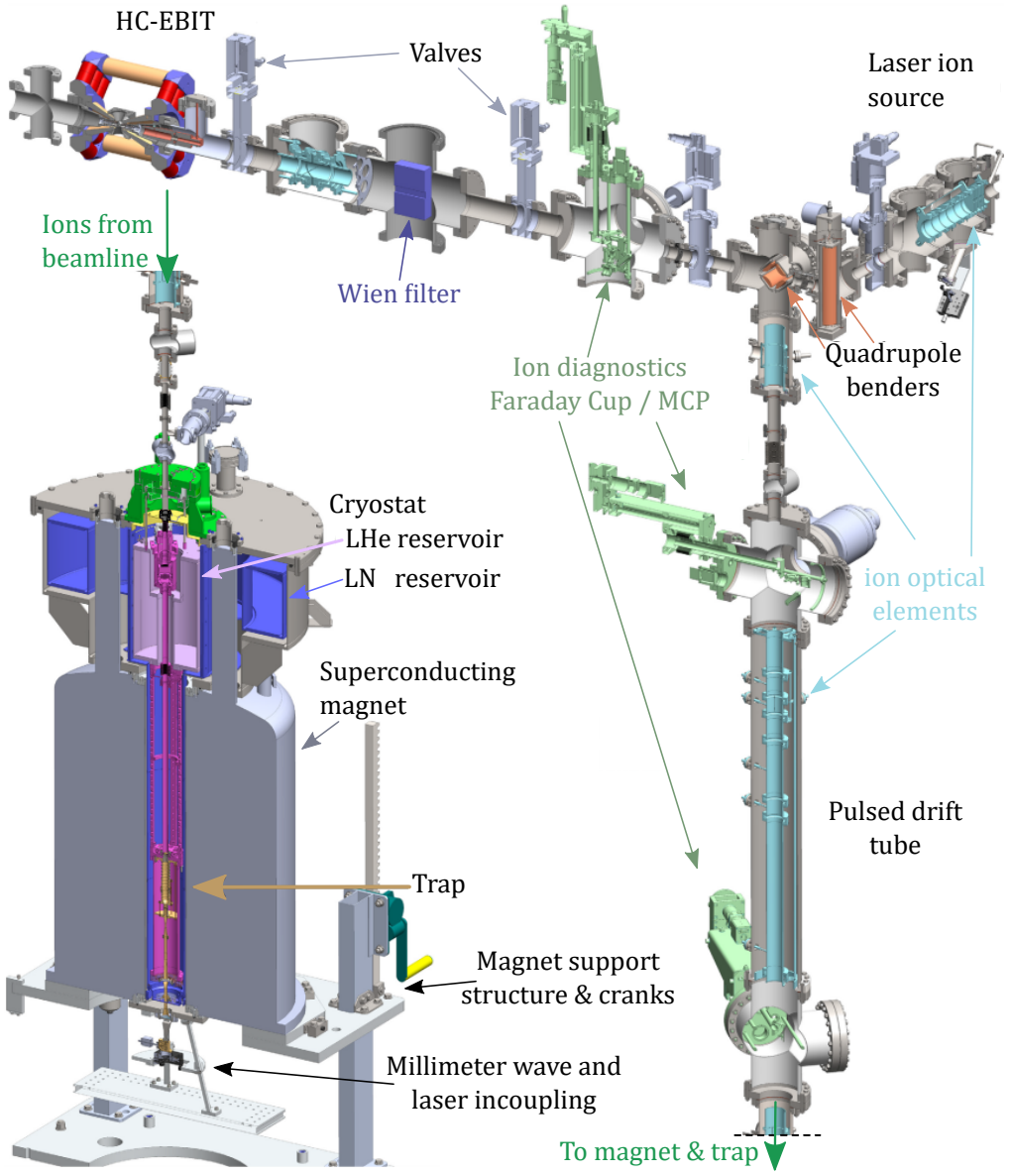

Figure 3.1.: Overview of the ALPHATRAP experimental setup. **bottom left** Lower end of the beamline located in the basement. The Penning-trap system is surrounded by the cryostat structure and inserted into the superconducting magnet. A cryogenic valve is used to partition off the cryogenic trapping region from the room temperature beamline. **top right** Upper part of the beamline located on the ground floor level. Ions can be produced in the HC-EBIT, the laser ion source or the Heidelberg-EBIT (not shown) which are connected to the beamline. For detailed description of the individual components, see text. Figure modified from [9].

pinched-off connection [157] or a foil separating the cryogenic vacuum from the beamline vacuum [174]. In order to inhibit a flow of residual gas from the beamline into the cryogenic trap region, a valve that can be operated at cryogenic temperatures and in a strong magnetic field was developed [171]. It can be opened for the injection of ions and closed during the time ions are stored, which reduces the influx of residual gas by two orders of magnitude and prevents a direct influx by blocking the line of sight. Opening or closing the valve by a mechanical detachable coupling mechanism from the outside takes around 1 min. For a detailed technical description of the beamline see [9, 84, 164, 165, 173] and for the cyrovalve and its mechanism see [84, 171].

3.3. Magnet and Cryostat

The homogeneous magnetic field necessary for the Penning trap is provided by a superconducting magnet. ALPHATRAP reuses a magnet with a vertical warm bore[1] (Oxford Instruments, 200/130 NMR [85]) which was previously used at the SMILETRAP experiment [175]. The magnet was charged to approx. 4.02 T, which leads to a convenient Larmor frequency ν_L, eq. (2.45), of around 112 GHz for hydrogenlike and 37 GHz for boronlike ions. The intrinsic self shielding factor of the magnet against external magnetic field perturbations was measured to be 14.3 [9]. The shielding is further improved by another factor of 6.7 after the installation of a superconducting self-shielding coil [9] around the trap chamber, following the proposal in [176]. The temporal stability of the magnetic field at the position of the ion was determined by continuous measurements of the free cyclotron frequency ν_c. From the modified Allan deviation a stability better than 3 ppb on a timescale from 3 min to 3 h was deduced [9, 40]. One advantage of the warm bore is that the trap chamber and beamline is inserted at room temperature and is cooled down slowly afterwards. This way the thermal stress in mechanical components, e.g. vacuum seals, electronic feedthroughs and optical windows, is drastically reduced. The superconducting tank circuits used as resonators (sec. 2.3) are also inserted into the high magnetic field above their critical temperature and therefore no repulsion of the magnetic field occurs.

However, this implies that for cooling down the experiment a dedicated independent cryostat structure is required. Inside the cryostat an insulation vacuum sets the heat transfer by convection to virtually zero, so that the only way of heat transfer is by thermal conduction and by radiation. The cryostat uses two reservoirs with a capacity of 55 l for liquid nitrogen (LN_2) and 14 l for liquid helium (LHe), to which different parts of the cryostat are thermally anchored. A cylindrical cooper tube, attached and strongly thermally coupled to the LN_2 reservoir resting in a vessel on top of the magnet, is inserted into the room temperature magnet bore (fig. 3.1). The tube is wrapped with multi-layer insulation foil and acts as a radiation shield against the heat radiation from the room temperature environment. An elaborate radial fixation at the bottom of the magnet bore prevents a thermal contact between the LN_2 shield (or "77 K"-stage) and

[1] Meaning that the bore of the magnet is not filled with liquid helium and at room temperature and atmospheric pressure, typical for nuclear magnetic resonance (NMR) magnets.

the magnet bore. The trap chamber, made from oxygen-free high-conductivity (OFHC) copper, containing the Penning-trap setup and the lower end of the beamline with the cryogenic valve are connected to the LHe reservoir, forming the LHe (or "4 K"-stage). This stage is suspended from only three pen sized durable high-performance polyimide-based rods [177] (Vespel® SP-1) into the LN_2 stage. These rods combine a low thermal heat conductivity with a large resistance to mechanical tensile forces.

The 4 K-stage can be lifted by the crane of the experimental hall and a traverse whose cables are guided through two holes in the ceiling. Then the magnet with the LN_2 cryostat is lowered and pushed to the side on a rail system. For this purpose the magnet rests on a platform which can be raised or lowered by cranks (fig. 3.1). This gives access to the complete 4 K-stage and if required, it allows fast maintenance cycles on the trap setup without venting substantial parts of the UHV beamline. Further details on the design of the cryostat and beamline can be found in [9, 84].

3.4. Penning-Trap System

The Penning-trap system of ALPHATRAP is optimized towards measurements on HCIs, like their ground-state g-factor. As mentioned in sec. 2.5.1, it makes use of the double-trap technique. Therefore the Penning-trap tower has an analysis trap (AT) and a precision trap (PT). Furthermore, for catching externally injected ions also a dedicated capture trap (CT) is formed by the first stack of electrodes in the trap tower. During the design and construction phase the idea to work towards sympathetic laser cooling with $^9Be^+$ ions arose. However, there was not a dedicated trap optimized for this purpose in the initial blueprint. Nevertheless, a rudimentary trap can be created by using some electrodes below the AT, and is therefore consequently called the beryllium trap (BeT), see sec. 4.2.

The whole stack of electrodes forming the individual traps, as well as the electrodes for an ion transport between them, is held together by a mechanical mounting structure and is enhoused by a cylindrical OFHC copper chamber (fig. 3.2). The trap electrodes are machined with 10 µm tolerance from OFHC copper, which is chosen because of its low susceptibility due to a reduced contamination with paramagnetic oxygen. In order to inhibit oxidation and to reduce the effect of patch potentials, all electrodes are coated with 10 µm layer of gold and 1 µm layer of silver as diffusion barrier in between. As insulating spacers between the electrodes, quartz-glass (SiO_2) and sapphire (Al_2O_3) are used. Fig. 3.2 shows the schematic view of the complete Penning-trap system. Following the convention in [9, 40] for a cylindrical Penning trap, the characteristic trap length d can be given as $d = \sqrt{\frac{1}{2}\left(z_0^2 + \frac{\rho_0^2}{2}\right)}$, where ρ_0 is the inner radius. z_0 is the axial distance from the ring electrode center to the edge of the endcap electrode $z_0 = l_r/2 + l_g + l_{c1} + l_g + l_{c2} + l_g$, including the gaps l_g between the electrodes, see fig. 3.2.

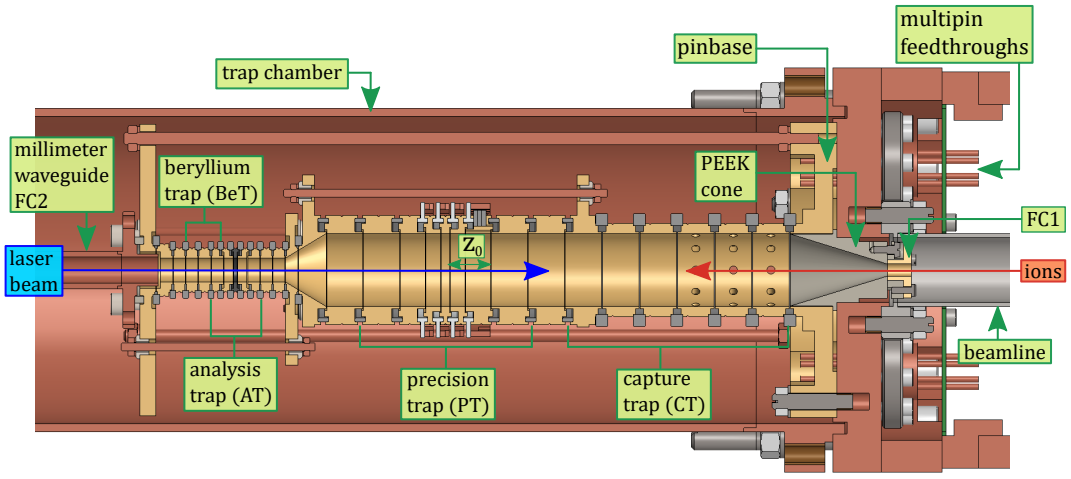

Figure 3.2.: Drawing of the ALPHATRAP Penning-trap setup. The trap tower is mounted onto the pinbase inside the trap chamber made from OFHC copper. The ions can be injected through a small aperture that also serves as a Faraday cup (FC1). As second Faraday cup (FC2) the millimeter waveguide at the bottom end can be used. The capture trap (CT) allows to dynamically capture externally injected ions and also store them for an extended period of time. Electrode voltages, as well as signal and excitation lines are led out of the trap chamber via multipin feedthroughs. Laser beams for spectroscopy or laser cooling can be injected from the lower end and are spatially overlapped with the millimeter waves. For details see text.

Capture Trap

The capture trap is located below a cone consisting of polyether ether ketone (PEEK) enriched with carbon nano tubes [178] (TECAPEEK ELS nano black®). The material of this cone is conductive and serves as a dump for the injected millimeter wave radiation. Before entering the trap, a bunch of ions is decelerated to a residual kinetic energy of around $q \cdot 150\,\mathrm{V}$. In order to capture the bunch, a fast-switchable and similar high potential is required. In the CT the insulation distances between electrodes are enlarged, allowing to safely apply higher voltages than in the rest of the trap. When the bunch enters the CT, the potential on the first electrodes is low, whereas the potential at the last electrodes is higher than the kinetic energy of the ions. Ideally close to the turnaround point at which the ions would reverse to leave again the trap, the first electrodes are switched to a high potential. In this way the ions are caught in a potential well, which has to be deeper than the energy spread of the incoming ions. The time when ions are entering or leaving the Penning-trap tower can be measured. For this purpose two cryogenic charge sensitive detectors [84] are connected each to an aperture with 3 mm

diameter opening at the top of the PEEK cone and to a millimeter wave guide at the bottom of the trap, see fig. 3.2. These two conductors act as Faraday Cups for the incoming ion bunch. For the fast switching, the first three electrodes have fast diode pair filters which allow switching times of 1 µs [84]. Once captured, the ions can also be long term stored in this potential well.

Small fractions of ions can be reloaded multiple times from this reservoir into the traps below, which reduces the dependency on the availability of the external ion sources, e.g. the Heidelberg-EBIT. Storage times longer than four months have been achieved for $^{40}Ar^{13+}$. In addition, the potentials for the long-term storage can also be generated by a battery, which makes the storage insensitive to very rare power outages.

Precision Trap

The precision trap is a 7-electrode trap based on a design [25] for the light ion trap (LIONTRAP) experiment in Mainz [179, 180]. However, the geometry was upscaled to be optimized for experiments with heavy HCI [40]. A detailed discussion on the design and optimisation process can be found in [25, 40]. The trap is dynamically orthogonal and compensated, which can be achieved to an exceptionally high degree by using a 7-electrode configuration, see sec. 2.2.1. The increased harmonicity is of advantage when using phase sensitive measurement methods, such as PnA [70], in which the ion is excited to large motional amplitudes. The signal-to-noise ratio in PnA can be increased when going to larger amplitudes, which is possible in such a highly harmonic trap. At the same time the uncertainty in the detected phase is decreasing [83]. As a further mechanical feature of the PT, the insulator rings and grooves of the electrode have a unique matching, because the total thermal linear expansion[2] of OFCH cooper and quartz glass differs significantly. The electrodes are encompassing the insulator rings so that, when cooling down the electrodes shrink more than the insulators rings and contract onto the outer lateral surface of the rings which likely improves the concentricity of the electrodes. This is very important since the inner radius of 9 mm is larger than for other experiments, e.g. 3.5 mm in the Mainz g-factor experiment [181]. Therefore a misalignment induced by thermal contraction during a cool down would be sizeable [84]. The radius is increased in order to reduce the influence of the image charge shift, which scales e.g. for the free cyclotron frequency $\frac{\Delta\nu_c}{\nu_c} \propto \frac{m}{r^3}$ [101] and which dominated systematics and their uncertainties in previous g-factor experiments [83, 182]. The image charge shift becomes even more relevant for heavier HCIs and, as a result, the larger radius of the PT mitigates this effect. For the application of di- and quadrupolar pulses (sec. 2.4) and for radial detection (sec. 2.3) the ring and the inner correction electrodes are radially halved and the outer upper correction electrode is quartered-segmented, see fig. 2.2.

[2] The often used temperature coefficient of thermal expansion $\alpha(T) = \frac{1}{L}\frac{\mathrm{d}L}{\mathrm{d}T}$ is temperature dependent. For cooling down to a temperature range where the assumed linearity ($\frac{\Delta L}{L} = \alpha\Delta T$) is not given anymore, the total (integrated) thermal linear expansion from 293 K to a temperature T, $\frac{\Delta L}{L} = \int_T^{293\,\mathrm{K}} \alpha(T)\mathrm{d}T = \frac{L_{293}-L_T}{L_{293}}$, is a more useful quantity [103].

Analysis Trap

The strong magnetic bottle required for the application of the CSGE (sec. 2.5) is created in the analysis trap. In order to be able to resolve and unambiguously detect a spin state transition in HCIs, eq. (2.48), the B_2 must be as high as possible. For the implementation of this magnetic inhomogeneity the ring electrode of the AT is replaced by a ferromagnetic cobalt iron alloy [183] (VACOFLUX®50) with a high magnetic permeability (fig. 2.6). The strength of B_2 at the trap center ($\rho = z = 0$) depends on the saturation magnetization M_0, which is around 2.35 T for the used CoFe alloy and the radius r of the electrode, which is 3 mm, $B_2 \propto \frac{M_0}{r^3}$. The achieved B_2 value is about 44 kT/m^2. For the induction of spin state transitions in the ground state of boronlike HCI ($^2P_{1/2}$ states), the Larmor frequency ν_L is around 37 GHz and a propagation of millimeter waves with this frequency through the AT has to be ensured. Therefore the cut off frequency for the millimeter wave transmission through the AT sets a lower limit to the trap radius. In contrast to the PT, where the main focus is on the precise determination of absolute frequencies, in the AT the detection of relative frequency differences after spin state transitions is of uttermost importance. Therefore, if the trapping frequencies are sufficiently stable [40, 84], systematic shifts are not as severe as in the AT. This being the case, the whole AT is built as 5-electrode trap with only one pair of correction electrodes with lower level of complexity so that fewer highly-stable voltage channels are required. The electrodes are manufactured in the same way as the PT electrodes, but additionally their inner surfaces were plasma polished to reduce the effect of patch potentials which are more pronounced for a smaller trap diameter. The insulating spacer rings are made from sapphire and are not T-shaped but rather have the conventional rectangular cross section. Even though the trap centers of AT and PT are spatially separated by 52 mm, the main contribution to the B_2^{PT} is coming from the ferromagnetic ring of the AT. This tail of the magnetic bottle (fig. 2.6), extending into the PT, is counteracted by a ring of the same CoFe alloy mounted retrospectively around the Penning trap tower which reduces the B_2^{PT} by one order of magnitude [9, 40].

3.5. Laser and Millimeter Wave Systems

Alphatrap has the possibility to irradiate the ion in the trap with electromagnetic radiation of different frequencies. For the first time and without experience different laser systems were added to the experimental setup. The frequencies used up to now are in the millimeter wave and optical regime. The Larmor frequency ν_L for driving spin state transitions between Zeeman substates of the ground states is around 37 GHz for boronlike HCI and 112 GHz for hydrogen- and lithiumlike HCI. The laser radiation for the laser cooling of $^9\mathrm{Be}^+$ is produced by a turnkey laser system, permanently available and located in an adjacent laser laboratory next to the magnet room. For the spectroscopy of HCI, the laser laboratory offers space to temporarily install other laser systems, as it was done for the fine structure spectroscopy of $^{40}\mathrm{Ar}^{13+}$. These systems and the way they are brought into the trap are shortly presented in the following section.

3.5.1. $^9Be^+$ Cooling Laser

The transition used for laser cooling of $^9Be^+$ has a wavelength in the UV-range of 313 nm. For the production of this laser radiation a commercial laser system is used [184] (TA-FHG pro). It uses nonlinear optical elements for a two stage frequency quadrupling, see fig. 3.3. An external cavity diode laser (ECDL) in Littrow configuration emits in single frequency mode operation at the fundamental wavelength of 1252 nm with a typical power of around 80 mW, which is first amplified by a tapered amplifier (TA) to around 1800 mW. This radiation is then frequency doubled by a second harmonic generation (SHG) unit and subsequently in a fourth harmonic generation (FHG) unit, resulting in up to 300 mW at 313 nm. Both SHG units are identical in design and geometry. For a resonant enhancement of the fundamental laser power, the doubling stages are bow tie type cavities into which a temperature stabilized non-linear optic (NLO) crystal is mounted. Crucial for the higher harmonic generation process is a good phase-matching between the fundamental and frequency doubled beam and a reliable robust lock of the cavity. A proper phase-matching is ensured by dedicated mode matching optics, control of the laser beam polarization, the temperature stabilization of the NLO crystal and a mechanical adjustment of the crystal angle and the light propagation [185]. The cavity length is stabilized via a piezo actuator on which one cavity mirror is mounted and the Pound-Drever-Hall scheme [186] is employed.

In a self-heterodyne measurement performed by the manufacturer, the linewidth at 313 nm on 3 µs integration time was determined to be around 30 kHz. At an integration time scale of 100 ms, the linewidth of the laser system at 313 nm was estimated to be around 190 kHz [69]. This was measured in a heterodyne measurement with another TA-FHG pro system used [146] at the proton g-factor experiment in Mainz.

For the stabilization of the laser frequency, a feedback loop using a wavelength meter is used. A small fraction of the power at 626 nm is coupled out by one mirror after the SHG into a optical single mode (SM) glass fiber, which is connected to the wavelength meter [187] (Ångstrom WS Ultimate 2), see fig. 3.3. Using a proportional–integral–derivative controller the wavelength meter creates an error signal that is fed back to the piezo control of the grating in the ECDL. The measurement resolution of the wavelength meter is 200 kHz at an absolute accuracy that depends on the absolute frequency difference, $\Delta\nu_{cal} = |\nu - \nu_{\mathrm{cal}}|$, of the measured frequency ν and the calibration point ν_{cal}. The absolute accuracy is specified to be ± 2 MHz for $\Delta\nu_{cal} < 10$ nm (respectively ± 10 MHz for $10\,\mathrm{nm} < \Delta\nu_{cal} < 200\,\mathrm{nm}$ and ± 30 MHz for $\Delta\nu_{cal} > 200$ nm).

A Helium-Neon (HeNe) laser [188] (LJSC-3-11) is used as an absolute reference for the calibration of the wavelength meter. The HeNe can be locked to one transition in iodine vapour at around 633 nm with a specified absolute frequency uncertainty of 2.5×10^{-11} equal to 12 kHz. The Allan variation for frequency stability is specified to be 1×10^{-11} at an averaging time of 1 s respectively 3×10^{-12} at an averaging time of 10 s [188].

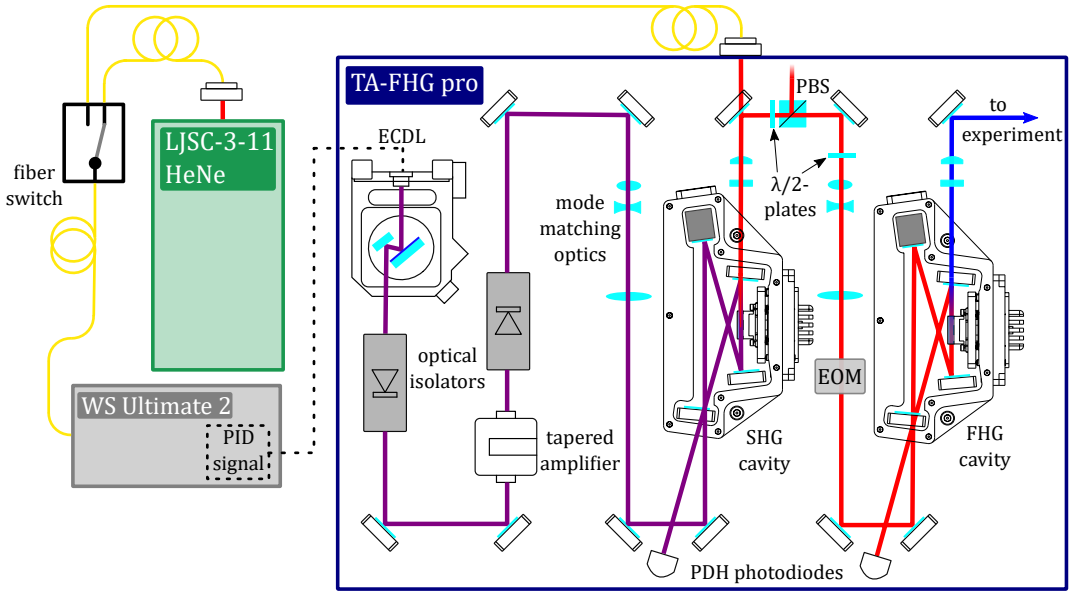

Figure 3.3.: Schematic of the beryllium cooling laser. Light from an external cavity laser diode (ECDL) is two times frequency doubled in a second and fourth harmonic generation (SHG/FHG) cavity using non-linear optic crystals. The cavities are stabilized using the Pound-Drever-Hall (PDH) locking scheme. For the PDH lock to work, the fundamental mode is modulated by the diode for the SHG and by an electro-optic modulator (EOM) for the FHG. The frequency can be controlled and stabilized by guiding some light after the SHG into a wavemeter, which is regularly calibrated by an iodine stabilized HeNe laser. Figure adapted from [185].

3.5.2. $^{40}Ar^{13+}$ Spectroscopy Laser System

The fine structure transition between the $2p\ ^2P_{1/2}$ and $^2P_{3/2}$ manifolds in boronlike argon amounts to roughly 441 nm. This wavelength is produced by using the frequency doubled fluorescence light of a titanium-doped sapphire (Ti:sapphire) laser, see fig. 3.4. The Ti:sapphire crystal is mounted in a ring laser [189] (Matisse 2 TS), which is pumped by a diode-pumped solid-state laser [190] (Verdi V18) with a typical power of 15 W at 532 nm. Using birefringent filters and etalons, one spectral single mode of the broad fluorescence spectrum of the Ti:sapphire crystal is selected, which yields 1.5 W to 2 W at 882 nm, which is subsequently frequency doubled by second harmonic generation. The frequency doubling based on a NLO crystal is done in a stand-alone external cavity [191] (Wavetrain 2) yielding up to 200 mW at 441 nm. In order to guide this light towards the Penning-trap system, a SM glass fiber was used, which goes from the laser laboratory into the magnet room and is outcoupled on a optical breadboard mounted below the

magnet (sec. 3.5.3). The output frequency of the system can be stabilized in two ways. The Ti:sapphire laser can be locked to a stable reference cell, that employs a side-of-fringe stabilization, yielding a spectral line width of typically[3] $< 50\,\mathrm{kHz_{rms}}/100\,\mathrm{ms}$ [189]. The long term stability is ensured by using the same wavelength meter as described in sec. 3.5.1. A fraction of the light of the Ti:sapphire at 882 nm is coupled into an optical single mode glass fiber and connected to the wavelength meter, which is regularly calibrated by the same HeNe laser as described in the previous section 3.5.1.

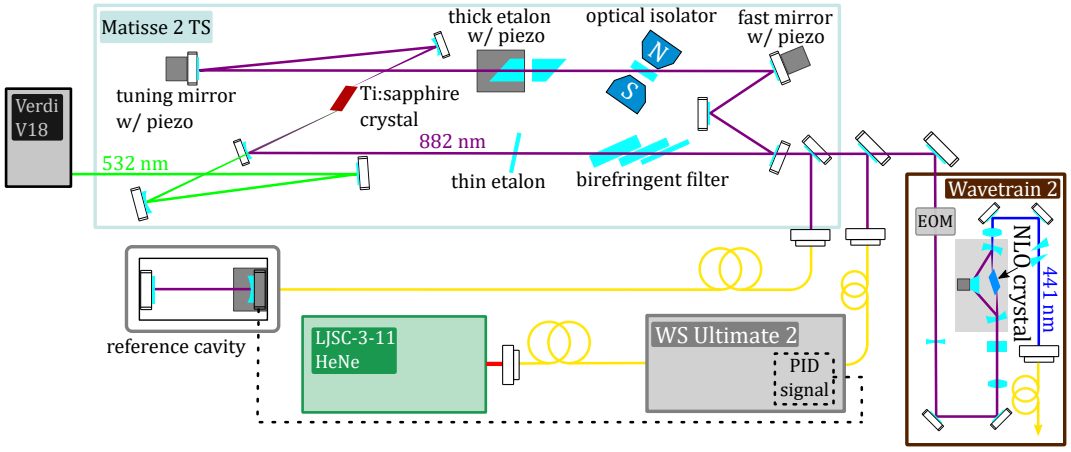

Figure 3.4.: Schematic of the laser system for the fine structure spectroscopy of $^{40}Ar^{13+}$. A ring laser with a Ti:sapphire crystal is pumped by a solid state laser. From the broad Ti:sapphire emission spectrum, a single wavelength mode is selected by etalons and a birefringent filter. The ring laser is locked to an external fiber coupled reference cavity. Long term frequency stabilization and control is achieved by using a wavelength meter which generates a voltage signal to change the piezo controlled cavity length. The wavelength meter is calibrated by an iodine stabilized HeNe laser serving as frequency standard. The laser light is frequency doubled after the ring laser in a standalone external cavity using a non-linear optic crystal. From there the laser light is guided to the trap setup using a single mode optical glass fiber. Figures adapted from [189, 191].

3.5.3. Millimeter Wave System and Laser Incoupling

Frequencies up to 40 GHz can be directly obtained by a millimeter wave signal generator [192] (MG3694C) or converted with an active frequency multiplier (sixfold frequency multiplication) to 112 GHz. Millimeter waves up to 40 GHz, as used throughout the presented measurements (chap. 5), are produced by the signal generator. They are

[3] This applies to the light with wavelength of 882 nm which is generated by the Ti:sapphire laser. This value would have to be doubled for 441 nm.

brought towards the trap setup with a semirigid coaxial cable connected to a coax-to-waveguide adapter which inserts them into a rectangular WR28 (internal dimensions 7.1 mm × 3.6 mm) waveguide. From their place of production, next to the magnet at room temperature and atmospheric pressure, the millimeter waves have to travel through two separate vacuum compartments (the insulation vacuum of the cryostat and the cryogenic vacuum inside the trap chamber) and two stages of the cryostat at different temperatures (the heat shield of the LN_2 and LHe cryostats), see sec. 3.3. In order to reduce the heat load on the cryostat, the transitions between different temperature and vacuum stages are bridged with horn-to-horn transitions, see fig. 3.5. This allows to transmit the millimeter waves between adjoining waveguide segments without a thermal connection between the heat shields and thus no thermal heat conduction.

In addition to the millimeter waves also the laser light has to be brought into the trap chamber. The laser laboratory was built behind the magnet room because the laser systems and optical components have stricter requirements on the cleanliness of the environment[4]. The laser light sources are in this adjacent room and a small opening in the wall allows to bring laser radiation onto an optical breadboard mounted below the magnet either as a free beam or by an optical fiber. Onto this optical breadboard, additional optics are mounted into a rigid optical cage system that allows for beam alignment and shaping. In order to pass through the apertures in the propagation path towards the trap, typically the laser beam diameter is reduced by an inverted Keplerian type beam expander. Furthermore the beam paths of laser beams with different wavelenghts can be combined by using a dichroic mirror, so that there is the possibility to use multiple frequencies of laser light in the same experiment. Nevertheless, for a free beam propagation the long distance between laser head and trap leads to sizable changes of the beam pointing, which in the case for the laser cooling measurements (chap. 4) already shows a substantial effect. Therefore the implementation of a laser beam alignment and stabilization system is work in progress within the master's thesis of Felix Hahne [193].

The only line of sight onto the trap center is along the axial trap axis. The cross section of the waveguides is large enough to allow transmission of a laser beam, but for merging the light with the millimeter waves special care has to be taken. In case of the 37 GHz the large size of the WR28 waveguides allows to drill a hole of 2 mm diameter tangentially into a 90° bend. This hole is smaller than the narrowest width of the waveguide and the wavelength in air, which is around 8 mm and thus constitutes only a small distortion for the millimeter waves. Therefore the propagation along the section with the drilled hole takes place without significant loss of power or reflections. When going from 37 GHz to 112 GHz, this ratio of waveguide dimension and wavelength is adverse for the same size of hole diameter. That is why a special waveguide was designed, following the same principle, however the geometry and hole diameter are optimized towards high transmission and reasonably sized aperture for the laser. Details of this waveguide and the overall millimeter waveguide setup can be found in [9, 194]. Since the microwave and the laser beam share the same path of propagation towards the trap, viewports with

[4]The magnet room of the ALPHATRAP setup is located in the basement of the accelerator hall which contains most of the building infrastructure and has a very high level of particulates in the air.

high transmission for the used frequencies have to be between the millimeter wave horns facing each other. This is fulfilled for UV fused silica, which is used as windows. At the transition from atmospheric pressure to the cryostat insulation vacuum a commercially available high-vacuum ConFlat flange viewports was used. At the bottom of the trap chamber a custom made flange was designed and machined into to bottom flange of the trap chamber. Because this part of the experiment cools down to approx. 4 K, a indium seal was used for the interface of silica windows and the OFHC copper of the trap chamber. Both windows [195] (VPWW42-UV) have a 30′ wedge on the side facing the incoming laser beam and an anti-reflection coating in order to minimize reflections or etalon like effects.

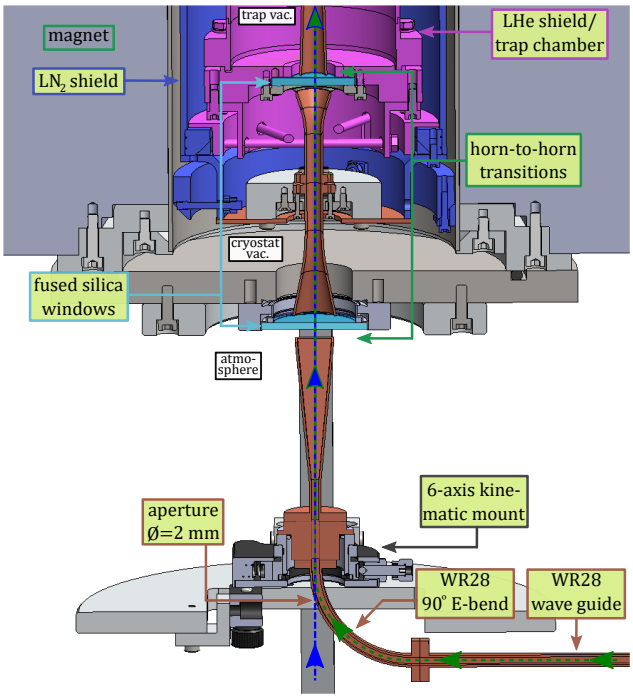

Figure 3.5.: Setup of the millimeter wave and laser incoupling. Shown is a cross section of the lower end of the magnet bore and cryostat. For the 37 GHz WR28 wave guides are used. The propagation path of the millimeter waves and laser beam are merged in a 90° E-bend of the waveguide, where the laser beam can enter tangentially into the waveguide through a 2 mm aperture. The cryostat is color coded to highlight the different temperature stages of the LN_2 stage (pink, ≈77 K) and the LHe cooled stage (blue, ≈4 K). The white labels show the compartments at different pressures which are separated by wedged fused silica windows and bridged by the millimeter waveguides using horn-to-horn transitions.

4. Experimental Results: Laser Cooling of $^9Be^+$ - Towards Sympathetic Laser Cooling of HCI

In this chapter the results from a measurement campaign on laser cooling of $^9Be^+$ ions will be presented. The main objective of these measurements is to demonstrate and verify that the $^9Be^+$ can be laser cooled at ALPHATRAP, in order to develop a specific strategy towards the implementation of a sympathetic laser cooling scheme. For this campaign three important steps were accomplished, the integration of the laser system (sec. 3.5.1, sec. 3.5.3) and a dedicated trap for beryllium (BeT, sec. 4.2) into the existing setup, the successful injection of beryllium ions into the trap and the demonstration of an interaction between these ions and the laser light. The interaction that leads to cooling of particles was shown qualitatively on a cloud of $^9Be^+$ ions stored in the AT, but could also be verified by measurements of the axial temperature of a single $^9Be^+$ ion stored in the BeT (sec. 4.4). These achievements are the first steps needed to be taken towards sympathetic cooling of HCIs and some valuable experience for future laser cooling experiments were gained.

4.1. Relevant Energy Levels of Singly Ionized Beryllium $^9Be^+$

As previously mentioned, HCIs generally do not offer laser accessible fast dipole allowed cooling transitions, therefore cooling is done via an auxiliary beryllium ion. To better understand the used laser cooling transition, this section will provide a close look at the atomic structure of singly charged beryllium in an external magnetic field.

Beryllium is an alkaline earth metal and as singly charged ion it has an alkali-like electron configuration ($1s^2 2s^1$) with one outer electron in the outermost shell, which simplifies the level scheme. Therefore the ground state is the $2\,^2S_{1/2}$ configuration and the next highest excited states are the two $^2P_{1/2}$ and $^2P_{3/2}$ fine structure states. Transitions between the ground state and excited states are dipole (E1) allowed. The nucleus of ^{9}Be carries a nuclear spin $I = 3/2$, which gives rise to an additional hyperfine structure. This leads to a coupling $\vec{F} = \vec{J} + \vec{I}$ between the total angular momentum of the electron $\vec{J}$ and the nucleus $\vec{I}$. The resulting HFS levels can be described by the quantum number F which takes the values $F = J+I, J+I, \ldots, |J-I|$ and each state is $2F+1$-times degenerate.

In the case of a weak external magnetic field this degeneracy is lifted and each HFS state splits into m_F states due to the Zeeman effect. A weak field here refers to the magnetic field strength at which the magnetic potential energy of the ion $\Phi_{\mathrm{HFS}} = -\vec{\mu}_F \vec{B}$

is much smaller than the energy difference of the hyperfine states $\Delta E_{\mathrm{HFS}} = g_F \mu_B B m_F$ and the coupling $\vec{F} = \vec{J} + \vec{I}$ keeps valid [54]. Here, $\vec{\mu}_F = \vec{\mu}_I + \vec{\mu}_J$ denotes the total internal magnetic moment of the ion and g_F is calculated from I, J, F, the Landé g-factor g_J and the nuclear g-factor g_I [54]. The eigenstates $|F, m_F\rangle$ can be described in a base using the quantum numbers F and m_F.

In the case of a strong external magnetic field, such as the 4 T inside the ALPHATRAP Penning trap, the angular momenta of I and J decouple, changing the level scheme and entering the hyperfine Paschen-Back regime[1]. Therefore the quantum number F no longer describes the eigenstates correctly and useful quantum numbers for the eigenstates become $|m_I, m_J\rangle$ [54]. The levels group into $2J+1$ manifolds with $2I+1$ sublevels.

At 0 T the vacuum wavelength for the transition between from $^2S_{1/2}$ to $^2P_{1/2}$ (resp. $^2P_{3/2}$) is 313.132 92(5) nm (resp. 313.197 42(4) nm) [196] corresponding to a fine structure splitting of 197.150(64) GHz [197]. The upper state lifetime τ of the ^2P states is 8.1(4) ns [198], which corresponds to a natural linewidth $\Gamma = \frac{1}{2\pi\tau} = 19.6(10)$ MHz. The shifts of all levels for different magnetic field strengths are exemplary shown in fig. 4.1.

For laser cooling the $^2S_{1/2}\,|m_I, m_J\rangle = |-3/2, -1/2\rangle$ to $^2P_{3/2}\,|-3/2, -3/2\rangle$ [197, 199] transition as well as $^2S_{1/2}\,|+3/2, +1/2\rangle$ to $^2P_{3/2}\,|+3/2, +3/2\rangle$ [200–202] can be used, see fig. 4.1. These transitions can be driven by circular polarized laser light, σ^- for $\Delta m_J = -1$ respectively σ^+ for $\Delta m_J = +1$. Because the hyperfine interaction will cause amplitude mixing of the states with $m_I \neq -3/2$ resp. $m_I \neq +3/2$, optical pumping into the pure states with $m_I = -3/2$ resp. $m_I = +3/2$ occurs [203, 204]. For efficient laser cooling a closed cycle of transitions is required. If this closed cycle is left, the cooling will fail. A repumping into the closed cooling cycle is necessary, typically provided by addressing other transitions with additional laser frequencies. In $^9Be^+$ this can be achieved even with one single laser frequency only, using the special level structure, in which an intrinsic repumping mechanism into the initial state of the cooling cycle exists. This will be further discussed for the specific case[2] when using the σ^- transition $^2S_{1/2}\ |-3/2, -1/2\rangle \rightarrow {}^2P_{3/2}\ |-3/2, -3/2\rangle$. At 4 T the splitting between the two $^2S_{1/2}$ $|m_I, \pm 1/2\rangle$ ground states amounts to about 110 GHz, which means a depopulation from the bright $^2S_{1/2}\,|m_I, -1/2\rangle$ into the dark $^2S_{1/2}\,|m_I, +1/2\rangle$ state will cause the cooling to stop. Such a depopulation can occur because the transition $^2S_{1/2}\,|m_I, -1/2\rangle \rightarrow {}^2P_{3/2}\,|m_I, +1/2\rangle$ can be driven off-resonantly (by 150 GHz) by laser light with opposite, wrong handiness. From there, the ratio of the spontaneous decay rates into the bright and dark ground states is 1/3 to 2/3, resulting in a depopulation of the $^2S_{1/2}\,|m_I, -1/2\rangle$ level. Once the ion is in the $^2S_{1/2}\,|m_I, +1/2\rangle$ state it can be off-resonantly (by 73 GHz) driven to the $^2P_{3/2}\,|m_I, -1/2\rangle$ by the initial cooling laser. In contrast to the previous depopulation cycle, in this repumping cycle, the ratio of the spontaneous decay rates from the $^2P_{3/2}\,|m_I, -1/2\rangle$ into the bright and dark ground states is now conversely favoring the bright over the dark state with 2/3 to 1/3.

[1] Here it is refered to the hyperfine Paschen-Back effect because of the break up of the coupling of F and I which is analog to the Paschen-back effect of the anomalous Zeeman effect in which the LS spin-orbit coupling (cf. sec. 2.5)is broken up.

[2] Same holds true vice versa for the case of the σ^+ transition.

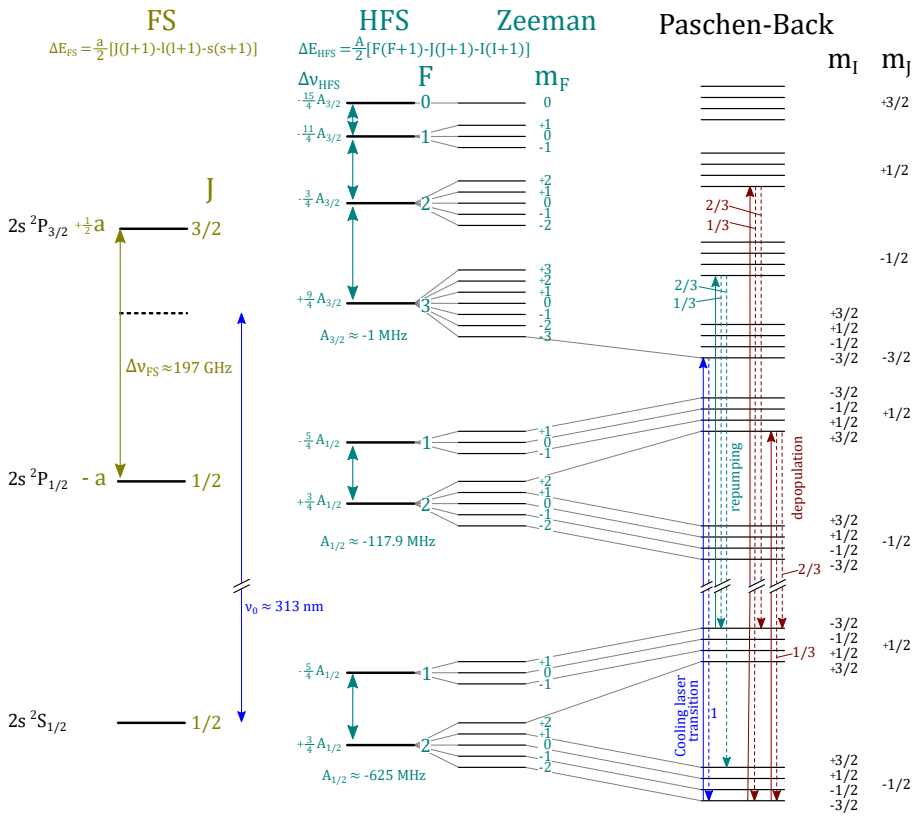

Figure 4.1.: Energy levels of the $^2S_{1/2}$ ground state and $^2P_{1/2}$ and $^2P_{3/2}$ excited states. Laser excitations are represented by a solid line and dotted lines are the spontaneous decays with corresponding probabilities next to the line. Exemplary shown is the laser cooling transition $^2S_{1/2}\,|-3/2,-1/2\rangle \rightarrow {}^2P_{3/2}\,|-3/2,-3/2\rangle$. Optical pumping occurs into the $^2S_{1/2}\,|-3/2,-1/2\rangle$ ground state and the $^2S_{1/2}\,|m_I,+1/2\rangle$ is in this case the dark state. Repumping from the dark state takes place via excitation to the $\rightarrow {}^2P_{3/2}\,|-3/2,-1/2\rangle$ and subsequent spontaneous decay. For details see text.

Using eq. (2.60) the transition rates ρ for both off-resonant cases as a function of the detuning $\delta = \nu - \nu_0$ can be given as:

$$\rho(\delta) = \Gamma \frac{S/2}{1 + S + [2\delta/\Gamma]^2}, \tag{4.1}$$

The population in the bright state can be estimated from the ratio of the detuning of the depopulation and repumping mechanism and the branching ratios of the spontaneous decay channels. Neglecting the influence of the $^2P_{1/2}$ manifold, for $S = 1$ and the above mentioned detuned frequencies it yields a ratio of 16:1 for the population probability of

bright to dark state at a repump rate of 0.69 Hz for random polarization. Due to the strong magnetic field, the Zeeman effect shifts the $^2P_{1/2}\,|m_I, +1/2\rangle$ manifold closer to the $^2P_{3/2}\,|m_I, -3/2\rangle$ levels, so that the frequency difference between the $^2P_{1/2}\,|m_I, +1/2\rangle$ and $^2P_{3/2}\,|m_I, -3/2\rangle$ is smaller than the difference between $^2P_{3/2}\,|m_I, +1/2\rangle$ and $^2P_{3/2}$ $|m_I, -3/2\rangle$. Therefore, when using the σ^- transition to the $^2P_{3/2}\,|-3/2, -3/2\rangle$ level as laser cooling transition, the aforementioned depopulation mechanism is mainly occurring via the $^2P_{1/2}$ states. Similarly also the repumping path can go via the $^2P_{1/2}$ states, although at a far lower transition rate compared to the $^2P_{3/2}$. Taking this into account the overall population probability of bright to dark state is 5:2. The efficiency of laser cooling could be improved by usage of the proper polarization of the laser light or by enhancement of the repumping at the necessary frequency with a second laser beam. The required frequency difference between cooling and repump laser would be $\approx 100\,\text{GHz}$, so that it is technically not possible to derive this frequency from the same laser cooling fundamental frequency. Therefore, a second laser system is required. Nevertheless, the intrinsic repumping mechanism on timescale of seconds allows to perform laser cooling on $^9Be^+$ ions without the need of a repumper, assuming the heating rates are smaller than the time the ion spends in the dark state.

4.2. The Beryllium Trap (BeT)

Because of its low q/m and q^2/m ratio[3] and the optimization of the ALPHATRAP Penning traps with respect to HCIs, working with $^9Be^+$ ions in the PT or AT is not trivial. For the PT the voltages are provided by the StaRep, an in-house built ultra-stable voltage source [121], which can produce a negative voltage of up to $-100\,\text{V}$. In order to be able to detect the ion on the axial resonator of the PT, it would require a voltage lower than $-200\,\text{V}$, far beyond the specifications of this or any other available voltage source of sufficient stability. In addition, for both the PT and AT, the dip width, scaling as $\propto \frac{q^2}{m d_{\text{eff}}^2}$ (eq. (2.35)), of a single beryllium ion is only 0.1 Hz. This makes the detection of the ion signal in the AT very challenging, due to the required voltage stability. Moreover the necessary high frequency resolution for the FFT analysis would cause too long data acquisition times. In a previous measurement campaign already a jitter of 55 mHz was measured for the axial frequency of an $^{40}Ar^{13+}$ ion in the AT [40].

As a provisional workaround, a trap using the remaining electrodes below the AT was created (fig. 4.2), mitigating some of the above mentioned problems. The AT is formed by the electrodes with numbers #25-29, whereas the newly created beryllium trap (BeT) uses the electrodes #28-32, see fig. 4.2. It is implemented, by using a second spare voltage source [205] (UM1-14), whose three channels are connected to form a pair of upper and lower correction electrodes (UC/LC, #29 & 31) and a ring electrode (R, #30). This trap has the advantage that its trap center, and with it the ion, is closer to the electrode to which the axial AT resonator is connected (#29). Therefore, the effective electrode distance d_{eff} (cf. sec. 2.3.1) is reduced from $d_{\text{eff}}^{\text{AT}} = 19.15\,\text{mm}$ [84] in the AT to $d_{\text{eff}}^{\text{BeT}} = 7.33\,\text{mm}$. This way, a dip width of 0.7 Hz for a single $^9Be^+$ can

[3] But among all singly charged ions used for laser cooling it has the largest q/m and q^2/m ratio.

be obtained. The downside of this arrangement is the increased distance between the BeT trap center and the vertically bisected electrode above the upper endcap of the AT (#23/24) used for the quadrupolar excitations. In the following, the characterization of

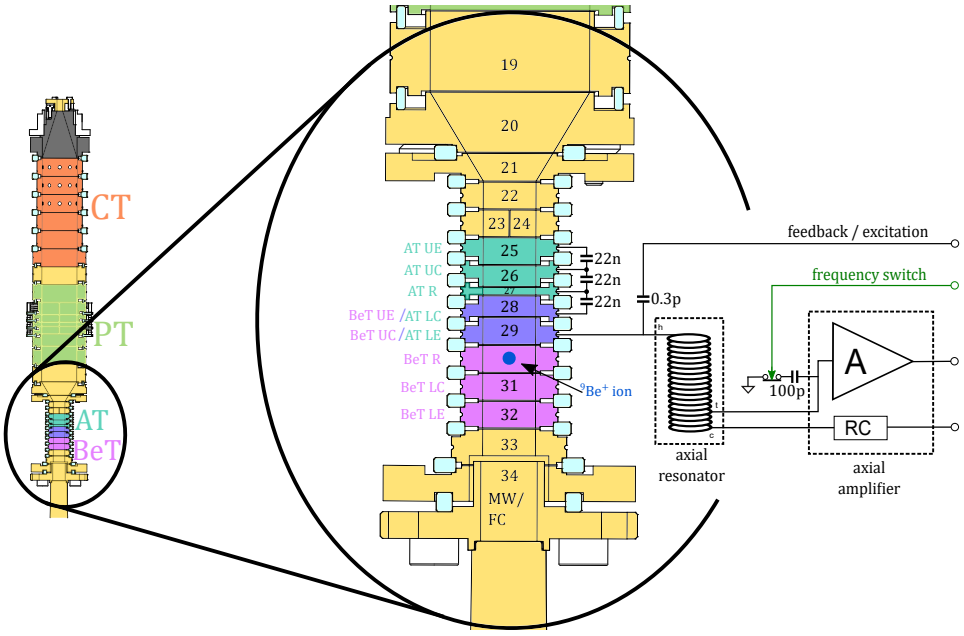

Figure 4.2.: Schematic view of the beryllium trap (BeT) at the lower end of the Penning-trap tower, located below and overlapping with the analysis trap (AT) electrodes. The AT axial resonator is connected to the upper correction electrode of the BeT. Through the same line also axial excitation and magnetron coupling pulses can be applied. For details see text.

this provisional BeT is presented as well as the first results of a successful demonstration of laser cooling with a single $^9Be^+$.

4.3. Characterization of the BeT

Because the BeT is newly created and many parameters necessary for a successful operation of this trap are not known or can only be derived approximately from simulations, a proper characterization of the BeT is crucial. Among the many, the first parameter to be checked is the correct tuning ratio, TR. Without an optimized tuning ratio experiments in this trap would not be doable. A suboptimal TR introduces systematic shifts (eq. (2.13)) of the motional frequencies or reduces the signal-to-noise ratio of the already narrow dip to such an extent that makes an ion detection rather difficult. Additional parameters are the absolute strength of the magnetic field B_0, its gradient B_1 and its curvature B_2 (eq. (2.15)). As outlined in sec. 4.1, the transition frequencies in beryllium

depend on the magnetic field strength B_0. Also the value of magnetron and cyclotron frequency are influenced by B_0, eq. (2.7). Therefore a good initial guess on the value of the magnetic field strength helps to find the laser cooling transition frequency, as well as the radial frequencies, in order to find the coupling frequencies ω_{rf}, eq. (2.42), for the quadrupole excitations. Similar to electric field imperfections, also magnetic field imperfections will lead to energy dependent frequency shifts of the ions motional frequency.

The characterization of the BeT is done with a $^{14}N^{4+}$ ion, which can be detected in the PT, AT and BeT. This allows to prepare the nitrogen ion in a well defined state, e.g. an excitation to a well-known magnetron or cyclotron radius, which is crucial for the measurements presented below.

4.3.1. Electric Field Optimization

Main goal of this procedure is to obtain an electric potential as close as possible to an ideal quadrupole potential. Potentially present field anharmonicities can be tuned out by choosing a suitable tuning ratio *TR* (sec. 2.2.1). Using the finite element analysis COMSOL Multiphysics® [206] and the dimensions of the trap electrodes, the axial potential inside the trap can be numerically evaluated. The *TR* derived from this simulation serves as a starting point for the optimization of the electric field. Due to a mishap, which has been discovered afterwards, the electrodes used as BeT for the simulation of the trapping potentials has been accidentally shifted upwards by one electrode, see fig. 4.2. Electrodes #29-32 have the same nominal lengths which should have resulted in an identical tuning ratio applied to upper and lower correction electrodes of the BeT. However, electrode #28 is shorter and as a result the derived voltages applied to the correction electrodes are not symmetric around the ring electrode anymore. Instead the $TR_{\mathrm{UC}} = 0.916\,22$ for the UC electrode, $V_{\mathrm{UC}} = V_{\mathrm{R}} \cdot TR_{\mathrm{UC}}$ and the $TR_{\mathrm{LC}} = 0.854\,62$ for the LC electrode, $V_{\mathrm{LC}} = V_{\mathrm{R}} \cdot TR_{\mathrm{LC}}$, has been used. However, this has been experimentally corrected for by introducing a combined tuning ratio TR_{c} scaling both TR_{UC} and TR_{LC}, which allows to anyway optimize for $C_4 = 0$.

In order to determine the optimal *TR*, the ion is excited to a large magnetron or cyclotron radius $\rho_{\pm}$. Due to the lack of an electrode for an efficient radial excitation in the BeT (sec. 4.3.3), the radial excitations are done in the PT and the excited ion is transported to the BeT afterwards. A possible heating of the magnetron mode during transport between PT and BeT was excluded by a separate measurement as in [84], which, as previously seen, confirmed the adiabacity of the transport. Then the axial frequency shift for different *TR*s and excitation strengths is measured and compared to the axial frequency for a thermalized cold ion with the same different *TR*s. The shift $\Delta\nu_z$ depends in the lowest two orders on C_4 and C_6 as [68]:

$$\Delta\nu_z = -\frac{C_4}{C_2}\frac{3}{2d^2}\nu_z\rho_{\pm}^2 + \frac{C_6}{C_2}\frac{45}{16d^4}\nu_z\rho_{\pm}^4. \tag{4.2}$$

The mistakenly applied *TR* is asymmetric, which introduces an additional C_3, which contributes to the axial frequency shift in second order. It acts then similar as a change

in C_4 and the shift $\Delta\nu_z$ is proportional to $\left(\frac{C_3}{C_2 d}\right)^2 \nu_z \rho_\pm^2$. For this effect has been checked using the simulation of the electrostatic trapping potentials. For an optimized TR a frequency shift due to C_3 has been found to be negligible. Also for the typically used tuning ratio changes $|\Delta TR| < 0.01$ shifts due to C_3 are more than three orders of magnitude smaller than shifts caused by C_4 and are therefore negligible, too.

For this method the excitation radius has to be known and can be determined in the PT in prior calibration measurements. Assuming that the ion is initially cooled to a radius of negligible size compared to the excited radius, the radius after excitation depends on the voltage of the excitation burst V_{exc}, the duration of the burst t_{exc} and the calibration factors $\kappa_\pm$:

$$\rho_\pm = \kappa_\pm V_{\mathrm{exc}} t_{\mathrm{exc}}. \tag{4.3}$$

In the PT, $\kappa_\pm$ are determined by doing this measurement for different combined tuning ratios TR_{comb}, a scaling factor applied to TR_1 and TR_2. For eq. (4.2), the polynomial fit parameters $P_1 = -\frac{C_4}{C_2}\frac{3}{2d^2}\kappa_\pm^2$ and $P_2 = \frac{C_6}{C_2}\frac{45}{16d^4}\kappa_\pm^4$ can be defined. Making use of the linear dependency of $P_1 \propto m_{P_1} TR_{\mathrm{comb}}$ and using eq. (4.2), the calibration constants for magnetron κ_- and cylcotron mode κ_+ for $^{14}\mathrm{N}^{4+}$ can be extracted [25, 40]:

$$\kappa_- = \sqrt{-\frac{m_{P_1} C_2}{\nu_z D_4^{\mathrm{comb}}}\frac{2d^2}{3}} = 140(1)\,\frac{\mu\mathrm{m}}{\mathrm{V\,ms}}, \tag{4.4a}$$

$$\kappa_+ = 105(2)\,\frac{\mu\mathrm{m}}{\mathrm{V\,ms}}. \tag{4.4b}$$

The value for $C_2 = -0.590\,325$ can be derived using eq. (2.3), $D_4^{\mathrm{comb}} = -0.786505$ is calculated from simulations [40] and the characteristic trap length for the PT is $d = 9.1565\,\mathrm{mm}$ [40].

The same method is applied for a tuning ratio optimization in the BeT. Compared to the procedure for the PT, the ion is transported to the BeT with already different calibrated excitation radii. There the axial frequency shift, compared to a cold ion, as function of the detuning TR_{c} and excitation strengths is measured. The scaling factor TR_{c} is applied to both TR_{UC} and TR_{LC}, such that $V_{\mathrm{LC}} = V_{\mathrm{R}} \cdot TR_{\mathrm{LC}} \cdot TR_{\mathrm{c}}$ and $V_{\mathrm{UC}} = V_{\mathrm{R}} \cdot TR_{\mathrm{UC}} \cdot TR_{\mathrm{c}}$. This way the C_4, arising from the erroneously used asymmetric TR_{UC} and TR_{LC}, as well as geometric uncertainties and patch potentials are compensated. Fig. 4.3 shows the outcome of this measurement. From a polynomial fit to the axial frequency shifts $\Delta\nu_z = \alpha_1\rho_-^2 + \alpha_2\rho_-^4$, an optimal value of $TR_{\mathrm{c}}^{\mathrm{opt}} = 0.993\,878(57)$ is determined, fig. 4.4. For TR_{UC} and TR_{LC} the previously calculated values were used. The simulated TR_{c} agrees with the herein found optimal value to 0.61 %.

Relative axial frequency shifts due to a B_2 (see sec. 4.3.2) can be estimated using eq. (2.17a). For the herein used magnetron radii $\Delta\omega_z/\omega_z$ is $< 1.4 \times 10^{-7}$ and can therefore be neglected. Even though the design of the used trap electrodes is not ab initio optimized to yield a highly harmonic trap, the contribution of the C_6 is small even for large radii as the used 300 µm.

However, during this measurement campaign the TR_{c} had to be often readjusted by an amount larger than the above given uncertainty for $TR_{\mathrm{c}}^{\mathrm{opt}}$. These adjustments are done before each measurement and are assumed to be caused by laser induced changes

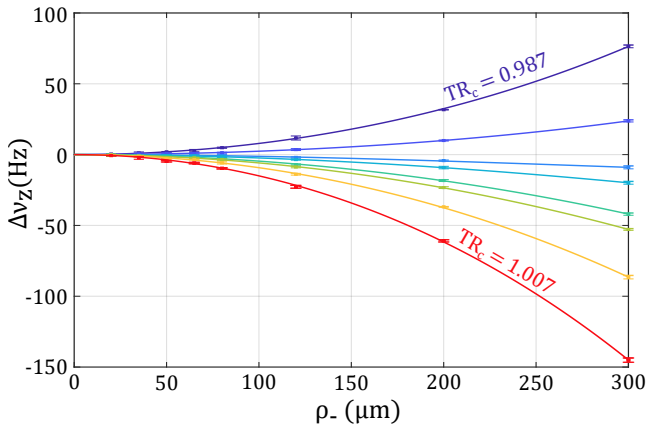

Figure 4.3.: Axial frequency shifts $\Delta\nu_z$ between an excited and thermalized $^{14}N^{4+}$ ion in the BeT as function of the excited magnetron radius and for different tuning ratios. The excitation was done after a calibration measurement in the PT and then transported to the BeT. For details see text.

of patch potentials. A similar behavior was also observed during the fine structure laser spectroscopy of $^{40}Ar^{13+}$ (chap. 5) and reported in [207–209]. Over the course of two months typical values for TR_c were 0.995(3).

4.3.2. Magnetic Field Shape

A second complication arises from the fact that for the detection of spin states a strong magnetic bottle is created by the ring electrode of the AT. Whereas the ion is typically located in the center of the magnetic bottle, where B_0 is minimal and B_2 is maximal, the center of the BeT has a nominal axial displacement of 7.45 mm with respect to center of the AT and the magnetic bottle. An initial approximate guess for the magnetic field at the position of the ion in the BeT can be obtained using the finite element analysis COMSOL Multiphysics® [206] to simulate the magnetic bottle of the AT. Fig. 4.5 shows the absolute value and the second derivative of the magnetic field in the AT and BeT on the z-axis. For this simulation the magnetic field is scaled so that the decrease of B_0 in the center of the AT matches with the measured values of B_0^{AT}. This value depends on the saturation magnetization of the ring electrode that is not given with sufficient accuracy by the manufacturer. The center of the BeT is located in one of the wings of the magnetic bottle, in a region where the B_2 has a zero crossing. The nominal trap center of the BeT is determined from the simulated potential with the aforementioned values for TR_{UC} and TR_{LC}. From the simulation a value of roughly $B_2 = 40\,\mathrm{T/m^2}$ is expected. For small deviations of the trap center, Δz, this value changes by $\Delta B_2 \simeq -0.4\frac{\mathrm{T/m^2}}{\mu\mathrm{m}}\Delta z$, see inset of fig. 4.5. The B_2 value can be measured in a similar way as described in the previous section. Instead of the magnetron mode, the cyclotron mode is excited in

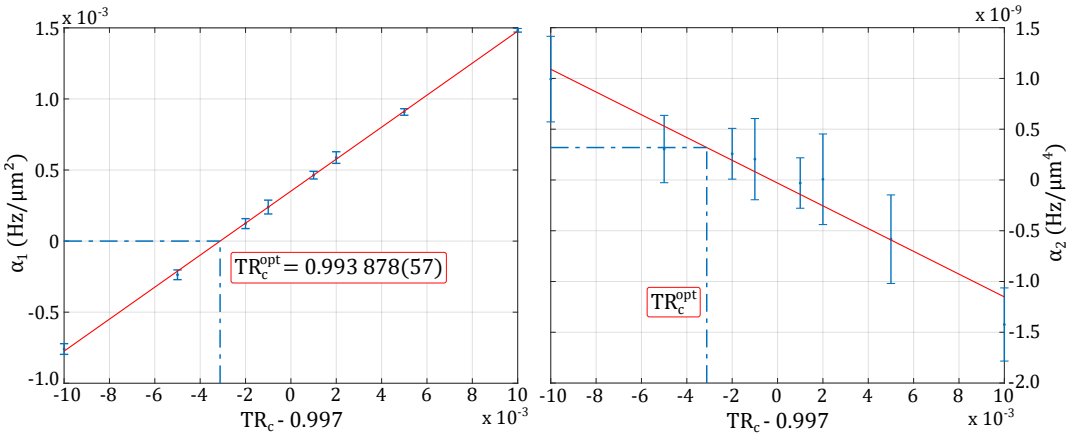

Figure 4.4.: Fit parameters of the polynomial of form $\Delta\nu_z = \alpha_1\rho_-^2 + \alpha_2\rho_-^4$. **left** Plot of the parameter $\alpha_1 \propto C_4$ as a function of the TR_c. From a linear fit to the data, the optimal value TR_c can be obtained for $\alpha_1 = 0$. **right** Plot of the parameter $\alpha_2 \propto C_6$ as a function of the TR_c. From the value of α_2 at TR_c^{opt}, which sets the shift due to C_4 to zero, the contribution due to C_6 can be estimated. For details see text.

the PT. According to eq. (2.17a) and if $C_4 = 0$, the shift for the axial frequency can be approximated as:

$$\Delta\nu_z \overset{(2.17a)}{\approx} \frac{B_2}{4B_0}\frac{(\nu_+ + \nu_-)\,\nu_z}{\nu_-}\rho_+^2 \overset{(2.8b)}{\approx} \frac{B_2}{2B_0}\frac{\nu_+^2}{\nu_z}\rho_+^2. \tag{4.5}$$

The contribution to an axial frequency shifts due to relativistic mass increase of the ion can be estimated by [80]:

$$\Delta\nu_z^{\text{rela}} \approx -\frac{1}{mc^2}\frac{\nu_z\nu_+E_+}{2\,(\nu_+ - \nu_-)} \overset{(2.11)}{=} -\frac{\pi^2}{c^2}\nu_+^2\nu_z\rho_+^2. \tag{4.6}$$

For the herein used $^{14}N^{4+}$ ion ($\nu_+^{\text{BeT}} = 7\,\text{MHz}$, $\nu_z^{\text{BeT}} = 335\,\text{kHz}$, $\nu_-^{\text{BeT}} = 31\,\text{kHz}$) excited to a cyclotron radius up to 80 µm, the absolute axial frequency shift $\Delta\nu_z^{\text{rela}} \approx 11\,\mu\text{Hz}$ is therefore negligible. The ion is excited to a specific cyclotron radius and transported to the BeT, where the axial frequency shift is measured comparing the dip frequency of the excited ion to the thermalized one. Because the cyclotron excitation was done in the PT and assuming an adiabatic transport to the BeT, the resulting cyclotron in the BeT has to be scaled by the ratio of the B_0 values for the PT and BeT:

$$\rho_+^{\text{BeT}} = \frac{B_0^{\text{PT}}}{B_0^{\text{BeT}}}\rho_+^{\text{PT}}. \tag{4.7}$$

This is because the radial motion creates a magnetic moment μ_ρ which is invariant under an adiabatic transport. The B_0^{BeT} can be estimated from the simulation model of the

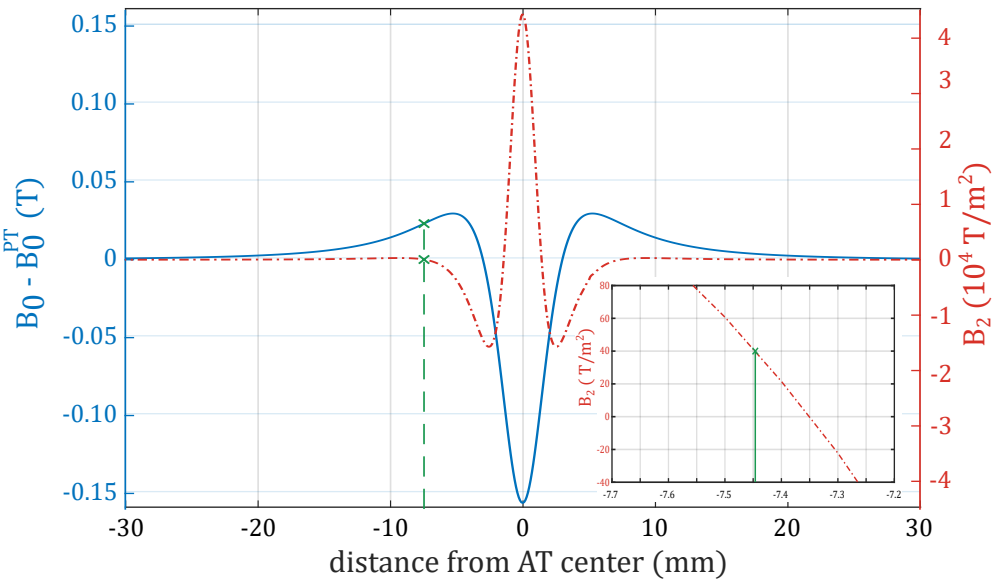

Figure 4.5.: Axial magnetic field and its second derivative in the area of AT and BeT. The blue solid line depicts the absolute magnetic field strength B_0, whereas the red dash-dot line is the second derivative B_2. The inset shows a zoom to the nominal trap center of the BeT, indicated by the green dashed line.

AT (fig. 4.5). The shift is then mainly given by eq. (4.5) and a contribution of the non vanishing C_4 in this measurement[4] can be corrected for, using the values obtained from the previous measurements, sec. 4.3.1. In fig. 4.6 the frequency shifts observed and corrected for the C_4 contribution are shown. From a fit of eq. (4.5) and taking also eq. (4.7) into account a final value of $B_2^{\mathrm{BeT}} = -28.4(27)\,\mathrm{T/m^2}$ can be derived. A jitter in the modified cyclotron radius $\delta\rho_+$ leads to a jitter in the axial frequency shift approximately linear to ρ_+ and therefore the fit is weighted by $1/\rho_+^2$ [40]. The measured value for B_2 deviates from the one derived by the simulation. Even though patch potentials can cause the real trap center to be shifted compared to the nominal center, the required voltage deviations in the order of few hundred mV seem to be very unlikely. The numerical simulation of the magnetic field is accurate on a 2 % level for B_2 in the center of the AT compared to measurements [9]. However, here the region of interest is close to a zero crossing and the B_2 is three orders of magnitude smaller than the B_2 in the AT center, so that a large uncertainty of the simulation has to be assumed in this range.

[4]The *TR* optimization, sec. 4.3.1, was done after this measurement and the herein used *TR* was taken from the initial simulations of the electrostatic potentials.

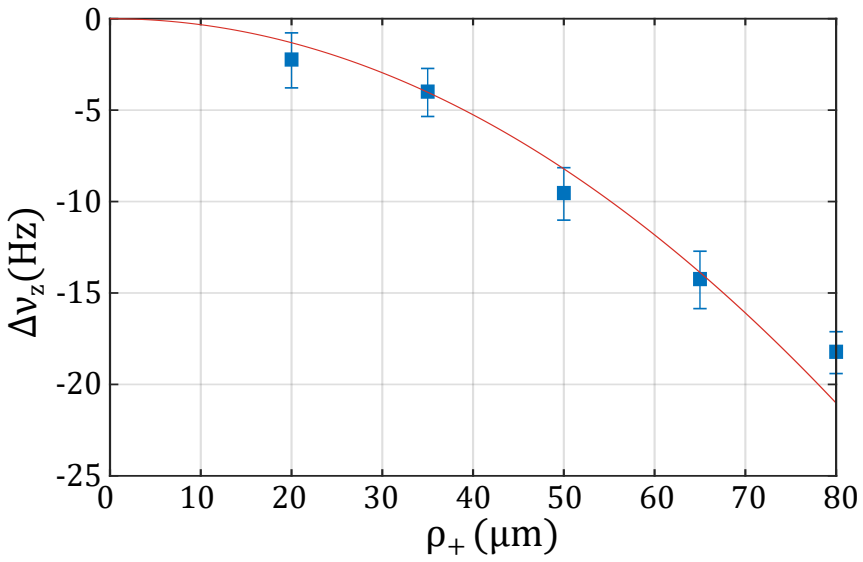

Figure 4.6.: Axial frequency shifts $\Delta\nu_z$ between an excited and thermalized $^{14}N^{4+}$ ion in the BeT as function of the excited cyclotron radius. The excitation was done after a calibration measurement in the PT and then transported to the BeT. Contributions to the frequency shift from a non vanishing C_4 are corrected for. For details see text.

4.3.3. Sideband Coupling

Laser cooling of an ion along only the axial direction leads to a heating in the radial modes (see sec. 2.7.3). In turn, cooling of the radial modes can be achieved via sideband coupling as discussed in sec. 2.4.2. Furthermore, cooling an ion in all modes to the achievable thermal equilibrium with the resonator, eq. (2.53a), allows preparing the ion in a reproducible, well defined state for further measurements. For a quadrupole excitation, split electrodes can be used and the closest segmented electrode that can be found to the BeT is the Q_{xz} electrode of the AT (#23/24 in fig. 4.2). Because of its large axial distance to the ion in the BeT, the excitation strength of this electrode at the location of the ion is not sufficiently strong to achieve sideband coupling and to observe a double dip for neither the magnetron nor the cyclotron mode. Another possibility to excite the ion is to apply the coupling radio-frequency drive to electrode #29, the UC electrode of the BeT, via the AT axial resonator (fig. 4.2). Even though this electrode is not segmented and is in principle radial symmetric, imperfections due to the manufacturing tolerances and most likely a small misalignment between the electric and magnetic field are causing the electric field produced by this electrode to have a non vanishing quadrupole component. This is sufficient to couple the axial mode with the magnetron mode, but not with the cyclotron mode. The reason for this might be that the coupling frequency for the magnetron mode, $\omega_{rf} = \omega_- + \omega_z$, is closer to the resonator

compared to the frequency required for a cylcotron coupling, $\omega_{\mathrm{rf}} = \omega_+ - \omega_z$, and the coupling is therefore enhanced by the axial resonator. Fig. 2.5 shows the magnetron double dip signal and a recorded avoided crossing obtained in this way for a single $^9Be^+$ ion the BeT.

In the future, the new dedicated laser cooling trap for beryllium which is currently under development will also allow sideband coupling between the axial and cyclotron mode. This way the temperature can be determined less complicated compared to method presented in this chapter. The temperature can be then measured as described in sec. 2.6 and performed in 5.4, using the cyclotron energy dependent axial frequency shift caused by a B_2.

4.4. Laser Cooling of a Single $^9\mathrm{Be}^+$ Ion in the BeT

Using the before introduced techniques and trap setup allows to laser cool the axial mode of a single $^9Be^+$ ion. For the verification of the laser cooling, a temperature measurement is implemented which proves that the ion's axial temperature can be brought below the temperature of resonator. The technique employed for the temperature determination and results from this are presented in the following section.

4.4.1. Ion Temperature Determination

As presented in sec. 2.3, the typical signal for the ion detection is a dip in the thermal noise spectrum of the resonator. In the derivation of this signal form it is implied, that the ion is in thermal equilibrium with the resonator. This feature is used in the there described bolometric cooling technique. However, if the ion is meant to be cooled below the temperature of the detection circuit, with which the ion is in thermal contact, then the role of the resonator changes and it is acting as a source of heating for the ion. Therefore, a technique allowing to measure the temperature should work without the ion being strongly thermally coupled to the resonator. The energy dissipation rate from the ion into the resonator is given by the frequency dependent cooling time constant $\tau(\omega)$, eq. (2.29b). This can be achieved by changing the trapping voltage so that the ions axial frequency is detuned from the resonator's frequency. For this technique the ion is off-resonant by 500 Hz to 1000 Hz, meaning that the ion's frequency lies in the noise floor of the detection circuit, far away from the flank of the resonator. In this region a thermalized ion is not visible anymore, but it can be made visible as a peak through an axial excitation.

As explained in sec. 2.6, the energy of the ion with finite temperature in thermal equilibrium with the resonator follows a Boltzmann distribution. This translates also to a distribution of radii via eq. (2.52), which is depicted as a constant and temperature dependent radial spread in phase-space, see fig. 4.7. The width of this "cloud" in the phase space can be mapped onto the axial frequency by introducing deterministically an inhomogeneity ($C_4 \neq 0$) in the trapping potential, by changing the tuning ratio. This will lead to a shift of the axial frequency $\Delta\nu_z$, eq. (2.13a). Also the peak averaged over many single measurements is smeared out by the thermal distribution of the axial

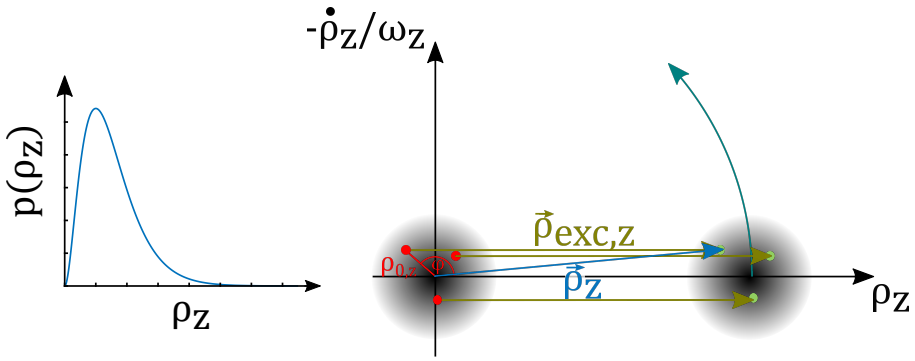

Figure 4.7.: Phase space representation of an axial dipolar excitation. Shown is the displacement for an excitation, which shifts the ion in phase space by an amount of $\rho_{z,\mathrm{exc}}$. This is illustrated exemplary for excitations occurring at different phases of the ion motion φ. Whereas the excitation leads to an increased overall amplitude, the width of the thermal distribution remains unchanged.

amplitudes. The width of the distribution of peaks is here denoted as the frequency jitter $\delta\nu_z$. By measuring this jitter, the width of the thermal amplitude distribution and thus the temperature can be determined. Whereas the thermal amplitude distribution will cause only a small frequency jitter, it can be enhanced by exciting the ion to a larger amplitude using a dipolar excitation. A dipole excitation corresponds in the phase-space picture to a displacement [157] of the cloud. The expected amplitude after excitation $|\vec{\rho}_z|$ will depend on the excitation strength that leads to a displacement of $\vec{\rho}_{\mathrm{exc},z}$, the initial ion amplitude before the excitation $\vec{\rho}_{0,z}$ and the initial phase φ difference between excitation pulse and ion motion, see fig. 4.7:

$$|\vec{\rho}_z| = |\vec{\rho}_{\mathrm{exc},z} + \vec{\rho}_{0,z}|\,. \tag{4.8}$$

Inserting above relation into eq. (2.13a), taking also contribution from C_6 into account and assuming the excitation amplitude is large compared to the initial amplitude, $\rho^2_{z,\mathrm{exc}} \gg \rho^2_{0,z}$, yields:

$$\begin{aligned}\Delta\nu_z &= \frac{C_4}{C_2}\frac{3}{4d^2}\nu_z \cdot \rho_z^2 + \frac{C_6}{C_2}\frac{15}{16d^4}\nu_z \cdot \rho_z^4 \\ &\simeq \frac{C_4}{C_2}\frac{3}{4d^2}\nu_z \left(\rho^2_{\mathrm{exc},z} + 2\rho_{\mathrm{exc},z}\rho_{0,z}\sin\varphi\right) + \frac{C_6}{C_2}\frac{15}{16d^4}\nu_z \left(\rho^4_{\mathrm{exc},z} + 4\rho^3_{\mathrm{exc},z}\rho_{0,z}\sin\varphi\right).\end{aligned} \tag{4.9}$$

The first terms in the brackets will give a general frequency shift $(\Delta\nu_z)_{\mathrm{offset}}$,

$$(\Delta\nu_z)_{\mathrm{offset}} = \frac{C_4}{C_2}\frac{3}{4d^2}\nu_z \cdot \rho^2_{\mathrm{exc},z} + \frac{C_6}{C_2}\frac{15}{16d^4}\nu_z \cdot \rho^4_{\mathrm{exc},z}, \tag{4.10}$$

whereas the second term leads to a variable frequency shift $\delta\nu_z$, depending on the initial amplitude $\rho_{0,z}$ whose variability in turn depends on the temperature of the ion before

excitation

$$\delta\nu_z = \frac{C_4}{C_2}\frac{3}{4d^2}\nu_z \cdot 2\rho_{\mathrm{exc},z}\rho_{0,z}\sin\varphi + \frac{C_6}{C_2}\frac{15}{16d^4}\nu_z \cdot 4\rho^3_{\mathrm{exc},z}\rho_{0,z}\sin\varphi. \tag{4.11}$$

Repeating this excitation multiple times and allowing the ion to re-thermalize to a heat bath each time, e.g. to the resonator or by interaction with the cooling laser, the root-mean-square of the initial amplitudes before excitation $\langle\rho_{0,z}\sin\varphi\rangle_{\mathrm{rms}}$ over many cycles can be associated to the thermal amplitude as defined in eq. (2.52):

$$\langle\rho_{0,z}\sin\varphi\rangle_{\mathrm{rms}} = \frac{\rho_{\mathrm{th},z}}{\sqrt{2}}. \tag{4.12}$$

The envelope of the peaks measured in many cycles is the convolution of the regular peak with the thermal Boltzmann distribution of the axial energy [180] resulting in a quasi Gaussian line shape. The width of this distribution $\delta\nu_z$, its offset compared to a non detuned trap $(\Delta\nu_z)_{\mathrm{offset}}$ and the excitation radius are obtained from the acquired data. The excitation radius $\rho_{\mathrm{exc},z}$ is determined from both the observed frequency shift and the known C_4 and C_6 values, whose dependencies on the tuning ratio are known from separate measurements (sec. 4.3.1). This allows to derive the thermal axial amplitude $\rho_{\mathrm{th},z}$, which is $\propto\sqrt{T}$ and relate it to the measured quantities:

$$\frac{(\Delta\nu_z)_{\mathrm{offset}}}{\delta\nu_z} = \frac{\rho_{\mathrm{exc},z}}{\sqrt{2}\rho_{\mathrm{th},z}}. \tag{4.13}$$

In Fig. 4.8 the resulting peak signals are shown. The envelope of the peaks is obtained by averaging over multiple measurement cycles. From the width of the envelope approximated by a Gaussian distribution the frequency jitter $\delta\nu_z$ is derived. By measuring the peak signal, the ion's frequency can be determined in short time without the need for a long averaging times as in case of the dip detection. Furthermore the peak is detected far off-resonant from the resonator, resulting in a weak thermal coupling to it.

4.4.2. Measurement Scheme

The temperature of the laser cooled $^9Be^+$ ion is determined using the scheme shown in fig. 4.9. The measurement is automatized using a text-based script in Matlab® [210]. The procedure is as follows:

1. At the beginning of each cycle, the ion's axial mode is thermalized with the resonator by setting the ions axial frequency to the resonator frequency. The magnetron mode is cooled by axial sideband coupling.

2. The trapping voltage is changed so that the ion's axial frequency is a few hundred Hz below the resonator frequency. Because the precision voltage source used for the BeT shows a slow drift upon voltage changes, a pause of 20 s is done to wait for the voltage to stabilize.

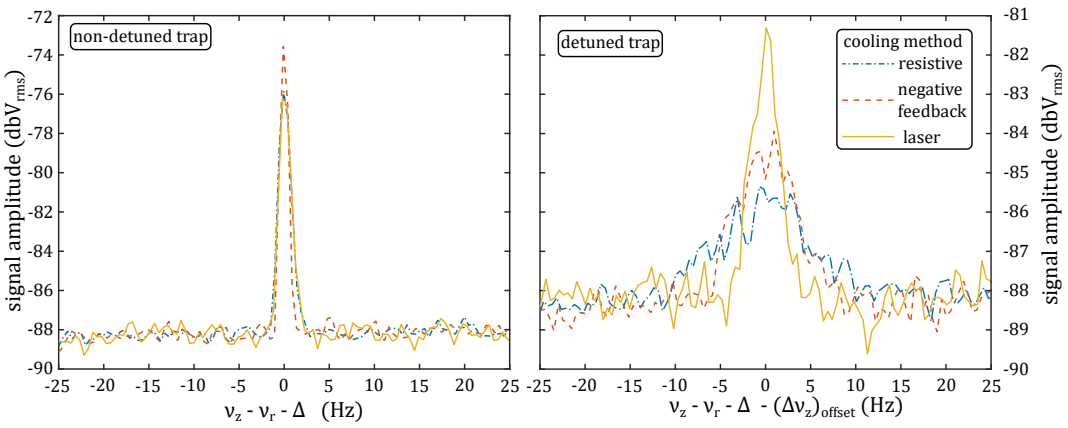

Figure 4.8.: **left** Averaged peak signals for a $^9Be^+$ ion after an excitation for a non-detuned ($TR = TR_c^{opt}$) trap. The center of the distributions is $\Delta = 500\,\text{Hz}$ on the lower side of the resonator. **right** Averaged peak signals for a detuned ($TR = TR_c^{opt} + \Delta TR$) trap to a known C_4 value. Compared to the non-detuned case, the distribution is shifted by $(\Delta\nu_z)_{offset}$ and the width of the distribution $\delta\nu_z$ is increased depending on the initial temperature axial temperature before excitation. For illustration the distributions for the three cases of a resistively (dash-dot blue), negative feedback (dashed red) and laser cooled ion (solid yellow) is shown. For all three cases the same excitation strength was used. For details see text.

3. The ion is axially excited using a burst excitation. With a short delay after the excitation, a sequence of peak spectra is acquired by the FFT analyzer at a repetition rate of 2 s. This sequence of peaks serves as reference for the determination of $(\Delta\nu_z)_{offset}$ since they are recorded for a trap with optimal tuning ratio.

4. The ion is shifted back onto the resonator and both the axial and magnetron mode are thermalized with the resonator, as in step 1.

5. Again, the ion is detuned in its axial frequency, but this time the tuning ratio is changed.

6. As in step 3, the ion is excited and the resulting peak signal is recorded.

7. Step 4-6 is repeated, keeping the same detuned tuning ratio, but for a series of different excitation strengths.

8. The cycle starts from the beginning with step 1.

After each cycle the ion frequency on the resonator is checked and if needed the trapping voltage adjusted to reinitialize the ion to its original axial frequency. This step is

necessary in order to minimize a possible detuning of the radio-frequency used for the axial coupling of the magnetron mode and to bring the ion to the same detuned axial frequency, see step 2. The aforementioned cycle is repeated multiple times in order to accumulate sufficient statistics, which corresponds to a data acquisition time of about one day. For the measurements done with the electronic negative feedback, the feedback

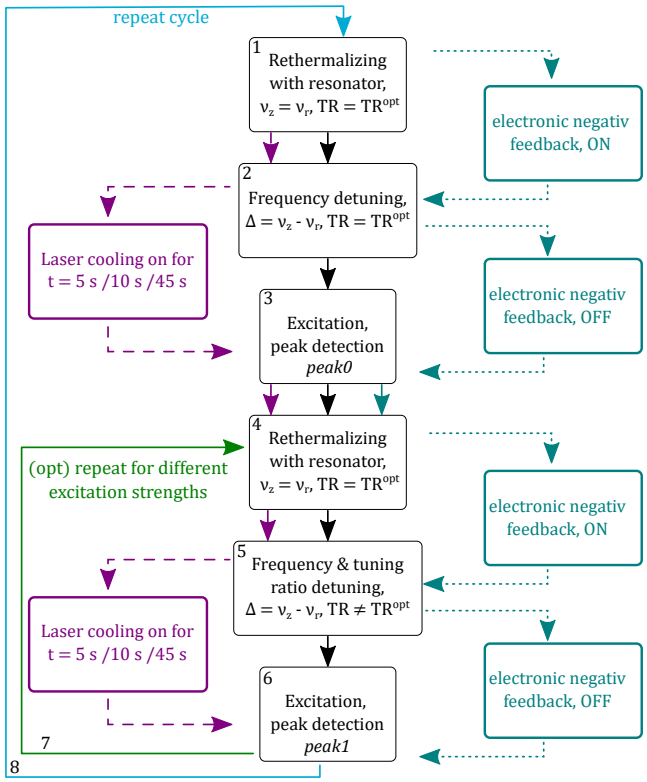

Figure 4.9.: Measurement cycle used for the temperature determination of a laser cooled $^{9}Be^{+}$ ion. The path given by the black solid arrows corresponds to a temperature measurement of an only resistively cooled ion. The flowline given by the teal dotted arrows is for a measurement using electronic negative feedback to cool the ion and the flowline described by the dashed purple arrows is for the case of the ion being laser cooled. For a detailed description of the building blocks and flow, see text.

is applied before the ion is moved off the resonator to make sure the ion is cooled further. The negative feedback is kept on throughout step 2 and turned off just before the excitation and the beginning of the peak detection to minimize a possible heating due to the resonator.

For the temperature determination of a laser cooled ion, the laser cooling is applied after the ion has been detuned from the resonator, during the time the voltage source is

stabilizing. Shortly before excitation, the laser cooling is turned off by switching a servo operated shutter.

4.4.3. Systematic Shifts and Uncertainties

In the evaluation of the experimental data obtained as described above, systematic effects and uncertainties have to be considered, which will otherwise compromise the derived value for the temperature. Centerpiece of this method is the extraction of the frequency jitter $\delta\nu_z$ and offset $(\Delta\nu_z)_{\text{offset}}$ of the distributed peak frequencies in the detuned trap compared to the non detuned case.

Resistive Damping and Heating by the Resonator

After excitation the ion is weakly resistively damped by the detection resonator such that its axial amplitude slowly decreases, while the frequency jitter of the amplitude and with it the ion's temperature slowly increases. This in turn leads in the presence of a sizable C_4, as in the case of the detuned trap, see step 5 & 6 in fig. 4.9, to a drift in the axial frequency over time. A sequence of spectra (averaging time of 2 s) is recorded with a short delay after each excitation. This drift of the axial frequency during the acquisition of a sequence affects the derived values for the center of the distribution, $(\Delta\nu_z)_{\text{offset}}$, and the jitter, $\delta\nu_z$, around the average drift in two ways. It causes not only the distribution to spread out and thus an increase of $\delta\nu_z$, but it also shifts the center of the distribution and therefore the $(\Delta\nu_z)_{\text{offset}}$ value. Since the acquisition time for the sequence is much smaller than the cooling time constant, the exponential decrease in the energy $E_z \propto (\rho_z)^2 \propto \Delta\nu_z^{C_4}$, can be approximated by a linear function. Therefore, in the analysis of the data, this effect can be compensated for by a linear extrapolation to a time of 0 s after the excitation pulse respectively the time after the laser was turned off, to derive the values $(\Delta\nu_z)_{\text{offset}}^{t_0}$ and $(\delta\nu_z)^{t_0}$, see fig. 4.10. According to eq. (4.13), the width of the distribution $\delta\nu_z$ is proportional to the thermal radius $\rho_{\text{th},z}$ which scales with $\sqrt{E_z}$. Thus, the linear extrapolation is done for $(\delta\nu_z)^2$. For the trap detuning ΔTR used in this measurement, the frequency shift $(\Delta\nu_z)_{\text{offset}}$ amounts to roughly -63 Hz and therefore the extrapolation to $t_0 = 0$ is only a small correction $< 0.4\,\%$. However, this is not the case for the width of the distributions which increase significantly over the time due to the heating effect of the resonator, see fig. 4.10. Here the extrapolation constitutes the major systematic correction and uncertainty.

Variation of the Excitation Strength

The width of the distribution, eq. (4.11), does not only depend on the initial amplitude $\rho_{0,z}$ but also on the radius to which the ion is excited, $\rho_{\text{exc},z}$. This excitation radius depends on the amplitude and duration of the used pulse. This effect has been checked for, and during the measurement no significant variation of the excitation strength has been observed. For the calculation of $\rho_{\text{exc},z}$, cf. eq. (4.10), the uncertainties of the determined offset $(\Delta\nu_z)_{\text{offset}}$ and of C_4 & C_6, whose dependencies on the ΔTR has been determined in sec. 4.3.1, are taken into account.

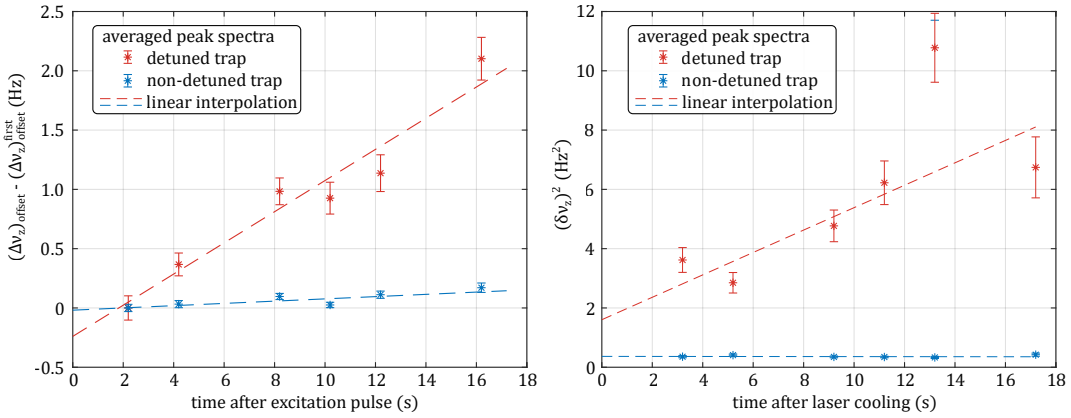

Figure 4.10.: Extrapolation of **left** the frequency offset $(\Delta\nu_z)_{\text{offset}}$ and **right** the square of the frequency jitter $(\delta\nu_z)^2$ to time $t_0 = 0$, when the laser cooling was turned off. For details see text.

Laser Induced Fluctuation of Trapping Potentials

During the measurement campaign it has been observed that the irradiation of the ion in the trap and the insertion of the laser beam into the trap setup has an effect on the temporal long term stability of the voltages on the electrodes. This can presumably be attributed to a change in patch potentials on the surface of the electrodes. As shown in fig. 4.9, during step 1 and step 4 the ions frequency ν_z is set to coincide with the resonator frequency ν_r to rethermalize the ion. Due to changing patch potentials in each cycle, the ion's axial frequency differs slightly for identical applied trapping voltages. While the measurement is ongoing, this effect is nominally compensated by determining the ions frequency from an online fit to the single dip on the resonator. The trapping voltage is adjusted accordingly such that $\nu_z = \nu_r$. This fluctuation is observed to feature also an underlying overall drift, which accumulates during the acquisition time of one data set to a frequency shift, comparable to the width $\delta\nu_z$ of the distribution. The underlying mechanism of this drift is not finally understood but it is modeled in first order to be linear. In the evaluation of the data, this can be accommodated for, by shifting the individual peak spectra by a correction derived from the observed and assumed linear drift, see fig. 4.11. In case the assumed linear behavior is not true, the derived temperature is overestimated, which justifies above approximation. The assumed to be laser induced patch potentials can change the C_2 and C_4 values of the externally applied trapping potential. Even though the exact change of the individual C_i is not fully understood yet, the effect on the final results here is only a small contribution to the overall error budget. Further investigations on this effect are wanted.

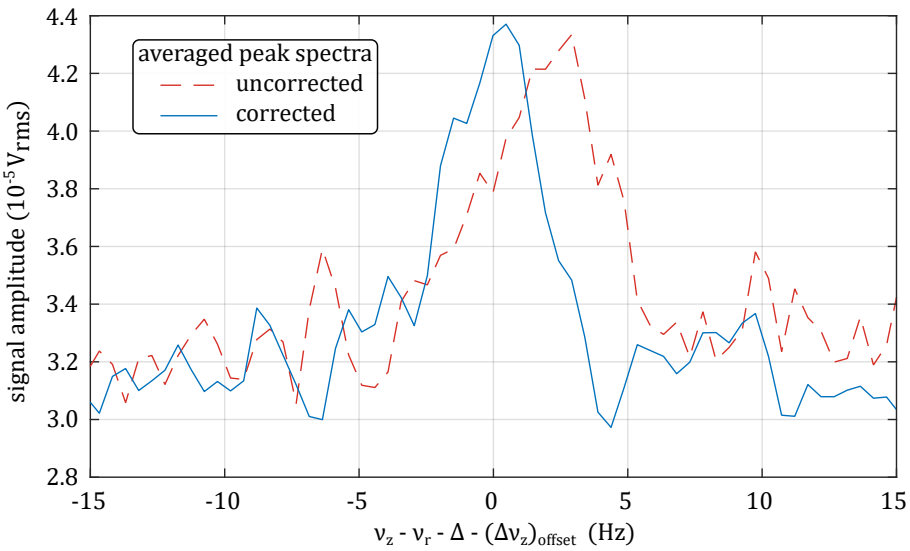

Figure 4.11.: Averaged spectrum of the peak distribution for a detuned trap. The red dashed line shows the averaged peak signal for the uncorrected peaks. The compensation of the individual spectra for the observed overall drift before averaging leads to a shifted and narrowed distribution (solid blue).

Imperfect Stabilty and Repeatability of the Voltage Source

On short time scales between cycles a fluctuating axial frequency can be observed. This jitter of the axial frequency $\delta\nu_z^{\mathrm{pot}}$ can be determined from online fits to the individual dips after the ion frequency is set to the resonator frequency. It is superimposed to the thermal jitter and can be caused by changing patch potentials as well as by the imperfect voltage stability and reproducibility of the employed voltage source. Since these two fluctuations are assumed to be independent, they add quadratically and the "true" thermal frequency jitter $\delta\tilde{\nu}_z$ can be found by correcting the the value for the frequency jitter from the width of fit to the axial frequency distribution $\delta\nu_z$:

$$\delta\tilde{\nu}_z = \sqrt{\left((\delta\nu_z)^2 - \left(\delta\nu_z^{\mathrm{pot}}\right)^2\right)} \tag{4.14}$$

In addition due to the changing trap potentials, the tuning ratio $TR_{\mathrm{c}}^{\mathrm{opt}}$ needs to be manually re-optimized before the start of each measurement run, see sec. 4.3.1.

Lineshape

Both the frequency offset $(\Delta\nu_z)_{\mathrm{offset}}$ and jitter $\delta\nu_z$ can be obtained after averaging of the peak spectra, the linear amplitude data, of all cycles. A Gaussian function is fitted to the resulting envelope of the distributed peaks (fig. 4.8). The slope of the noise floor

level in wings of the resonator depends on the selected frequency detuning and is taken into account for fitting. This slope in a small region around the peak distribution can be in first order approximated to be linear. Therefore the fitted function is: $y(x) = a\exp\left(-\frac{(x-\mu)^2}{2\sigma^2}\right) + dx + e$. Simulations of the expected lineshape being a convolution of a thermal Boltzmann distribution and a Gaussian due to the excitation yield that the Gaussian contribution is dominant and the contribution to the error of the final temperature value below 2 % [211].

4.5. Final Results

The linear polarized laser has been tuned to the red side of the initially calculated $^2S_{1/2}$ $|-3/2,-1/2\rangle \rightarrow {}^2P_{3/2}$ $|-3/2,-3/2\rangle$ transition frequency in order to not accidentally heat the ion. In order to find the exact transition frequency for laser cooling to occur, the ion axial frequency is set to the side of the resonator and excited to yield a peak signal. Without the laser, the ion re-thermalizes with the resonator on a timescale given by the cooling time constant on which the peak disappears. For the herein typically used ion axial frequency detunings, $\Delta = \nu_z - \nu_r$, of $\Delta = -1000/-500/0$ Hz these calculated cooling time constants are 354/ 88/ 0.2 s. With the laser cooling the ion, the re-thermalization rate is increased and the peak is disappearing in shorter time, see fig. 4.12. These results show that the laser cooling is acting on typical timescales of a few seconds. This is assumed to be due to the time it takes to repump the ion out of the dark state. The overall efficiency of the laser cooling is reduced since the polarization of the laser beam has been linear. Using the correct circular polarization would reduce the depopulation of the bright state into the darkstate, see sec. 4.1. Furthermore, the laser pointing is not stabilized which leads to beam position offset over time and realignment of the beam is done with this method minimizing the damping time of the excited ion. These effects lead to a laser cooling time which is longer than the expected time derived from simulations. Both of these issues will be addressed and improved in future measurements. Using the frequency found in this way, systematic measurements were done to narrow down the transition frequency. Since the Doppler width of the cooling transition amounts to 511 MHz at 5 K, the ion is not irradiated by the laser with a fixed frequency but rather the laser is swept up-and-down by a triangular frequency modulation of typically ±100 MHz to ±200 MHz around a central frequency to improve the cooling. The time for one period of a triangular sweep is 7 s, resulting in a slew rate of 57 MHz/s to 114 MHz/s and typical laser irradiation times are 10 s to 45 s.

After these preparatory measurements, the case of a laser cooled $^9Be^+$ ion is considered. In order to check the reliability and robustness of the aforementioned method, the temperature is first measured for a single $^9Be^+$ ion that is in thermal equilibrium with the axial AT resonator. The measured axial temperature is 5.5(2) K which is in good agreement with the expectation of 4 K to 5 K for the axial resonator being in thermal equilibrium with the liquid helium cryostat and not contributing additional electronic noise. Furthermore, as a consistency check, a measurement is done with the ion being cooled by negative electronic feedback (sec. 2.7.2). In this case a temperature of 2.0(1) K

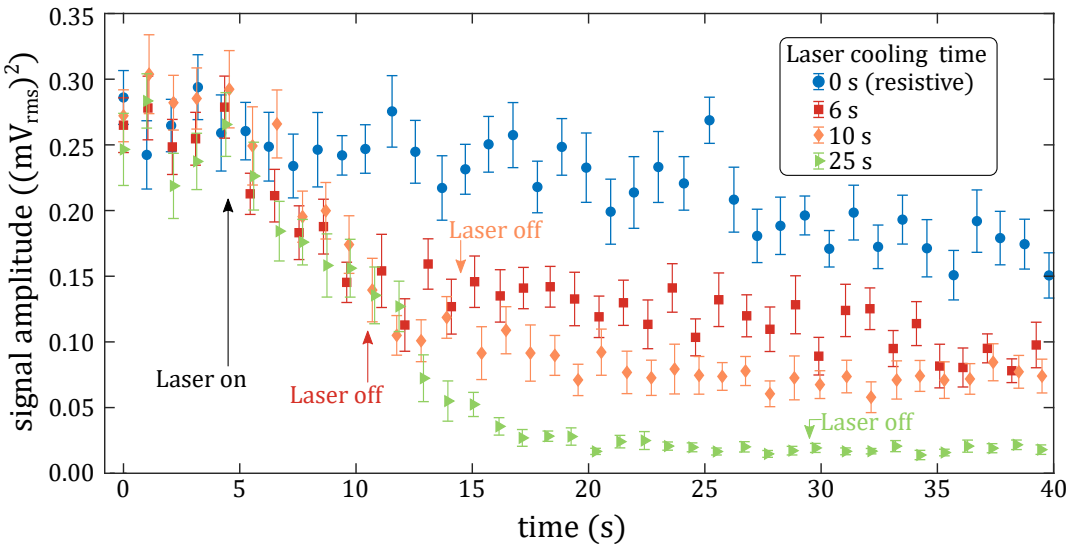

Figure 4.12.: Influence of the laser cooling on the damping of an excited ion on the side of the resonator. Shown is the signal height of the ion excited to a peak as a function of time. Without the laser (blue dots), the ion is only damped by the off-resonant axial AT resonator. The damping is enhanced when the laser is on and therefore the peak amplitude is decreasing faster (colored dots). Once the laser is shut off again, the damping continues with the rate as in the resistive only case.

is measured, consistent with the expected temperature reduction by the feedback. In the case of the measurements with the resistive and negative feedback cooling, the frequency jitter is determined for different excitation strengths in each experiment. This allows to check the method for self-consistency and systematic amplitude respectively energy dependent uncertainties. The measurements with the laser cooling are all done with one excitation strength for having a reasonable overall measurement time.

After these preparatory steps, the case of a laser cooled $^9Be^+$ ion is considered. A series of measurement has been done in order to find the optimal settings for the temperature determination and following parameters have been varied:

- The axial frequency detuning $\Delta = \nu_z - \nu_r$ of the ion with respect to the resonator. A frequency detuning of either 500 Hz or 1000 Hz has been used. The larger the frequency detuning, the lower is the signal-to-noise ratio which makes it more difficult to see the excited ion, which also requires larger excitations.

- The applied tuning ratio detuning. Before each measurement the optimal tuning ratio TR_c^{opt} is determined by exciting the ion on the side off the resonator in a non-detuned trap. While the ion is resistively cooling back, the frequency changes

in presence of a sizable C_4. This frequency change is minimized so that during the time a sequence of peaks is recorded, the chirp is less than one bin width of the FFT. The optimal tuning ratio is then detuned by ΔTR to $TR = TR_c^{opt} + \Delta TR$. The larger ΔTR the larger is the frequency jitter $\delta\nu_z$ and more measurement cycles are required to obtain enough statistics to fit the envelope of the peak distribution.

- The laser frequency which is scanned during the irradiation. The frequency was varied to approach the exact frequency for the laser cooling cycle iteratively.
- The time t_l during which the laser cooling is applied to the ion. Because the laser is affecting the stability of the trapping potentials, it has been tried to minimize t_l.

The lowest temperature was determined for an axial frequency detuning $\Delta = \nu_z - \nu_r \simeq 1000\,\text{Hz}$ and $\Delta TR = 0.01$. The laser was irradiated for 10 s and sweeped by $\pm 100\,\text{MHz}$ around 957.340 500 THz. This way an estimate for the upper limit for the axial temperature of the $^9Be^+$ ion can be given:

$$T_z \lesssim 69\ (30)\ (1)\ (1)\ (3)\ \text{mK}. \tag{4.15}$$

The first error is from the uncertainty in the determination of the frequency jitter $\delta\nu_z$ due to fitting of the peak distribution envelope, the extrapolation in time and drift correction of the individual peaks. The second error is arising from the uncertainty of $\rho_{exc,z}$ which was determined according to eq. (4.10). The third and the last error are due to the uncertainty for the deterministically applied C_4 and C_6, whose values are derived from the measurement described in sec. 4.3.1.

These results are a successful demonstration of laser cooling of the axial mode. In those measurements in which the upper limit has been 200 MHz higher than 957.340 600 THz already a heating can be observed. Therefore it can be assumed that the lowest temperatures are achieved for red-detuned frequency sweeps up to 957.340 600 THz, which has to be close to the nominal transition frequency.

Since the above-mentioned method of temperature determination has some limitations, the above stated value is considered to be an upper estimate for the actual temperature the ion is cooled to by the laser. The main limitation of this method is reached when the fluctuations of the peak distributions, caused by either the voltage source or laser induced patch potentials changing the C-coefficients, becomes comparable to the thermal jitter which is tried to be measured. This can be circumvented by using a larger ΔTR to increase both the axial frequency shift and the jitter. Since a larger C_4 also causes larger drifts of the axial frequency, the ion's frequency has to be offset further from the resonator to increase the cooling time constant τ. This in turn reduces the signal-to-noise ratio and larger excitations are needed to detect a peak, which are then prone to systematic uncertainties by contributions from C_6. Furthermore, the efficiency of the laser cooling might be reduced or changed in time, since there is no laser beam stabilization used. This leads to a change of the beam center and thus reduced intensity at the position of the ion. Later measurements revealed drifts in the pointing of the laser

beam, on the distance between the laser head and the trap center, of up to 300 µm on a time scale of 15 h and sudden jumps of up to 1 mm [193]. The drifts might have been be caused by ground vibrations or changes in the ambient room temperature, since both laboratories are not temperature stabilized. Sudden jumps in the pointing of the laser beam are correlated to vibrations or impacts on the laser table or quickly closing and opening laboratory doors. This will affect the efficiency of the laser cooling as also the observed cooling rate is lower than expected from simulations [211]. The first step to address this issue is the installation of a real-time active laser beam stabilization system which is currently work in progress.

5. Experimental Results: Fine Structure Laser Spectroscopy of $^{40}Ar^{13+}$

This chapter discusses the main results obtained in the course of this PhD thesis. In the measurement campaign on $^{40}Ar^{13+}$ a novel measurement scheme, proposed by ALPHATRAP's PI Sven Sturm, was demonstrated for the first time and is presented in the following. For these measurements the group of Prof. Wilfried Nörtershäuser, from the Technische Universität Darmstadt, Germany, collaborated with ALPHATRAP and provided the necessary laser system. The results are published in Physical Review Letters [71]. The details and results of this measurement will be outlined in this chapter.

5.1. The Fine Structure of $^{40}Ar^{13+}$

The electronic ground state of the boronlike five-electron system $^{40}Ar^{13+}$ is the $2p\,^2P_{1/2}$ configuration. The g-factor of this level has been subject of a previous measurement [27, 40] performed by Ioanna Arapoglou, a former PhD student at ALPHATRAP. It constitutes the first high-precision measurement of the g-factor of a boronlike system, testing theoretical predictions for many-electron, QED and nuclear recoil contributions. For this thesis, laser spectroscopy of the ground-state fine-structure splitting is performed.

The second lowest lying electronic level is the fine structure $2p\,^2P_{3/2}$ state. The separation to the $2p\,^2P_{1/2}$ ground state is about 2.81 eV, corresponding to a transition wavelength of 441.2 nm or a frequency ν_0 of 679 THz, which allows to access it by laser spectroscopic investigations. The transition is an electric dipole (E1) forbidden transition, but allowed as magnetic dipole (M1) transition. Typical approaches for detecting forbidden transitions using a three level scheme or electron-shelving techniques cannot be applied in this case because a third laser-accessible state is missing. The ^{40}Ar nucleus does not carry a nuclear spin ($I=0$) and therefore the level structure does not exhibit a hyperfine structure. In a nonzero magnetic field, the degeneracy of the magnetic substates is lifted and each fine-structure level splits into a manifold with $2J+1$ Zeeman sublevels, which are identified by their respective magnetic quantum number m_J ranging from $m_J = -J, -J+1, ..., J-1, J$. In a magnetic field of 4 T, as applied within the PT, the Zeeman shift amounts to up to ± 112 GHz as for the $m_J = \pm 3/2$ sublevels of the $2p\,^2P_{3/2}$ state, see fig. 5.1. The change of the projection value of the ion's magnetic moment between the $|J, m_j\rangle = |1/2, -1/2\rangle$ ("spin down", $|\downarrow\rangle$) and $|1/2, +1/2\rangle$ ("spin up", $|\uparrow\rangle$) levels separated by a Larmor frequency ν_L of 37.2 GHz will cause a difference in the axial frequency $\Delta\nu_z$ of 309 mHz in the magnetic bottle of the AT. The spin state of the ion in its ground state cannot only be detected with high fidelity but also be prepared in

one specific Zeeman level using microwave radiation in the AT. This is a distinct feature on which the presented method relies.

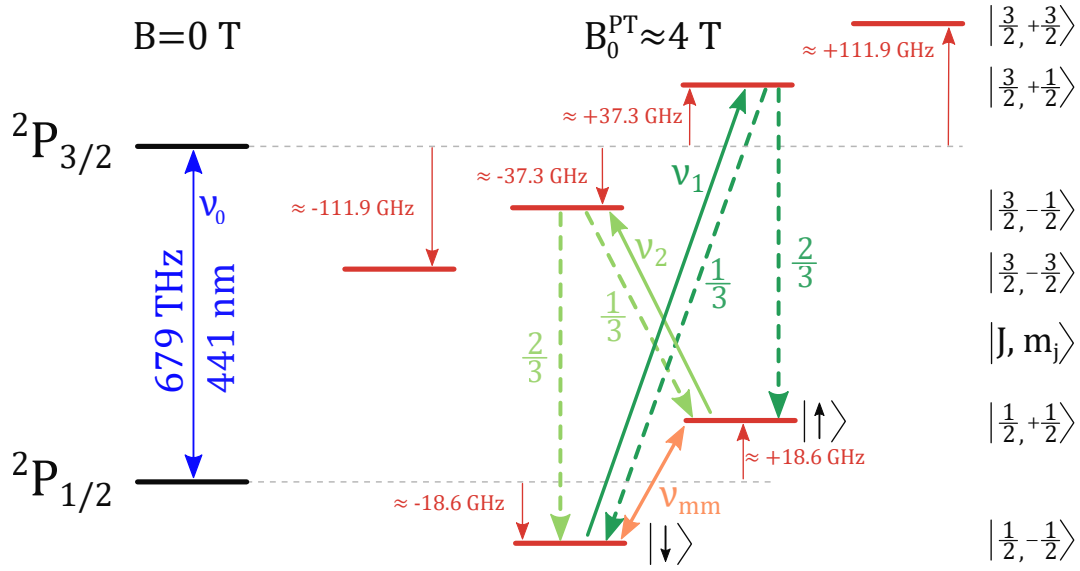

Figure 5.1.: Level scheme for $^{40}Ar^{13+}$ at zero magnetic field and at a field of around 4 T. The magnetic field lifts the degeneracy of the fine structure levels and a splitting of several tens of GHz between the Zeeman substates can be observed. The laser driven transitions $\nu_{1,2}$ of frequency ≈ 679 THz are denoted by the solid lines. The dashed lines show the possible spontaneous decay channels of the excited states with the corresponding branching ratio. Vertical axis not to scale.

5.2. Measurement Procedure

Being an optical M1 transition results in a rather long lifetime τ of the excited $^2P_{3/2}$ state of 9.573(6) ms [212, 213] and thus a natural linewidth of $\Gamma = \frac{1}{2\pi\tau} = 16.6(10)$ Hz. Due to a therefore expected low fluorescence rate, a detection based on the observation of the fluorescence is technically extremely challenging [214, 215]. With the method presented herein, high-precision laser spectroscopy of this electric dipole forbidden transition becomes possible using only a single ion stored at low energies in the Penning-trap system of ALPHATRAP. The method is based on the unambiguous detection of the projection value of the ion's magnetic moment onto the magnetic field axis, using the continuous Stern-Gerlach Effect (CSGE, see section 2.5) in the AT. In this novel scheme there is no need for fluorescence detection. Instead of observing the transition, manifesting in the emission of fluorescence photons, rather the final state after the transition is accomplished is determined.

The measurement procedure is similar to the one used in earlier experiments for g-factor measurements with a double-trap setup [25, 83]. For the determination of the transition frequency ν_1 the measurement routine, which is executed fully automatized by a Matlab script controlling the experiment, is as follows:

1. In the AT, the ion is initialized in the $|1/2, -1/2\rangle$ state, by irradiation with millimeter waves of frequency ν_{mm} that equals the transition frequency ν_{L} between the spin down and spin up state, $|\downarrow\rangle \leftrightarrow |\uparrow\rangle$. To determine the spin state, a phase-sensitive technique is used (see sec. 5.6) instead of detecting the spin state dependent change in the axial frequency via single dip spectra. The axial phase is calculated from the standard deviation of four consecutive phase measurements. In case the stability exceeds a threshold value, then the ion is adiabatically transported to the PT. There the cyclotron mode is cooled by a sideband coupling to the axial mode which is simultaneously cooled by negative electronic feedback. Then the ion is adiabatically transported back to the AT, where it is initialized as described in step 1.

2. The ion is adiabatically transported from the AT to the PT.

3. In the PT the magnetron mode is cooled by sideband coupling to the axial mode.

4. The laser is tuned to the probe frequency, which is selected in a randomized order from a predefined range of frequencies. Then the laser shutter is opened for an irradiation time between 22 s and 66 s and at different laser powers for different measurements:
   a) Measurements done using *negative electronic feedback*: Before the laser irradiation, the axial mode is cooled by applying a negative electronic feedback, whose strength is monitored online and if necessary the attenuation of the feedback is adjusted to match the desired feedback strength, see sec. 2.7.2.
   b) Measurements done with the *adiabatically cooled* ion: Before the laser irradiation, the trapping potential is adiabatically relaxed by reducing the negative trapping voltage by a factor of ξ, as explained in sec. 2.7.1.
   c) Measurement done with the combination of negative electronic feedback and adiabatic cooling: First the negative feedback is applied, (step a), and then the trapping voltage is changed, (step b), while the feedback is still turned on. Once the lowered trapping potential is reached, the feedback is turned off and the laser irradiation starts as described in step 4.

5. Adiabatic transport from PT to AT.

6. Determination of the spin state in which the ion arrived at the AT.

7. Start over with step 1 and repeat this cycle multiple times for different laser probe frequencies.

The ion is initially prepared with low cyclotron energy. In case the sideband coupling to the axial mode (step 1) yields a to high cyclotron energy, the coupling is repeated until the energy after coupling is again similar to the initial one. The procedure for ν_2 is analogue, whereas the signs in the corresponding m_j states are inverted, see fig. 5.1. By comparing the initially prepared spin state (step 1) with those determined after the laser irradiation (step 6), the frequency-dependent spin state transition rate can be derived and a resonance be sampled.

5.3. Line-Shape Model of the Resonance

The natural linewidth Γ of the transition $|1/2, \mp 1/2\rangle \leftrightarrow |3/2, \pm 1/2\rangle$ is 16.6(10) Hz. But since the ion is bound in the harmonic axial potential, the effective absorption resp. emission spectrum of the ion is not a single Doppler broadened line but features a substructure. This can be understood by looking at how either the electromagnetic field of the incoming laser radiation in the ion's frame of reference is modulated or how an observer in the laboratory frame sees the light emitted from the ion, modulated by its periodic axial oscillation [216].

As the ion oscillates $z(t) = z_0 \sin(\omega_z t)$, where z_0 is the current maximal axial amplitude, the magnetic field component[1] $\vec{B}_\mathrm{L}$ of the laser radiation with frequency ω_L is modulated. If the incident plane wave is aligned with the z-axis the magnetic field seen by the ion $\vec{B}_\mathrm{ion}$ can be written as [72, 134]:

$$\vec{B}_\mathrm{ion}(t) = \vec{B}_\mathrm{L} \cos(k_\mathrm{L} z(t) - \omega_\mathrm{L} t) = \vec{B}_\mathrm{L} \cos(k_\mathrm{L} z_0 \sin(\omega_z t) - \omega_\mathrm{L} t) \tag{5.1}$$

with $k_\mathrm{L} = \left|\vec{k}_\mathrm{L}\right| = \frac{2\pi}{\lambda_\mathrm{L}}$ being the projection of the wave vector of the laser beam onto the z-axis. This relation is the same as for a signal of frequency ω_L, which is frequency modulated by a frequency ω_z with a modulation index of $\eta = k_\mathrm{L} z_0$. Therefore eq. (5.1) can be expressed in frequency space as a series of Bessel functions $J_\alpha(\eta)$ of first kind and second order:

$$\vec{B}(\omega) = \vec{B}_\mathrm{L} \sum_{\alpha=-\infty}^{+\infty} J_\alpha(\eta). \tag{5.2}$$

The modulation index η equals the Lamb-Dicke parameter as defined in sec. 2.7.3. The complete absorption spectrum $\sigma(\omega)$ is then given by combining the intensity $I(\omega)$ of the laser beam, which is proportional to the amplitude square of the magnetic field $|B(\nu)|^2 = B(\nu)\overline{B(\nu)}$, with the atomic cross section for absorption [72, 134]:

$$\sigma(\omega) = \sigma_0 \frac{(\Gamma/2)^2}{(\Gamma/2)^2 + [\omega_\mathrm{L} - (\omega + \omega_z)]^2} \sum_{\alpha=-\infty}^{+\infty} |J_\alpha(\eta)|^2 , \tag{5.3}$$

where σ_0 is the resonance scattering cross section. In frequency space the carrier frequency is then symmetrically surrounded by sidebands equally spaced by ν_z around the

[1] Same holds true for the electric field component, but since it is a magnetic dipole (M1) transition, the magnetic field component is used here.

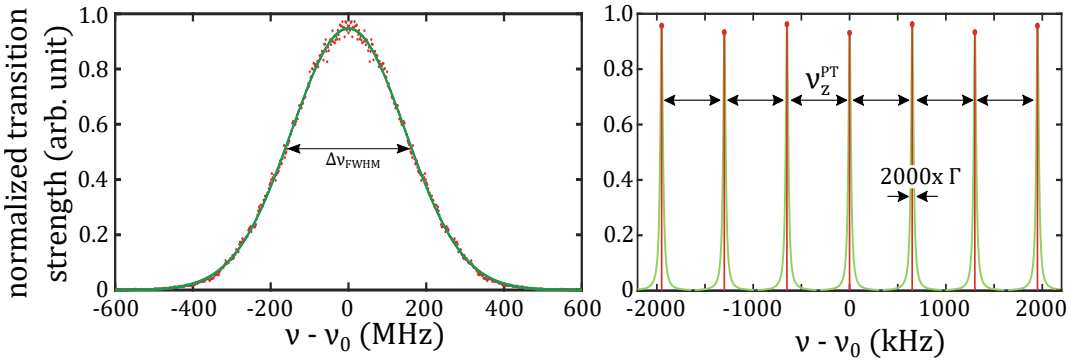

Figure 5.2.: Simulation of the expected sideband spectrum. **left** Normalized transition strength (dots) at frequencies $\nu = n \times \nu_z^{\mathrm{PT}} + \nu_0$ around the transition frequency ν_0 evaluating eq. (5.6) for an ion with temperature $T_z = 19.5\,\mathrm{K}$ in thermal contact with the axial PT resonator. A Gaussian fit (solid line) to the resulting envelope yields a FWHM equal to the broadening one would expect for an ideal gas of the same temperature, eq. (5.7). **right** Detailed view in a frequency range of $\pm 3 \times \nu_z^{\mathrm{PT}}$ around the carrier frequency ν_0. For better visualization the spectral linewidth $\Gamma = 16\,\mathrm{Hz}$ of the individual sidebands is increased by a factor of 2000. The equidistant spacing between the sidebands equals the axial frequency $\nu_z^{\mathrm{PT}} = 650\,\mathrm{kHz}$.

carrier. The strength of the individual sidebands compared to the carrier transition is given by the modulation index

$$\eta = \frac{\text{peak frequency deviation}}{\text{modulation frequency}} = \frac{\sqrt{\frac{2E_z}{mc^2}}\nu_0}{\nu_z}, \tag{5.4}$$

where the peak frequency deviation is given by the first order Doppler shift and the modulation frequency equals the axial frequency of the ion in the trap. Fig. 5.2 shows exemplarily such a sideband spectrum for one specific ion axial energy. As discussed in sec. 2.3.3, the ion is in thermal equilibrium with the resonator and the energy of the ion follows the thermal Boltzmann distribution [83] in which the probability density $p(E_z)\mathrm{d}E_z$ is given by

$$p(E_z)\mathrm{d}E_z = \frac{1}{k_{\mathrm{B}}T_z} e^{-\frac{E_z}{k_{\mathrm{B}}T_z}} \mathrm{d}E_z, \tag{5.5}$$

see also fig. 2.7. Combining eq. (5.3)-(5.5) the overall spectrum $\sigma^{\mathrm{total}}(\omega)$ is obtained by integration over all individual sideband spectra which are depending on the ion energy:

$$\sigma^{\mathrm{total}}(\omega, T_z) = \int_0^\infty \sigma(\omega, E_z)\, p(E_z)\mathrm{d}E_z. \tag{5.6}$$

The envelope of this structure corresponds to a Gaussian distribution, whose FHWM $\Delta\nu_{\mathrm{FWHM}}$ equals the value for the Doppler broadening of a transition in an ideal gas of

the same temperature $T = T_z$ as the ion's axial temperature:

$$\Delta\nu_{\mathrm{FWHM}} = \sqrt{\frac{8\ln(2)k_{\mathrm{B}}T_z}{mc^2}}\nu_0, \tag{5.7}$$

where ν_0 corresponds to the transition frequency in the rest frame of the ion, see fig. 5.2. Sidebands of the radial modes [217] are not observed, because of the orientation of the laser beam. The beam is ideally aligned along the vertical trap axis and therefore the projection value of the wave vector onto the radial axes is zero.

With the laser system used for this measurement, see sec. 3.5.2, the individual lines spaced by ν_z cannot be resolved, since the frequency stability and linewidth is not sufficient. Using a laser system which allows to resolve the individual lines, spectroscopy down to the natural linewidth could be possible. By varying the axial trapping potential depth the carrier frequency ν_0 could be found and determined by fractions of the linewidth[2]. In the experimental situation found at ALPHATRAP at the moment, the achievable uncertainty is limited by the width of the resonances by the first order (linear) Doppler effect and thus the temperature of the ion, see fig. 5.7.

5.4. Temperature Measurement of the Axial Mode

Since the width of the acquired resonances depends on the temperature of the ion, it is of importance to have an independent method to determine the ion's axial temperature in the PT during the interrogation of the laser transition frequency. The method used is based on energy dependent frequency shifts in the magnetic bottle of the AT [123]. Using a cyclotron to axial sideband coupling in the PT, the thermal Boltzmann distribution of the axial energy can be mapped onto the cyclotron mode, see eq. (2.40). After an adiabatic transport from the PT to the AT, the axial frequency $\nu_z^{\mathrm{AT}}(E_+)$ in the AT will be shifted depending on the cyclotron energy according to eq. (2.17a) by [25, 123]:

$$\Delta\nu_z^{\mathrm{AT}}\left(E_+^{\mathrm{AT}}\right) = \frac{B_2^{\mathrm{AT}}}{B_0^{\mathrm{AT}}\left(2\pi\right)^2\nu_z^{\mathrm{AT}}m}E_+^{\mathrm{AT}}. \tag{5.8}$$

For an optimized TR of the AT, shifts due to electric field imperfections or relativistic mass increase are negligible compared to the shifts arising from the strong B_2^{AT}. Repeating this cycle multiple times the measurement of the ν_z^{AT} distribution allows to derive the distribution of the cyclotron energies and thus the temperature of this mode. From a fit of $\exp(-\Delta\nu_z^{\mathrm{AT}}/k_{\mathrm{B}}T_+^{\mathrm{AT}})$ to the binned distribution of $\Delta\nu_z^{\mathrm{AT}}$, the cyclotron temperature T_+^{AT} in the AT can be derived, see fig. 2.7. Because the magnetic moment created by the radial motion is invariant under adiabatic transport, the cyclotron amplitude and thus also the ratio of cyclotron energies, E_+^{AT} and E_+^{PT} scales by the ratio of the magnetic

[2] Assuming the carrier frequency could be determined by 1/10 of its natural linewidth Γ and having a complete understanding and control of all systematic effects, this would result in a frequency measurement with $< 2.4\times10^{-14}$ relative uncertainty.

fields $B_0^{\mathrm{PT}}/B_0^{\mathrm{AT}}$. Using this relation and eq. (2.53a) the axial temperature of the ion, T_z^{PT}, in the PT can be written as:

$$T_z^{\mathrm{PT}} = \frac{\nu_z^{\mathrm{PT}}}{\nu_+^{\mathrm{PT}}} \frac{B_0^{\mathrm{PT}}}{B_0^{\mathrm{AT}}} T_+^{\mathrm{AT}}. \tag{5.9}$$

These measurements reveal a variable temperature of 12 K to 20 K, which is higher than expected but in good agreement with the observed FWHM of the transitions measured by laser spectroscopy. To the detector circuit, with which the ion is in thermal equilibrium, an effective temperature T_{eff} can be assigned. The effective temperature has contributions from the thermal Johnson-Nyquist noise u_{JN}, cf. eq. (2.33), and from uncorrelated electronic noise of the detector circuit u_{el}, which add quadratically [84]

$$T_{\mathrm{eff}} = \frac{u_{\mathrm{JN}}^2 + u_{\mathrm{el}}^2}{4k_{\mathrm{B}}\Re\left(Z\right)}. \tag{5.10}$$

This is observed also in earlier measurements [84] and is caused by additional electronic noise that could later be attributed to a broken capacitor, which got replaced after the end of the measurement campaign. The elevated temperature leads merely to an increased FWHM of the resonances, but does not cause a mean shift of the center. Also possible effects due to the second order Doppler shift are negligble, see sec. 5.8.3.

5.5. Single Ion Preparation

$^{40}\mathrm{Ar}^{13+}$ ions can be easily produced in the prototype HC-EBIT, as demonstrated earlier [162, 165]. An ionization energy of 686 eV [196] is required to ionize injected argon gas to the boronlike charge state $^{40}\mathrm{Ar}^{13+}$. The Wien filter allows to select the wanted q/m of $^{40}\mathrm{Ar}^{13+}$ and after the transport to the Penning-trap system, the ions are captured in the CT. From there a fraction of a large cloud of ions can be transported to the PT. By repeated excitations of the different modes and switching the trap to a shallow potential, all except one ion can be ejected, see [40]. This single ion can then be cooled in all eigenmodes using sideband couplings and be prepared in a specific Zeeman substate by using millimeter waves and the spin state detection in the AT, see sec. 2.5. The results presented in the following paragraphs were obtained using only two single $^{40}\mathrm{Ar}^{13+}$ ions. The first nine resonances were taken with a single ion stored for 18 weeks. In order to exclude systematic effects that could arise from parasitically co-trapped ions, the first ion is replaced by a second single $^{40}\mathrm{Ar}^{13+}$ ion, which was similarly prepared as described above.

5.6. Phase-Sensitive Spin State Detection

The measurement scheme, described in sec. 5.2, is similar to the one done in the measurement campaign for the g-factor of the $^{40}\mathrm{Ar}^{13+}$ ground state [40]. In this previous g-factor measurement campaign the read out of the spin state in the AT was done by

extraction of the axial frequency from a fit of the axial dip and comparing it to the axial frequency of the previous one before irradiation with the millimeter waves.

In order to reduce the overall measurement time for one resonance for the measurement campaign reported here, the detection of the spin state in the AT is done using a phase-sensitive measurement method [218]. For this purpose the ion is excited by a well-defined dipolar burst excitation imprinting a fixed phase onto the ion, cf. sec. 2.4.1. Then the resonance frequency of the axial AT resonator is shifted to a $\approx 10\,\mathrm{kHz}$ higher value[3] by using a fast-switchable parallel capacitance [84]. In this way the ion is decoupled from the resonator, which allows a free undisturbed phase evolution of the axial oscillation for a time t_{evol}. After switching back the resonator to its initial value, from the complex Fourier transform of the signal a phase can be determined, see fig. 5.3. From

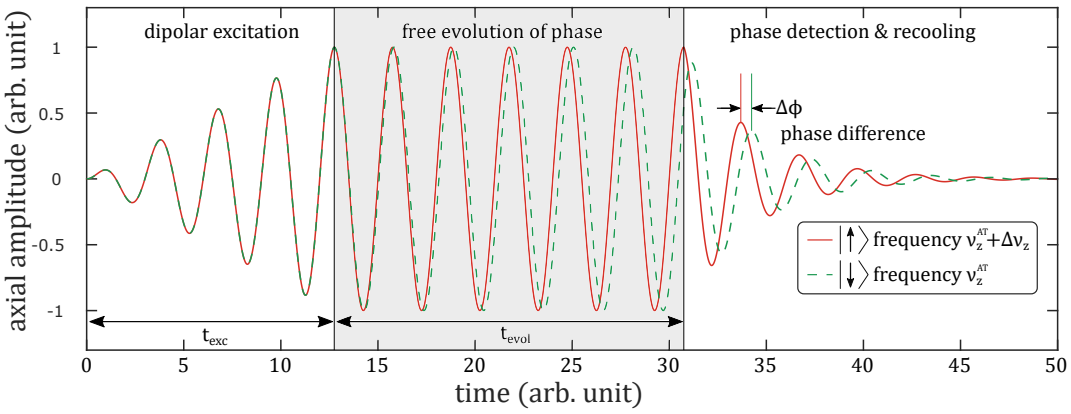

Figure 5.3.: Schematic explanation of the phase-sensitive method for the detection of spin-state transition in the AT. By the initial dipolar excitation a fixed phase is imprinted onto the ion. During a time t_{evol} the ions is evolving unperturbed and decoupled from the axial resonator. The different spin states exhibit a slight frequency difference ϵ which can be read out from the FFT spectrum after the phase evolution period.

the previously determined B_2^{AT} [40, 84] and eq. (2.48) the axial frequency difference $\Delta\nu_z$ between the $|\downarrow\rangle \leftrightarrow |\uparrow\rangle$ states (sec. 5.1) is expected to be 309 mHz for an axial frequency $\nu_z^{\mathrm{AT}} = 335\,\mathrm{kHz}$. Therefore the phase evolution time t_{evol} of 800 ms is chosen such that for a spin state the transition, the phase difference between two back-to-back measurements amounts to $\pm 90°$ respectively $\pm\pi/2$. Fig. 5.4 shows an example of the spin-state determination in the AT. For an increased robustness and fidelity of the spin-state determination a set of four consecutive phase measurements is done and averaged. Then the millimeter waves are irradiated and another set of four phase values is measured. In case the difference of the means of both quadruples satisfies predefined upper and lower threshold values, the attempted change of the spin state by the millimeter waves

[3] This values corresponds to about 200× the 3dB-bandwidth of the axial AT resonator.

is considered successful. This way both the determination of the spin state after the laser irradiation in the PT and the preparation in a specific spin state $|\uparrow\rangle$ or $|\downarrow\rangle$ can be accomplished (compare sec. 5.2).

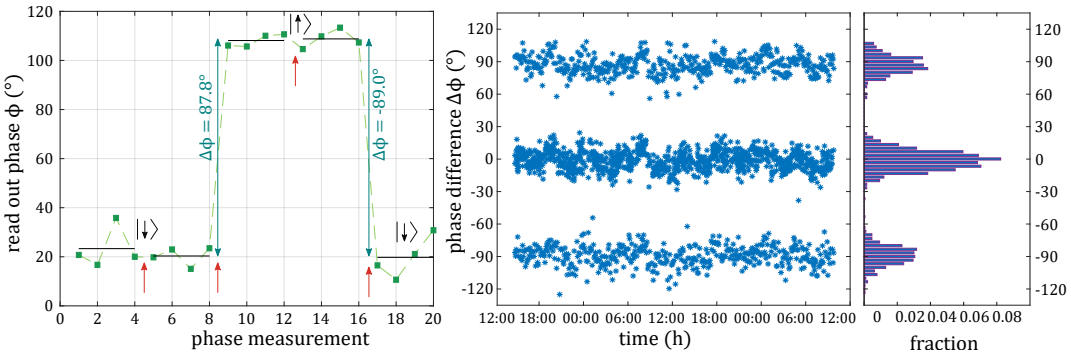

Figure 5.4.: **left** Exemplary readout of the phase for subsequent measurements. After every fourth measurement, the millimeter wave is irradiated (red arrows). In case of a spin-state transition, a jump in the phase is observed (teal arrows). The solid lines are the means for a set of four consecutive phase read outs. In the shown example the sequence of spin states is $|\downarrow\rangle \rightarrow |\uparrow\rangle \rightarrow |\downarrow\rangle$. **middle** Measured phases of many cycles over a time span of 14 h. For 0° no spin-state transition happened, whereas a change of ±90° indicate a transition between the $|\downarrow\rangle \leftrightarrow |\uparrow\rangle$ states. **right** The histogram of the data in the middle reveals the sharp discrimination between the different spin states.

5.7. Calculation of Zeemanshifts

The two transitions ν_1 and ν_2 are measured in the strong magnetic field $B_0^{\mathrm{PT}} \approx 4.023\,\mathrm{T}$ of the PT and therefore the probed levels are subject to the Zeeman effect. At this magnetic field, in addition to the linear Zeeman shift,

$$\Delta\nu_{\mathrm{ZE}}^{\mathrm{lin}} = \frac{1}{h} g_J^{(1)}(J)\, m_j \mu_{\mathrm{B}} B = a_J^{(1)}(m_j)\, B^i, \tag{5.11}$$

also the next high-order quadratic Zeeman shift has to be taken into account. The additional frequency shift $\Delta\nu_{\mathrm{ZE}}^{\mathrm{h.o.}}$ for the individual levels m_j of the $J = 1/2$ and $J = 3/2$ manifolds (fig. 5.1) due to the higher order Zeeman shift can be expressed as [214]:

$$\Delta\nu_{\mathrm{ZE}}^{\mathrm{h.o.}} = \frac{1}{h} \sum_{i=2}^{\infty} \frac{g_J^{(i)}(m_j)\, \mu_{\mathrm{B}}^i}{E_0^{i-1}} B^i = \sum_{i=2}^{\infty} a_J^{(i)}(m_j)\, B^i, \tag{5.12}$$

where $E_0 = m_{\mathrm{e}} c^2$ is the electron rest energy, $g_J^{(1)}$ is the Landé g-factor and $g_J^{(i\geq 2)}(m_j)$ are dimensionless constants depending on m_j. Values for the coefficients $a_J^{(i)}(m_j)$ and

$g_J^{(i)}(m_j)$ for the first three orders can be found in tab. 5.1. The contribution from the quadratic Zeeman effect at B_0^{PT} reaches values up to 2.1 MHz. This is on the level of the overall accuracy and therefore it must be included in the final evaluation.

Table 5.1.: Values of the coefficients of $a_J^{(i)}(m_j)$ and $g_J^{(i)}(m_j)$ for boronlike argon. The columns contain the values for the corresponding $|J, m_j\rangle$ states. The values are taken from [214], if not stated elsewise.

	$\lvert 3/2, \pm 3/2\rangle$	$\lvert 3/2, \pm 1/2\rangle$	$\lvert 1/2, \pm 1/2\rangle$
$g_J^{(1)}(J)$	1.332 282 5(14) [219]		0.663 648 455 32(93) [27]
$a_J^{(1)}(m_j)$ (GHz/T)	± 28.0	± 9.3	± 4.6
$g_J^{(2)}(m_j)$	0.95×10^3	41.0×10^3	-39.5×10^3
$a_J^{(2)}(m_j)$ (kHz/T^2)	1.5	65.0	-62.6
$g_J^{(3)}(m_j)$	$\mp 5.7 \times 10^3$	$\mp 2.5 \times 10^9$	$\pm 2.5 \times 10^9$
$a_J^{(3)}(m_j)$ (Hz/T^3)	$\mp 1.0 \times 10^{-6}$	∓ 0.45	± 0.45

5.8. Systematic Shifts and Uncertainties

Before determining the final value for the transition frequency of the fine structure transition from the obtained resonances, systematic effects that might shift the frequency have to be considered and corrected for. The effects are ordered by their relative contribution on the systematic error for the determination of the transition frequency, starting with the most dominant one.

5.8.1. Absolute Laser Frequency Determination

In order to determine the absolute spectroscopy laser frequency, a wavemeter is used and a HeNe laser locked to a transition in iodine at around 633 nm serves as absolute frequency standard (see sec. 3.5.2). During one measurement which lasts 24 h to 62 h, the wavemeter is re-calibrated typically every 3 h. The comparison of the measured frequencies before and after the re-calibration show deviation of the size of the measurement resolution of the wavemeter of 200 kHz in agreement with zero. The Ti:sapphire laser with a wavelength of around 882 nm is then referenced and stabilized by this wavemeter. The absolute accuracy specified by the manufacturer for such a combination of calibration and measurement wavelengths is ± 10 MHz [187]. Reference measurements of other wavemeters, identical in desgin, against a frequency comb done in the collaborating group of Prof. Nörtershäuser [220] show that this estimate is assumed to be conservative. To this end, at the beginning and at the end of the measurement campaign which lasted five months, the HeNe laser and the wavemeter are brought to the Institut für Kernphysik in Darmstadt, Germany. There, the absolute calibration of the

wavemeter by the HeNe laser is compared against a GPS-referenced frequency comb (Menlo Systems, FC1500-250-WG) at a calibration frequency ν_{cal}, which corresponds to the Zeeman shifted frequency at the magnetic field strength B_0^{PT}. These measurements are shown in fig. 5.5. The frequency calibrations done at different times before (July

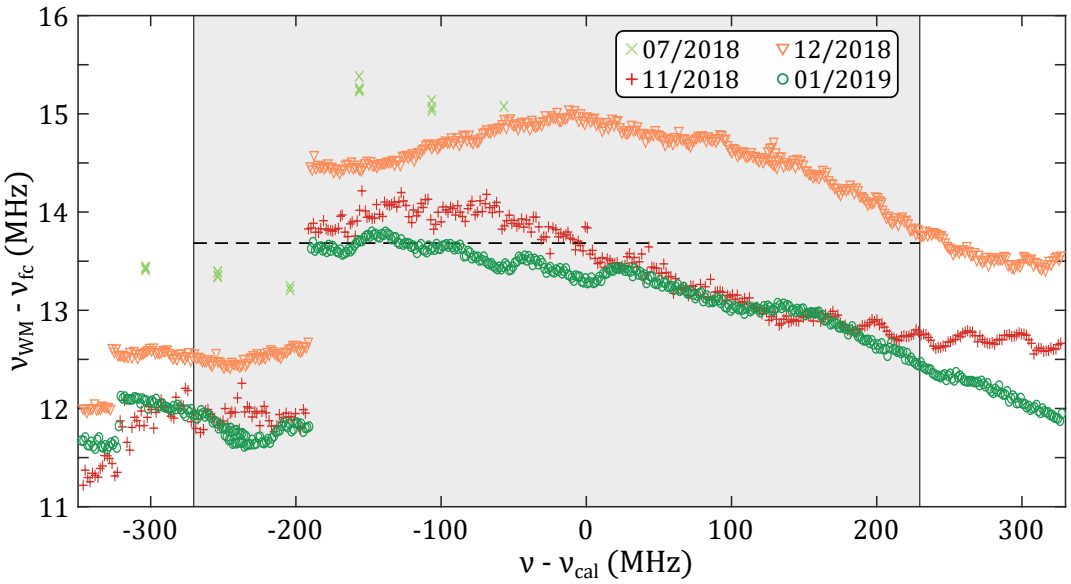

Figure 5.5.: Measured deviation between the frequencies as measured by the wavemeter ν_{WM} and the frequency comb ν_{fc}. The offset between the wavemeter and the frequency comb can either be corrected in the software of the wavemeter or as done here in the analysis afterwards. Shown are different measurements done before and after the measurement campaign. The gray shaded area is the frequency range used for the investigation of the transition ν_1. The dashed line is the mean value for all four measurements. For details see text.

2018) and after the campaign (November 2018 - January 2019) deviate from each other by $<2\,$MHz. Even though the maximum absolute deviation of every single measurement to the mean of all calibrations (dashed line) is $<2.1\,$MHz, as a conservative estimation the largest minimal-maximal difference of 2.6 MHz which occurs in a single measurement (December 2018) was taken as uncertainty. This confirms an absolute frequency repeatability of better than 2.6 MHz in the investigated wavelength regions around $\nu_{1,2}$, measured with the wavelength meter at 882 nm. In the same way also the frequency calibration around the investigated frequency for ν_2 is done, showing a similar behavior. Therefore the absolute accuracy of the determination of the laser frequency constitutes the dominant relative contribution on the systematic error of

$$\frac{\delta\nu_0}{\nu_0} < 7.7\times10^{-9}. \tag{5.13}$$

5.8.2. Magnetic Field Stability

From tab. 5.1, a sensitivity of the transition $\nu_{1,2}$ of 13.97 GHz/T due to the dominant linear Zeeman effect can be estimated. The typically observed stability for the magnetic field B_0^{PT} yields a modified Allan deviation of $<2\times10^{-8}$ on averaging timescales of 3 min to 7 h [84]. In addition, the stability of the magnetic field is observed to be better than $< 1.3\times10^{-7}$ during the whole measurement campaign of five months. This results in a systematic uncertainty due to the magnetic field stability on a level of

$$\frac{\delta\nu_0}{\nu_0} < 4\times10^{-11}, \tag{5.14}$$

which is below the overall systematic and statistical uncertainty. The magnetic field has been determined before and after each measurement by sideband coupling of the radial modes to the axial mode.

5.8.3. Second-Order Doppler Shift

As mentioned in sec. 2.7.3 and 5.3, the resonance profile will be broadened by the first order Doppler effect due to the finite axial temperature respectively axial energy of the ion. In addition to the broadening, also a shift of the resonance is caused by the second-order Doppler effect [134, 221]. Whereas in the equation for the momentum conservation, eq. (2.57a), only the linear frequency shift was considered for simplicity, the full expression for the resonant absorption condition reads:

$$\omega = \omega_0 + k_z v_z - \frac{1}{2}\omega_0\frac{|\vec{v}|^2}{c^2} + \frac{(\hbar k_z)^2}{2m\hbar}. \tag{5.15}$$

The second term and the third term on the right-hand side correspond to the linear and quadratic Doppler shift and the last term causes a shift due to the recoil energy $R = (\hbar k_z)^2/2m$. The second order shift is independent of the direction and therefore also the radial velocity components have to be considered. Because the the axial and cyclotron mode were sideband coupled at the beginning of the measurement, the kinetic energy $\langle E_{\mathrm{k}}\rangle$ is dominated by the cyclotron energy E_+, cf. eq. (2.10) and eq. (2.40):

$$\Delta\omega_{\mathrm{s.o.D.}} = -\frac{1}{2}\omega_0\frac{|\vec{v}|^2}{c^2} = -\omega_0\frac{\langle E_{\mathrm{k}}\rangle}{mc^2} \simeq -\omega_0\frac{\langle E_{\mathrm{k},+}\rangle}{mc^2} \overset{(2.40)}{\underset{(2.50)}{=}} -\omega_0\frac{k_{\mathrm{B}}T_z}{mc^2}\frac{\omega_+}{\omega_z} \tag{5.16}$$

This shift for the $^{40}\mathrm{Ar}^{13+}$ ion at $T_z = 19.5\,\mathrm{K}$ can be calculated to be 950 Hz and thus yields to a fractional shift of:

$$\frac{\Delta\nu_0}{\nu_0} < 1.4\times10^{-12}. \tag{5.17}$$

Therefore the second order Doppler shift can be neglected at the current level of precision.

5.8.4. Residual Magnetic Field Inhomogeneities

Because the transition frequency is measured in a magnetic field and later on corrected to a value in a zero magnetic field, also residual magnetic inhomogeneities constitute a source of systematic uncertainties. For the axial oscillation of the ion in a linear gradient of the magnetic field $B_1^{\mathrm{PT}}(z)$, the shift caused by this changing magnetic field and thus the Zeeman shift will average to zero for one oscillation period. However, this is not the case for a quadratic inhomogeneity $B_2^{\mathrm{PT}}(z^2)$. Averaged over one period the ion will sample a magnetic field $B \neq B_0^{\mathrm{PT}}$ [83]:

$$\frac{\Delta B}{B_0^{\mathrm{PT}}} \simeq \frac{B_2^{\mathrm{PT}}}{B_0^{\mathrm{PT}}} \rho_{\mathrm{th},z}^2. \tag{5.18}$$

Using eq. (2.52) and $B_2^{\mathrm{PT}} = 0.0643(32)\,\mathrm{T/m^2}$ [9] this systematic shift due to a residual quadratic magnetic field inhomogeneity for an ion temperature of $T_z = 19.5\,\mathrm{K}$ amounts to:

$$\frac{\Delta\nu_0}{\nu_0} < 3\times10^{-15}. \tag{5.19}$$

All systematic frequency shifts and relative systematic uncertainties for the determination of the transition frequency taken into account are summarized in table 5.2.

Table 5.2.: Summary of the relative contributions of individual effects on the systematic error for the determination of the transition frequency.

effect	$\delta\nu_0/\nu_0$
Absolute laser frequency determination	$< 7.7\times10^{-9}$
Magnetic field stability, B_0^{PT}	$< \quad 4\times10^{-11}$
Second-order Doppler shift	$< 1.4\times10^{-12}$
Residual magnetic field inhomogeneities, B_2^{PT}	$< \quad 3\times10^{-15}$
Total	$\leq 7.7\times10^{-9}$

5.9. Final Results

5.9.1. Maximum-Likelihood Routine

For recording one resonance, the interrogation frequency used in each cycle is taken from a predefined and randomly shuffled set of frequencies. Each frequency is probed multiple times and a spin state transition rate can be estimated from the ratio of successfully induced spin state transitions over the number of attempts. For each frequency the spin state transition rate at each frequency is determined by a maximum-likelihood estimate (MLE) of the probability of success for the independent trials to induce a spin flip [222].

As a consequence the error assigned to each spin state transition rate is asymmetric especially for a low number of attempts at each frequency, see fig. 5.6. Whereas the fitting of the resonance lineshape to the data using a nonlinear regression with a least square method assumes the error of the individual data points to be normally distributed, the MLE does not [83]. For a given set of data points, the MLE tries to find the set of parameters which maximizes the known likelihood distribution. For n attempted spin state transitions at a frequency ν, the probability p to observe k successful events is $p = f(\nu)^k \left(1 - f(\nu)\right)^{n-k}$. Here f is the function that describes the expected lineshape model (see sec. 5.3). In the case here it is a Gaussian function with free parameters for the center μ, width σ and amplitude α [40]:

$$f(\nu|\mu, \sigma, \alpha) = \alpha \exp\left(-\frac{(\nu - \mu)^2}{2\sigma^2}\right) \tag{5.20}$$

The likelihood function L is then given by the product of the uncorrelated probabilities of the full set of all individual data points i:

$$L = \prod_i p_i = \prod_i f(\nu)^{k_i} \left(1 - f(\nu)\right)^{1-k_i}, \tag{5.21}$$

where $k_i = 1$ for a successful spin state transition and $k_i = 0$ for a non-successful attempt of a spin state transition. The most probable set of parameter $(\nu_0, \sigma_0, \alpha_0)$ which lead to the observed results will also maximize the likelihood function L. An easier way of finding the maximum of L than by its derivative, is to maximize the logarithm of L, the log-likelihood function $\mathcal{L}$:

$$\mathcal{L} = \ln(L) = \sum_i \ln(p_i). \tag{5.22}$$

This simplifies the numerical calculation of the set of parameters $(\nu_0, \sigma_0, \alpha_0)$ that maximizes $\mathcal{L}$.

5.9.2. Resonances at Different Temperatures

In a span of two months 13 resonances are recorded with different parameters such as laser power, interrogation times, interrogation at a fixed frequency or with frequency sweeps ± 7 MHz around a center frequency. The laser power however can only be given as an upper estimate, since for the irradiation the linear polarized laser light was coupled into the Penning trap using a non-polarization-maintaining fiber and no polarization adjustment afterwards. The laser power is monitored during the measurements by measuring the light leaking through the dichroic mirror used on the optical breadboard. The intensity at the position of the ion, assuming it to be in the center of a Gaussian beam is estimated from the measured reflection and transmission of the dichroic mirror, the reflectivity of the last mirror and the transmission of the two view port windows inside the cryostat, see fig. 3.5. Due to the design of the ALPHATRAP setup there is no possibility to measure the actual power at the the center of the PT or to exclude clipping or internal reflections of the laser beam in situ. The estimated laser intensities

are $20\,\mu W/mm^2$ to $50\,\mu W/mm^2$, which is limited by the overall energy deposited into the trap, which is observed to cause unwanted frequency shifts and change in trapping potentials. The saturation intensity of the transition is $0.75\,nW\,mm^{-2}$ [214], but the transition is only driven by a small fraction given by the ratio of the natural linewidth and the laser linewidth.

The frequency sweeps are used to avoid the case that the laser irradiation is done at a frequency right in between two sidebands spaced by $\nu_z^{PT} = 650\,kHz$ (see fig. 5.2), since the laser linewidth is on the order of $< 100\ kHz_{rms}/100\,ms$ and the stabilization system used for controlling the reference cavity is limited on the low frequency end by the measurement resolution of the wavelength meter of 200 kHz[4]. However, no differences for resonances taken with interrogation at fixed or swept frequencies are observed.

In order to investigate systematic effects on determination of the center frequency of the acquired resonances, such as possible amplitude dependent frequency shifts not considered in sec. 5.8, different measurement settings are used. The strongest effect on the resonances have the axial energy $\langle E_z \rangle$ respectively axial temperature T_z which is changed either by using electronic negative feedback, sec. 2.7.2, or adiabatic cooling, sec. 2.7.1. Adiabatic cooling can be applied here in this unique measurement scheme, since during the interrogation of the ion with the laser, measuring the axial frequency is not of importance[5]. Therefore the initially thermalized ion can be fully decoupled from the axial resonator, being supposedly most unperturbed. For this the trapping voltage was decreased by a factor of $\xi = 15$ (cf. sec. 2.7.1). Furthermore it is demonstrated that the adiabatic cooling can be combined with a previous negative feedback, which leads to the narrowest measured resonance at a derived temperature of 1.0(3) K, a factor of almost 20 lower than with the resistive cooling from the resonator only, see fig. 5.6. Also shown there are resonances taken with the resistive cooling by the axial resonator only and with adiabatic cooling. An overview of the determined centers of the resonances is shown in fig. 5.7. Even though the resonances acquired without the negative feedback cooling technique (red resonances in figs. 5.6 and 5.7) appear to be shifted to lower frequencies, this is statistically nonsignificant. It is not assumed to be related to the temperature of the ion during the measurements and also every single measurement is in good agreement with the mean of all resonances. The largest deviation from the weighted mean is 1.8σ for resonance #1, all others deviate less. There is a good agreement between the resonances taken for transition ν_1 (#1-#9) and ν_2 (#10-#13). Furthermore there is good agreement between the values taken at the lowest temperatures (#11-#13) for which the absolute uncertainties are the smallest. The measurements done with the adiabatic cooling for which the ion is fully decoupled from the resonator show good agreement with each other and the weighted mean.

In both figures the center of the resonances is referenced to the overall final result for

[4] Since this is measured at 882 nm it corresponds to 400 kHz at 441 nm.

[5] This is not the case in "traditional" g-factor measurement in which during the millimeter wave interrogation for the Larmor frequency, the cyclotron frequency needs to be measured simultaneously via a cyclotron sideband coupling.

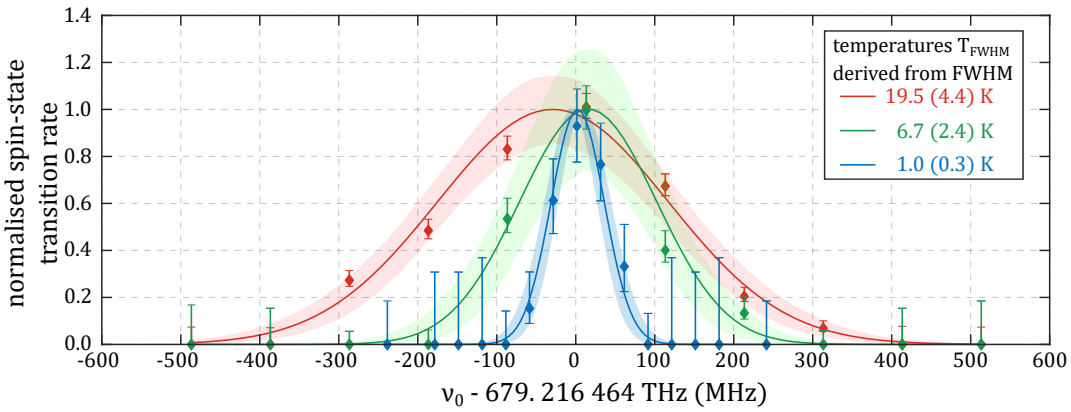

Figure 5.6.: Typical resonances for different axial temperatures achieved by using different cooling techniques. The corresponding temperatures are derived from the fitted FWHM according to eq. (5.7). The resonance in red is recorded with the resistive cooling of the PT axial resonator only. The resonance in green is acquired using adiabatic cooling and the blue one is for a combined cooling with negative electronic feedback and adiabatic cooling. The error bars are the maximum likelihood estimates for binomial attempts for obtaining a spin state transition at the respective frequency. The fit (solid line) is a Gaussian lineshape fitted by the MLE routine. The shaded areas are the 68 %-confidence band of the fit. The data shown are resonance #8, #9 and #12 of fig. 5.7. The figure is modified from [71].

the transition ν_0 at zero magnetic field for the fine structure $2p\,^2P_{1/2} \leftrightarrow {}^2P_{3/2}$ state:

$$\nu_0 = 679.216\,464\,(4)_{\text{stat}}\,(5)_{\text{sys}}\,\text{THz} \tag{5.23}$$

The systematic error is composed of the contributions listed in tab. 5.2 and the statistical error is the error of the mean of the found resonance centers weighted by their individual errors, see fig. 5.7. Before the magnetic field corrections including the second order Zeeman effect, the individual transitions ν_1 between the states $|J, m_j\rangle = |1/2, -1/2\rangle \leftrightarrow |3/2, +1/2\rangle$ and ν_2 for $|1/2, +1/2\rangle \leftrightarrow |3/2, -1/2\rangle$ are:

$$\nu_1 = 679.272\,651\,(7)_{\text{stat}}\,(5)_{\text{sys}}\,\text{THz}, \tag{5.24a}$$

$$\nu_2 = 679.160\,272\,(5)_{\text{stat}}\,(5)_{\text{sys}}\,\text{THz}. \tag{5.24b}$$

5.9.3. The Excited State *g*-factor

Because both transitions ν_1 and ν_2 are measured, above results can be combined and allow to extract a value for the excited state g-factor $g^{(1)}_{3/2}$ using the known value for the

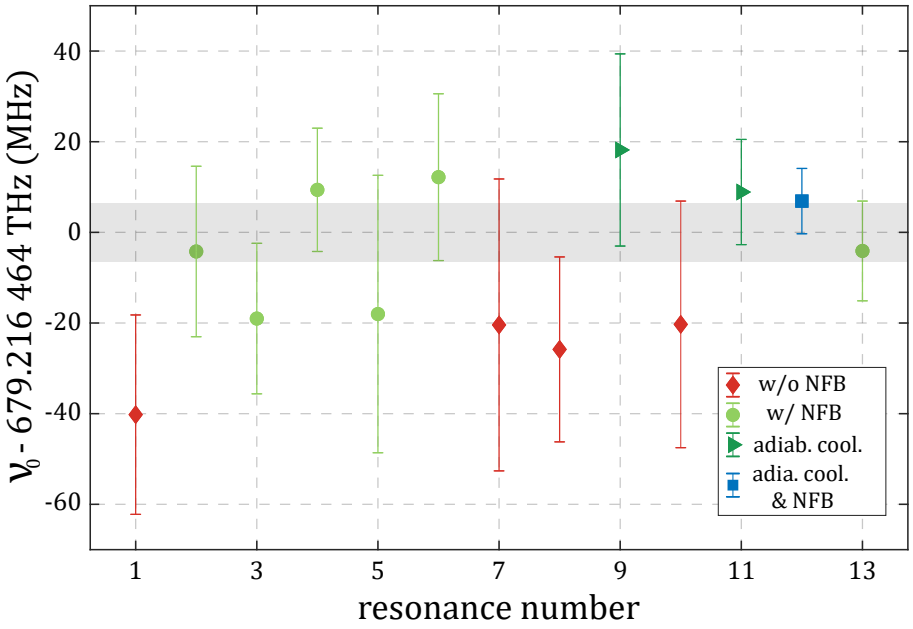

Figure 5.7.: Centers of resonances taken with different cooling methods. Resonances #1 to #9 are recorded with transition ν_1, whereas resonances 10 to 13 correspond to transition ν_2, see fig. 5.1. Both transitions are corrected for the magnetic field induced Zeeman shift including also the second order. The shaded area represents the combined systematic and statistical error. Figure modified from [71].

ground-state g-factor $g^{(1)}_{1/2}$ [27]. This way the following value can be derived:

$$g^{(1)}_{3/2} = 1.332\ 14(15). \tag{5.25}$$

This value is in in agreement with the theoretically calculated value [219] of $g^{(1)}_{3/2} = 1.332\ 282\ 5(14)$.

5.10. Comparison to Previous Literature Values

Whereas the main objective of this measurement is a demonstration of the detection method using the CSGE, it improves the existing value for the fine structure transition in $^{40}Ar^{13+}$ by more than one order of magnitude, namely by a factor of 24.

For the fine structure transition between the $^2P_{1/2}$ and $^2P_{3/2}$ levels in $^{40}Ar^{13+}$ several measurements and theoretical predictions can be found. The most recent and precise values are measured in an EBIT [223–225], see fig. 5.8. There the ions are stored as a cloud of interacting ions in a potential depth of typically a few eV, which gives the ions a kinetic energy in the kK to MK regime. Common to this approach based on

the detection of fluorescence is the low photon yield coming from the HCI. The high temperatures of the ions do not allow a high precision due to Doppler broadening and are the main limitation of these measurements.

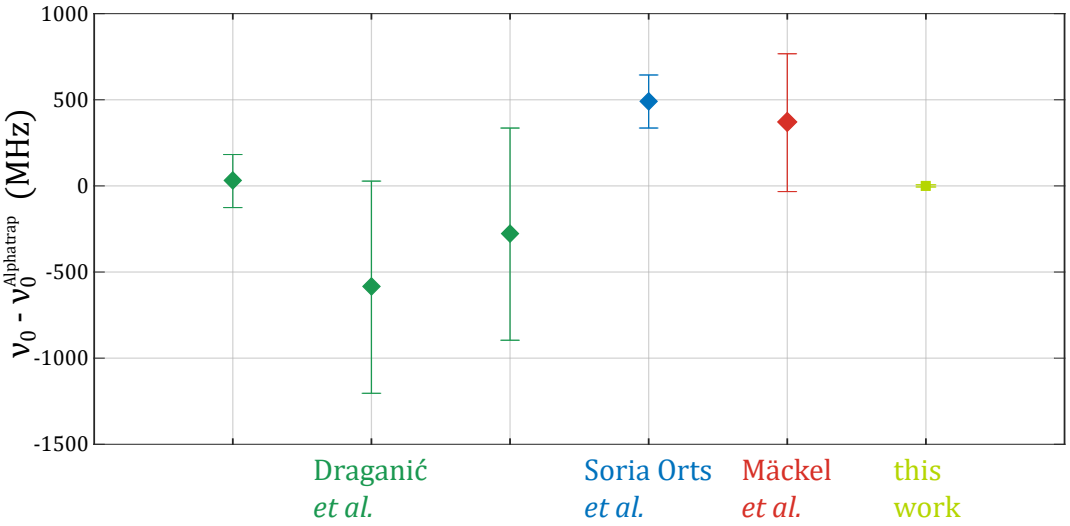

Figure 5.8.: Comparison of the final value for ν_0 to the most recent and precise literature values. The corresponding references are [223–225] and [71].

The result of this work is in good agreement with the four values given in [223, 225]. However, there is a deviation of 3.2σ to lower frequency compared to [224], which is listed as the current value for this transition in atomic spectra database of NIST [196]. Comparison of the value of this work to the weighted mean of all five values [223–225] does not show a deviation with statistical significance (2.2σ). Furthermore, the value is in good agreement with theoretical calculations for the transition frequency [226].

6. Conclusion and Outlook

Having successfully set up [69, 84, 164, 165, 168, 171, 173, 194] and commissioned [9, 84] the ALPHATRAP experiment, the first results from HCI measurements were obtained and published [9, 27, 71].

In the scope of this thesis laser systems for different purposes have been implemented into the ALPHATRAP experiment. Even though lasers both for spectroscopy and laser cooling of trapped charged particles in a Penning trap are commonly used, it was new ground to implement these techniques not only at ALPHATRAP and but also within our division on *Stored and Cooled Ions* [227] to gain first experience first-hand. At the time this PhD started, the Doppler cooling laser system was just about to be purchased and the floor plan for the laser laboratory behind the ALPHATRAP magnet room was outlined. Having joined ALPHATRAP at this stage of the experiment and accompany the experiment from the first steps of setting up the infrastructure for a laser laboratory to the publication of a novel spectroscopy technique was a great journey.

Both techniques, the laser spectroscopy and laser cooling, pave the way for a plethora of new intriguing future experiments and measurements at ALPHATRAP. In this thesis two main contributions towards these goals have been presented.

6.1. Laser Cooling of $^9Be^+$

Laser cooling of the axial mode of a single $^9Be^+$ ion was demonstrated. To this end, beryllium ions from the external laser ablation source [168] are injected into the Penning-trap tower for the first time and a single ion is prepared in a dedicated beryllium trap. In order to determine the ion temperature an already established technique was adapted to the case here, in which the ion is not in thermal equilibrium with the detection circuit. The obtained measurements give an upper estimate of the achieved axial temperature of

$$T_z = 69(30)\,\mathrm{mK}. \tag{6.1}$$

During these measurements technical limitations were identified, which triggered upgrades at the ALPHATRAP apparatus that are already under development or in the process of being implemented.

A substantial issue is the negative influence of the laser beam onto the stability and reproducibility of the trapping potentials, which are required for high-precision measurements. In order to mitigate this effect, a separate cooling trap, located off-center and next to the trap tower containing the PT and AT is currently under development [193]. This new cooling trap will also be optimized for the detection and control of $^9Be^+$ ions. In order to then couple the laser cooled beryllium ions and the HCI under investigation,

a novel scheme is under development [193, 211]. It uses the resonator detection circuit to mediate the interaction between the laser cooled beryllium ion and the HCI, allowing sympathetic cooling of the HCI. Furthermore the pointing stability of the laser beam is improved by an active stabilization system that is currently being installed [193].

Once these new ideas together with a to be improved magnetic field stability are implemented, the targeted level of relative precision of $\leq 10^{-11}$ for g-factor measurements might be in reach, since systematic amplitude-dependent frequency shifts will be reduced significantly by the sympathetic cooling. Furthermore, an unambiguous detection of spin state transitions in heavy HCI via the continuous Stern-Gerlach effect in the analysis trap is facilitated by a reduced amplitude in the radial modes. Fluctuations in the cyclotron energy E_+, following a corresponding thermal Boltzmann distribution can cause frequency shifts in the strong magnetic bottle of the AT, mimicking frequency changes due to spin-state transitions. In addition, the phase-sensitive technique PnA [70], which will be used for the determination of the ions motional frequencies [88], will benefit from a lower initial temperature of the ion.

Also the relative uncertainty of future laser spectroscopy experiments will be decreased by using sympathetic laser cooling. A reduced motional amplitude of the ion under investigation (see sec. 6.3 and 6.4) results in a significant improvement of the achievable precision due to a reduced Doppler broadening.

6.2. Laser Spectroscopy of the $^{40}Ar^{13+}$ Fine Structure

In addition to the laser cooling of beryllium ions, in the course of this thesis a proof-of-principle measurement of a novel laser spectroscopy technique was successfully demonstrated [71]. By using the continuous Stern-Gerlach effect (CSGE), high-precision laser spectroscopy of an electric dipole forbidden long-lived transition in $^{40}Ar^{13+}$ was accomplished. The final value for the transition ν_0 between the $2p\,^2P_{1/2} \leftrightarrow {}^2P_{3/2}$ fine structure states at zero magnetic field was obtained:

$$\nu_0 = 679.216\,464\,(4)_{\mathrm{stat}}\,(5)_{\mathrm{sys}}\,\mathrm{THz}. \tag{6.2}$$

The value is in agreement with the current best literature values and with a fractional uncertainty of 9.4×10^{-9} it improves the previous best value by a factor of 24. Most importantly, this method does not rely on fluorescence detection which makes it very appealing for investigations of long-lived forbidden transitions which can often be found in HCI [42, 228]. In multielectron HCI, dissimilar electron configurations with almost degenerate energies can be found, which give rise to transitions in the optical regime. If those transitions also have different projection values of the overall magnetic moment of the ion, they can be detected with the herein presented method. Because the method is based on a pumping mechanism into a long lived dark state, it allows the search for and the identification of transitions not known a priori with sufficient precision.

At Alphatrap arbitrary HCIs can be stored and cooled for virtually an indefinite time span. This allows to either precisely determine the frequency of those transitions

that could serve as valuable starting points for other experiments [229] or directly measure the transition with similar precision at ALPHATRAP. The achievable uncertainty, dominated by the first order Doppler effect can be further reduced by the implementation of the aforementioned sympathetic laser cooling of the HCI. For future experiments at ALPHATRAP two candidates can be identified with different physics cases as motivation:

6.3. Lithium- and Hydrogenlike Bismuth $^{209}\mathrm{Bi}^{80+,82+}$

A first interesting candidate for spectroscopy on HCIs is the hyperfine splitting of the ground state in lithium- and hydrogenlike bismuth, $^{209}\mathrm{Bi}^{80+,82+}$. In lithium- and hydrogenlike ions many laser accessible HFS transitions can be found [12]. However, bismuth is the only system in which the HFS transition for both the lithium- and hydrogenlike charge state are laser accessible (243 nm respectively 1554 nm [67]). This enables a test of QED calculations in strong electric and magnetic fields[1]. The most precise experimental values of these two transitions have relative uncertainties of 1.8×10^{-5} (243 nm) respectively 1.9×10^{-5} (1554 nm) [67] and are limited by the high energy of the HCIs, as they are measured either in storage rings [66, 67, 230, 231] or EBITs [232]. Assuming $^{209}\mathrm{Bi}^{80+,82+}$ ions can be injected into ALPHATRAP and resistively cooled to $\approx$4 K, already the width of the transition due to the first order Doppler effect would be a factor of roughly 200 smaller than the uncertainty of the measurement in [67]. Therefore a determination of the transition frequency by fractions of the Doppler broadenend linewidth would improve the relative precision by two to three orders of magnitude. A frequency determination down to the natural linewidth $\Gamma=\frac{1}{2\pi\tau}$ ($\Gamma(^{209}\mathrm{Bi}^{80+}) \simeq 1.5$ Hz respectively $\Gamma(^{209}\mathrm{Bi}^{82+}) \simeq 286$ Hz [233]) would improve the relative precision by another five to seven orders of magnitude[2] and allows direct measurement of the nuclear magnetic moments.

6.4. Molecular Hydrogen Ion H_2^+

Another promising candidate for the application of this spectroscopy method is the molecular hydrogen ion, H_2^+. Precision spectroscopy of the rovibrational levels of molecular hydrogen ions [234, 235] give access to fundamental constants, e.g. the electron-to-proton mass ratio, $m\,(\mathrm{e}^-)\,/m\,(\mathrm{p})$. As proposed in [236], the rovibrational HFS spectroscopy of the molecular hydrogen ion H_2^+ and its antimatter counterpart $\bar{\mathrm{H}}_2^-$ can be used as a direct test of the CPT-theorem[3]. Using single trapped molecular ions allow virtually indefinite storage times, which is especially useful considering the necessary effort to produce $\bar{\mathrm{H}}_2^-$.

The electronic states $|\nu, N\rangle$ of H_2^+ are described by their vibrational quantum number ν and rotational quantum number N. The total nuclear spin I of the molecule can either

[1] For hydrogenlike bismuth $^{209}\mathrm{Bi}^{82+}$ the expectation value for the electric field in the $1S_{1/2}$ orbital is as high as $<1.1\times10^{16}$ V/cm and for the magnetic field in the order of 1×10^4 T [10].

[2] Assuming to have a full understanding and control of all systematic effects.

[3] Transformation of the physical laws under simultaneous charge conjugation (C), parity transformation (P) and time reversal (T).

be $I=0$ for para-hydrogen ($N=$even) or $I=1$ for ortho-hydrogen ($N=$odd). Transitions between para- and ortho-hydrogen are not allowed ($\Delta N \neq \pm 1$) and also the rovibrational levels mainly decay via electric quadrupole transitions (E2, $\Delta N = 0, 2$). This results in very long lifetimes which makes fluorescence based spectroscopic measurements of rovibrational transition frequencies a challenging task.

In the strong magnetic field of a Penning trap, the overall level structure is given by the projection value of the magnetic moment from the electron spin (m_s), nuclear spin (m_I) and the angular momentum of the rotation (m_N). The Zeeman splitting[4] is dominated by the electron magnetic moment (m_s). The frequency difference $\Delta f(\nu, N, m_\mathrm{N}; B)$ between different HFS states ($N \neq 0$) depends on ν, N and m_N and can be calculated [237] as well as experimentally resolved. Using the continuous Stern-Gerlach effect, individual rovibrational and Zeeman-hyperfine states can be identified. According to eq. (2.48), the axial frequency difference $\Delta\nu_z$ for H_2^+ caused by a spin state transition of the electron $|m_\mathrm{s} = -1/2\rangle \leftrightarrow |+1/2\rangle$ in the AT of ALPHATRAP amounts to 19 Hz.

This allows to perform laser optical microwave double resonance measurements of the rovibrational levels. The procedure is very similar to the fine structure spectroscopy of $^{40}Ar^{13+}$ (sec. 5). Starting from an initial rovibrational state, the H_2^+ ion is prepared in a specific spin state (e.g. $|\nu, N, m_\mathrm{s}\rangle = |0, 2, +1/2\rangle$) using the CSGE. Then the transition frequency f of an electric dipole forbidden long lived vibrational transition ($\Delta\nu = 1$) to $|1, 2, +1/2\rangle$ is probed ($f \simeq 65.7$ THz and corresponds to a wavelength of 4.6 µm). The success rate for the vibrational excitation as function of the probed frequency f can be determined, using again the CSGE. Because the Larmor frequency between the two Zeeman manifolds $|\nu, N, +1/2\rangle \leftrightarrow |\nu, N, -1/2\rangle$ is dependent on ν and N, checking for spin state transitions in either the excited state $|1, 2, +1/2\rangle \leftrightarrow |1, 2, -1/2\rangle$ or the initial state $|0, 2, +1/2\rangle \leftrightarrow |0, 2, -1/2\rangle$ reveal the vibrational state of the ion. In this way the resonance of the vibrational transition can be recorded.

All together the results presented in the second part of this thesis constitute a proof-of-principle demonstration for this spectroscopy technique and opens up very promising and interesting perspectives for the future.

[4] Similar as in hydrogenlike ions, the Zeeman splitting depends on the g_e-factor of the bound electron, $g_\mathrm{e}(\nu, N) \simeq 2$ and amounts to $\nu_\mathrm{L} \simeq 112$ GHz in ALPHATRAP.

List of Publications

1. S. Sturm, I. Arapoglou, **A. Egl**, M. Höcker, S. Kraemer, T. Sailer, B. Tu, A. Weigel, R. Wolf, J. R. Crespo López-Urrutia, and K. Blaum. The ALPHATRAP experiment, *The European Physical Journal Special Topics*, 227(13), 1425-1491, 2019.

   Note: cited as [9].

2. P. Micke, S. Kühn, L. Buchauer, J. R. Harries, T. M. Bücking, K. Blaum, A. Cieluch, **A. Egl,** D. Hollain, S. Kraemer, T. Pfeifer, P. O. Schmidt, R. X. Schüssler, Ch. Schweiger, T. Stöhlker, S. Sturm, R. N. Wolf, S. Bernitt, and J. R. Crespo López-Urrutia. The Heidelberg compact electron beam ion traps, *Review of Scientific Instruments*, 89, 063109, 2018.

   Note: cited as [162].

3. I. Arapoglou, **A. Egl**, M. Höcker, T. Sailer, B. Tu, A. Weigel, R. Wolf, H. Cakir, V. A. Yerokhin, N. S. Oreshkina, V. A. Agababaev, A. V. Volotka, D. V. Zinenko, D. A. Glazov, Z. Harman, C. H. Keitel, S. Sturm and K. Blaum, g Factor of Boronlike Argon $^{40}Ar^{13+}$, *Phys. Rev. Lett.*, 122:253001, 2019.

   Note: cited as [27].

4. **A. Egl**, I. Arapoglou, M. Höcker, K. König, T. Ratajczyk, T. Sailer, B. Tu, A. Weigel, W. Nörtershäuser, K. Blaum and S. Sturm, Application of the continuous Stern-Gerlach effect for laser spectroscopy of the $^{40}Ar^{13+}$ fine structure in a Penning trap, *Phys. Rev. Lett.*, 123:123001, 2019.

   Note: Results of chapter 5 and cited as [71].

A. Appendix

A.1. Typical Trap Parameters of ALPHATRAP

The trap parameters for the ALPHATRAP Penning trap setup can be found in detail in the theses of Andreas Weigel [84] and Ioanna Arapoglou [40] as well as in the ALPHATRAP overview review paper [9]. Some of the most important parameters are summarized in the following table. The magnetic fields in the PT and AT are $B_0^{\mathrm{PT}} \simeq 4.02\,\mathrm{T}$ and $B_0^{\mathrm{AT}} \simeq 3.8\,\mathrm{T}$ and $B_2^{\mathrm{AT}} \simeq 44\,\mathrm{kT/m^2}$. The axial resonators of the PT has a resonance frequency $\omega_{\mathrm{res}}^{\mathrm{PT}} = 2\pi \cdot 650\,\mathrm{kHz}$ and the one of the AT has a resonance frequency $\omega_{\mathrm{res}}^{\mathrm{AT}} = 2\pi \cdot 335\,\mathrm{kHz}$.

Table A.1.: Typical trap parameters for ALPHATRAP for an $^{40}Ar^{13+}/^{9}Be^{+}$ ion. Here both are assumed to have a temperature of 4.2 K. For the calculated quantities, the used relation is giving in the corresponding line. For the derivation the radial modes are assumed to be thermalized to the axial mode.

	axial mode, $i=z$	modified cyclotron mode, $i=+$	magnetron mode, $i=-$
frequency, eq. (2.7)			
frequency ν_i^{PT}	650 kHz/650 kHz	20.1 MHz/6.8 MHz	10.5 kHz/31.0 kHz
frequency ν_i^{AT}	335 kHz/335 kHz	19.0 MHz/6.5 MHz	3.0 kHz/8.7 kHz
dip width, eq. (2.35)			
$\Delta\nu_{\mathrm{dip}}^{\mathrm{PT}}$	4.1 Hz/0.1 Hz	n.a.	n.a.
$\Delta\nu_{\mathrm{dip}}^{\mathrm{AT}}$	4.4 Hz/0.1 Hz	n.a.	n.a.
$\Delta\nu_{\mathrm{dip}}^{\mathrm{BeT}}$	26 Hz/0.7 Hz	n.a.	n.a.
Temperature, eq. (2.53a)			
T_i^{PT}	4.2 K/4.2 K	130 K/44 K	−68 mK/−200 mK
thermal amplitude, eq. (2.52), (2.53b), $\rho_{i,\mathrm{th}}^{\mathrm{PT}}$	10.2 µm/21.6 µm	1.8 µm/6.7 µm	1.8 µm/6.7 µm
quantum number, eq. (2.11), $n_{z,+,-}$	134600/134600	134600/134600	134600/134600
Spinflip, eq. (2.48)	$^2P_{1/2}$ ground state $\lvert J, m_j\rangle = \lvert 1/2, -1/2\rangle \leftrightarrow \lvert 1/2, +1/2\rangle$		
$\Delta\nu_z^{\mathrm{AT}}$	307 mHz/n.a.	n.a.	n.a.

Bibliography

[1] M. Dine and A. Kusenko. Origin of the matter-antimatter asymmetry. *Rev. Mod. Phys.*, 76:1–30, 2003.

[2] Nobelprize.org. Hans G. Dehmelt – Biographical, 2019.

[3] D. Hanneke, S. Fogwell, and G. Gabrielse. New Measurement of the Electron Magnetic Moment and the Fine Structure Constant. *Phys. Rev. Lett.*, 100:120801, 2008.

[4] S. Sturm, A. Wagner, B. Schabinger, J. Zatorski, Z. Harman, W. Quint, G. Werth, C. H. Keitel, and K. Blaum. g Factor of Hydrogenlike $^{28}Si^{13+}$. *Phys. Rev. Lett.*, 107:023002, 2011.

[5] W. E. Lamb and R. C. Retherford. Fine Structure of the Hydrogen Atom by a Microwave Method. *Phys. Rev.*, 72:241–243, 1947.

[6] H. M. Foley and P. Kusch. On the Intrinsic Moment of the Electron. *Phys. Rev.*, 73:412–412, 1948.

[7] P. Kusch and H. M. Foley. The Magnetic Moment of the Electron. *Phys. Rev.*, 74: 250–263, 1948.

[8] P. A. M. Dirac. The Quantum Theory of the Electron. *Proceedings of the Royal Society of London. Series A, Containing Papers of a Mathematical and Physical Character*, 117(778):610–624, 1928.

[9] S. Sturm, I. Arapoglou, A. Egl, M. Höcker, S. Kraemer, T. Sailer, B. Tu, A. Weigel, R. Wolf, J. C. López-Urrutia, and K. Blaum. The ALPHATRAP experiment. *The European Physical Journal Special Topics*, 227(13):1425–1491, 2019.

[10] T. Beier. The g_j factor of a bound electron and the hyperfine structure splitting in hydrogenlike ions. *Physics Reports*, 339(2):79 – 213, 2000.

[11] S. K. Suslov. Expectation values in relativistic Coulomb problems. *Journal of Physics B: Atomic, Molecular and Optical Physics*, 42(18):185003, 2009.

[12] W. Quint and M. Vogel, editors. *Fundamental Physics in Particle Traps*. Springer Berlin Heidelberg, 2014.

[13] J. Schwinger. On Quantum-Electrodynamics and the Magnetic Moment of the Electron. *Phys. Rev.*, 73:416–417, 1948.

[14] T. Aoyama, M. Hayakawa, T. Kinoshita, and M. Nio. Quantum electrodynamics calculation of lepton anomalous magnetic moments: Numerical approach to the perturbation theory of QED. *Progress of Theoretical and Experimental Physics*, 2012(1), 2012.

[15] T. Aoyama, M. Hayakawa, T. Kinoshita, and M. Nio. Tenth-order electron anomalous magnetic moment: Contribution of diagrams without closed lepton loops. *Phys. Rev. D*, 91:033006, 2015.

[16] R. Bouchendira, P. Cladé, S. Guellati-Khélifa, F. m. c. Nez, and F. m. c. Biraben. New Determination of the Fine Structure Constant and Test of the Quantum Electrodynamics. *Phys. Rev. Lett.*, 106:080801, 2011.

[17] T. Aoyama, T. Kinoshita, and M. Nio. Revised and improved value of the QED tenth-order electron anomalous magnetic moment. *Phys. Rev. D*, 97:036001, 2018.

[18] R. H. Parker, C. Yu, W. Zhong, B. Estey, and H. Müller. Measurement of the fine-structure constant as a test of the Standard Model. *Science*, 360(6385):191–195, 2018.

[19] T. Aoyama, T. Kinoshita, and M. Nio. Theory of the Anomalous Magnetic Moment of the Electron. *Atoms*, 7(1), 2019.

[20] H. Häffner, T. Beier, N. Hermanspahn, H.-J. Kluge, W. Quint, S. Stahl, J. Verdú, and G. Werth. High-Accuracy Measurement of the Magnetic Moment Anomaly of the Electron Bound in Hydrogenlike Carbon. *Phys. Rev. Lett.*, 85:5308–5311, 2000.

[21] J. Verdú, S. Djekić, S. Stahl, T. Valenzuela, M. Vogel, G. Werth, T. Beier, H.-J. Kluge, and W. Quint. Electronic g Factor of Hydrogenlike Oxygen $^{16}O^{7+}$. *Physical review letters*, 92(9):093002, 2004.

[22] A. Wagner, S. Sturm, F. Köhler, D. A. Glazov, A. V. Volotka, G. Plunien, W. Quint, G. Werth, V. M. Shabaev, and K. Blaum. g Factor of Lithiumlike Silicon $^{28}Si^{11+}$. *Phys. Rev. Lett.*, 110:033003, 2013.

[23] F. Köhler, K. Blaum, M. Block, S. Chenmarev, S. Eliseev, D. A. Glazov, M. Goncharov, J. Hou, A. Kracke, D. A. Nesterenko, Y. N. Novikov, W. Quint, E. Minaya Ramirez, V. M. Shabaev, S. Sturm, A. V. Volotka, and G. Werth. Isotope dependence of the Zeeman effect in lithium-like calcium. *Nature communications*, 7:10246, 2016.

[24] D. A. Glazov, F. Köhler-Langes, A. V. Volotka, K. Blaum, F. Heiße, G. Plunien, W. Quint, S. Rau, V. M. Shabaev, S. Sturm, and G. Werth. g Factor of Lithiumlike Silicon: New Challenge to Bound-State QED. *Phys. Rev. Lett.*, 123:173001, 2019.

[25] F. Köhler. *Bound-Electron g-Factor Measurements for the Determination of the Electron Mass and Isotope Shifts in Highly Charged Ions.* PhD thesis, Ruprecht-Karls-Universität, Heidelberg, 2015.

[26] P. Indelicato. QED tests with highly charged ions. *Journal of Physics B: Atomic, Molecular and Optical Physics*, 52(23):232001, 2019.

[27] I. Arapoglou, A. Egl, M. Höcker, T. Sailer, B. Tu, A. Weigel, R. Wolf, H. Cakir, V. A. Yerokhin, N. S. Oreshkina, V. A. Agababaev, A. V. Volotka, D. V. Zinenko, D. A. Glazov, Z. Harman, C. H. Keitel, S. Sturm, and K. Blaum. g Factor of Boronlike Argon $^{40}Ar^{13+}$. *Phys. Rev. Lett.*, 122:253001, 2019.

[28] J. Schwinger. On Gauge Invariance and Vacuum Polarization. *Phys. Rev.*, 82: 664–679, 1951.

[29] V. Shabaev, A. Bondarev, D. Glazov, Y. Kozhedub, I. Maltsev, A. Malyshev, R. Popov, D. Tumakov, and I. Tupitsyn. QED with heavy ions: on the way from strong to supercritical fields. *arXiv preprint arXiv:1910.01373*, 2019.

[30] W. H. Furry. On Bound States and Scattering in Positron Theory. *Phys. Rev.*, 81:115–124, 1951.

[31] G. Breit. The magnetic moment of the electron. *Nature*, 122(3078):649–649, 1928.

[32] A. Czarnecki and R. Szafron. Light-by-light scattering in the Lamb shift and the bound electron g factor. *Phys. Rev. A*, 94:060501, 2016.

[33] A. Czarnecki, M. Dowling, J. Piclum, and R. Szafron. Two-Loop Binding Corrections to the Electron Gyromagnetic Factor. *Phys. Rev. Lett.*, 120:043203, 2018.

[34] V. M. Shabaev. QED theory of the nuclear recoil effect on the atomic g factor. *Phys. Rev. A*, 64:052104, 2001.

[35] I. Angeli and K. Marinova. Table of experimental nuclear ground state charge radii: An update. *Atomic Data and Nuclear Data Tables*, 99(1):69 – 95, 2013.

[36] J. Zatorski, N. S. Oreshkina, C. H. Keitel, and Z. Harman. Nuclear Shape Effect on the g Factor of Hydrogenlike Ions. *Phys. Rev. Lett.*, 108:063005, 2012.

[37] V. M. Shabaev, D. A. Glazov, N. S. Oreshkina, A. V. Volotka, G. Plunien, H.-J. Kluge, and W. Quint. g-Factor of Heavy Ions: A New Access to the Fine Structure Constant. *Phys. Rev. Lett.*, 96:253002, 2006.

[38] V. A. Yerokhin, E. Berseneva, Z. Harman, I. I. Tupitsyn, and C. H. Keitel. g Factor of Light Ions for an Improved Determination of the Fine-Structure Constant. *Phys. Rev. Lett.*, 116:100801, 2016.

[39] A. V. Volotka, D. A. Glazov, V. M. Shabaev, I. I. Tupitsyn, and G. Plunien. Many-Electron QED Corrections to the g Factor of Lithiumlike Ions. *Phys. Rev. Lett.*, 112:253004, 2014.

[40] I. Arapoglou. *First measurements of the ground-state g-factor of boronlike* $^{40}Ar^{13+}$ *in ALPHATRAP*. PhD thesis, Ruprecht-Karls-Universität, Heidelberg, 2019.

[41] S. Sturm, F. Köhler, J. Zatorski, A. Wagner, Z. Harman, G. Werth, W. Quint, C. H. Keitel, and K. Blaum. High-precision measurement of the atomic mass of the electron. *Nature*, 506(7489):467, 2014.

[42] M. G. Kozlov, M. S. Safronova, J. R. Crespo López-Urrutia, and P. O. Schmidt. Highly charged ions: Optical clocks and applications in fundamental physics. *Rev. Mod. Phys.*, 90:045005, 2018.

[43] J. C. Berengut, V. A. Dzuba, and V. V. Flambaum. Enhanced Laboratory Sensitivity to Variation of the Fine-Structure Constant using Highly Charged Ions. *Phys. Rev. Lett.*, 105:120801, 2010.

[44] S. Schiller. Hydrogenlike Highly Charged Ions for Tests of the Time Independence of Fundamental Constants. *Phys. Rev. Lett.*, 98:180801, 2007.

[45] T. Dent, S. Stern, and C. Wetterich. Unifying cosmological and recent time variations of fundamental couplings. *Phys. Rev. D*, 78:103518, 2008.

[46] V. A. Kostelecký and N. Russell. Data tables for Lorentz and CPT violation. *Rev. Mod. Phys.*, 83:11–31, 2011.

[47] T. Rosenband, D. B. Hume, P. O. Schmidt, C. W. Chou, A. Brusch, L. Lorini, W. H. Oskay, R. E. Drullinger, T. M. Fortier, J. E. Stalnaker, S. A. Diddams, W. C. Swann, N. R. Newbury, W. M. Itano, D. J. Wineland, and J. C. Bergquist. Frequency Ratio of Al+ and Hg+ Single-Ion Optical Clocks; Metrology at the 17th Decimal Place. *Science*, 319(5871):1808–1812, 2008.

[48] R. M. Godun, P. B. R. Nisbet-Jones, J. M. Jones, S. A. King, L. A. M. Johnson, H. S. Margolis, K. Szymaniec, S. N. Lea, K. Bongs, and P. Gill. Frequency Ratio of Two Optical Clock Transitions in $^{171}Yb^{+}$ and Constraints on the Time Variation of Fundamental Constants. *Phys. Rev. Lett.*, 113:210801, 2014.

[49] N. Huntemann, B. Lipphardt, C. Tamm, V. Gerginov, S. Weyers, and E. Peik. Improved Limit on a Temporal Variation of m_p/m_e from Comparisons of Yb^{+} and Cs Atomic Clocks. *Phys. Rev. Lett.*, 113:210802, 2014.

[50] B. Seiferle, L. von der Wense, P. V. Bilous, I. Amersdorffer, C. Lemell, F. Libisch, S. Stellmer, T. Schumm, C. E. Düllmann, A. Pálffy, and P. G. Thirolf. Energy of the ^{229}Th nuclear clock transition. *Nature*, 573(7773):243–246, 2019.

[51] V. V. Flambaum. Enhanced Effect of Temporal Variation of the Fine Structure Constant and the Strong Interaction in ^{229}Th. *Phys. Rev. Lett.*, 97:092502, 2006.

[52] T. Nicholson, S. Campbell, R. Hutson, G. Marti, B. Bloom, R. McNally, W. Zhang, M. Barrett, M. Safronova, G. Strouse, W. Tew, and J. Ye. Systematic evaluation of an atomic clock at 2×10^{-18} total uncertainty. *Nature communications*, 6:6896, 2015.

[53] N. Huntemann, C. Sanner, B. Lipphardt, C. Tamm, and E. Peik. Single-Ion Atomic Clock with 3×10^{-18} Systematic Uncertainty. *Phys. Rev. Lett.*, 116:063001, 2016.

[54] H. Haken and H. C. Wolf. *Atomic and Quantum Physics*. Springer Berlin Heidelberg, 1984.

[55] V. M. Shabaev. Hyperfine structure of hydrogen-like ions. *Journal of Physics B: Atomic, Molecular and Optical Physics*, 27(24):5825–5832, 1994.

[56] A. Bohr and V. F. Weisskopf. The Influence of Nuclear Structure on the Hyperfine Structure of Heavy Elements. *Phys. Rev.*, 77:94–98, 1950.

[57] E. Y. Korzinin, N. S. Oreshkina, and V. M. Shabaev. Hyperfine splitting of low-lying levels in heavy Li-like ions. *Physica Scripta*, 71(5):464, 2005.

[58] H. F. Beyer and V. P. Shevelko. *Atomic physics with heavy ions*, volume 26. Springer Science & Business Media, 2012.

[59] S. Boucard and P. Indelicato. Relativistic many-body and QED effects on the hyperfine structure of lithium-like ions. *The European Physical Journal D*, 8(1), 2000.

[60] J.-P. Karr. Quantum electrodynamics: Hyperfine puzzle? *Nature Physics*, 13(6): 533, 2017.

[61] L. V. Skripnikov, S. Schmidt, J. Ullmann, C. Geppert, F. Kraus, B. Kresse, W. Nörtershäuser, A. F. Privalov, B. Scheibe, V. M. Shabaev, M. Vogel, and A. V. Volotka. New Nuclear Magnetic Moment of ^{209}Bi: Resolving the Bismuth Hyperfine Puzzle. *Phys. Rev. Lett.*, 120:093001, 2018.

[62] V. M. Shabaev, A. N. Artemyev, V. A. Yerokhin, O. M. Zherebtsov, and G. Soff. Towards a Test of QED in Investigations of the Hyperfine Splitting in Heavy Ions. *Phys. Rev. Lett.*, 86:3959–3962, 2001.

[63] J. R. Crespo López-Urrutia, P. Beiersdorfer, D. W. Savin, and K. Widmann. Direct Observation of the Spontaneous Emission of the Hyperfine Transition $F = 4$ to $F = 3$ in Ground State Hydrogenlike $^{165}Ho^{66+}$ in an Electron Beam Ion Trap. *Phys. Rev. Lett.*, 77:826–829, 1996.

[64] J. R. Crespo López-Urrutia, P. Beiersdorfer, K. Widmann, B. B. Birkett, A.-M. Mårtensson-Pendrill, and M. G. H. Gustavsson. Nuclear magnetization distribution radii determined by hyperfine transitions in the $1s$ level of H-like ions ^{185}Re^{74+} and ^{187}Re^{74+}. *Phys. Rev. A*, 57:879–887, 1998.

[65] P. Beiersdorfer, S. B. Utter, K. L. Wong, J. R. Crespo López-Urrutia, J. A. Britten, H. Chen, C. L. Harris, R. S. Thoe, D. B. Thorn, E. Träbert, M. G. H. Gustavsson, C. Forssén, and A.-M. Mårtensson-Pendrill. Hyperfine structure of hydrogenlike thallium isotopes. *Phys. Rev. A*, 64:032506, 2001.

[66] P. Seelig, S. Borneis, A. Dax, T. Engel, S. Faber, M. Gerlach, C. Holbrow, G. Huber, T. Kühl, D. Marx, K. Meier, P. Merz, W. Quint, F. Schmitt, M. Tomaselli, L. Völker, H. Winter, M. Würtz, K. Beckert, B. Franzke, F. Nolden, H. Reich, M. Steck, and T. Winkler. Ground State Hyperfine Splitting of Hydrogenlike $^{207}Pb^{81+}$ by Laser Excitation of a Bunched Ion Beam in the GSI Experimental Storage Ring. *Phys. Rev. Lett.*, 81:4824–4827, 1998.

[67] J. Ullmann, Z. Andelkovic, C. Brandau, A. Dax, W. Geithner, C. Geppert, C. Gorges, M. Hammen, V. Hannen, S. Kaufmann, et al. High precision hyperfine measurements in Bismuth challenge bound-state strong-field QED. *Nature communications*, 8:15484, 2017.

[68] J. Ketter, T. Eronen, M. Höcker, S. Streubel, and K. Blaum. First-order perturbative calculation of the frequency-shifts caused by static cylindrically-symmetric electric and magnetic imperfections of a Penning trap. *International Journal of Mass Spectrometry*, 358:1 – 16, 2014.

[69] S. Kraemer. Towards Laser Cooling of Beryllium Ions at the Alphatrap Experiment. Master's thesis, Ruprecht-Karls-Universität, Heidelberg, 2017.

[70] S. Sturm, A. Wagner, B. Schabinger, and K. Blaum. Phase-sensitive cyclotron frequency measurements at ultralow energies. *Physical review letters*, 107(14): 143003, 2011.

[71] A. Egl, I. Arapoglou, M. Höcker, K. König, T. Ratajczyk, T. Sailer, B. Tu, A. Weigel, K. Blaum, W. Nörtershäuser, and S. Sturm. Application of the Continuous Stern-Gerlach Effect for Laser Spectroscopy of the $^{40}Ar^{13+}$ Fine Structure in a Penning Trap. *Phys. Rev. Lett.*, 123:123001, 2019.

[72] F. G. Major, V. N. Gheorghe, and G. Werth. *Charged Particle Traps: Physics and Techniques of Charged Particle Field Confinement (Springer Series on Atomic, Optical, and Plasma Physics)*. Springer, Berlin Heidelberg, 2005.

[73] G. Werth, V. N. Gheorghe, and F. G. Major. *Charged Particle Traps II: Applications (Springer Series on Atomic, Optical, and Plasma Physics)*. Springer-Verlag Berlin Heidelberg, 2009. ISBN 978-3-540-92260-5.

[74] L. S. Brown and G. Gabrielse. Geonium theory: Physics of a single electron or ion in a Penning trap. *Reviews of Modern Physics*, 58(1):233–311, 1986.

[75] S. Earnshaw. On the nature of the molecular forces which regulate the constitution of the luminferous ether. *Trans. Camb. Phil. Soc.*, 7:97–112, 1842.

[76] W. Paul and H. Steinwedel. Verfahren zur Trennung bzw. zum getrennten Nachweis von Ionen verschiedener spezifischer Ladung. *German Patent DE944900*, 1956.

[77] Nobelprize.org. The Nobel Prize in Physics 2015, 2019.

[78] H. G. Dehmelt. *Radiofrequency Spectroscopy of Stored Ions I: Storage*, volume 3 of *Advances in Atomic and Molecular Physics*. Academic Press, 1968.

[79] J. S. deGrassie and J. H. Malmberg. Waves and transport in the pure electron plasma. *The Physics of Fluids*, 23(1):63–81, 1980.

[80] J. Ketter, T. Eronen, M. Höcker, M. Schuh, S. Streubel, and K. Blaum. Classical calculation of relativistic frequency-shifts in an ideal Penning trap. *International Journal of Mass Spectrometry*, 361:34 – 40, 2014.

[81] G. Gabrielse, L. Haarsma, and S. Rolston. Open-endcap Penning traps for high precision experiments. *International Journal of Mass Spectrometry and Ion Processes*, 88(2):319 – 332, 1989.

[82] R. S. Van Dyck, D. J. Wineland, P. A. Ekstrom, and H. G. Dehmelt. High mass resolution with a new variable anharmonicity Penning trap. *Applied Physics Letters*, 28(8):446–448, 1976.

[83] S. Sturm. *The g-factor of the electron bound in* $^{28}Si^{13+}$*: The most stringent test of bound-state quantum electrodynamics*. PhD thesis, Johannes Gutenberg-Universität, Mainz, 2011.

[84] A. Weigel. *Detection Electronics Design and First Observation of Bound-Electron Spin Transitions at the ALPHATRAP g-Factor Experiment*. PhD thesis, Ruprecht-Karls-Universität, Heidelberg, 2019.

[85] Oxford Instruments. *Superconducting Magnet System - Assembly and Commissioning Manual*, 1989.

[86] S. Ulmer. *First Observation of Spin Flips with a Single Proton Stored in a Cryogenic Penning Trap*. PhD thesis, Ruprecht-Karls-Universität, Heidelberg, 2011.

[87] J. Verdú. *Ultrapräzise Messung des elektronischen g-Faktors in wasserstoffähnlichen Sauerstoff*. PhD thesis, Johannes Gutenberg-Universität, Mainz, 2003.

[88] T. Sailer. *In preparation*. PhD thesis, Ruprecht-Karls-Universität, Heidelberg, 202x.

[89] L. S. Brown and G. Gabrielse. Precision spectroscopy of a charged particle in an imperfect Penning trap. *Phys. Rev. A*, 25:2423–2425, 1982.

[90] G. Gabrielse. Why Is Sideband Mass Spectrometry Possible with Ions in a Penning Trap? *Phys. Rev. Lett.*, 102:172501, 2009.

[91] M. Höcker. *Precision Mass Measurements at THe-Trap and the FSU trap*. PhD thesis, Ruprecht-Karls-Universität, Heidelberg, 2016.

[92] H. G. Dehmelt and F. L. Walls. "Bolometric" Technique for the rf Spectroscopy of Stored Ions. *Phys. Rev. Lett.*, 21:127–131, 1968.

[93] D. J. Wineland and H. G. Dehmelt. Principles of the stored ion calorimeter. *Journal of Applied Physics*, 46:919–930, 1975.

[94] J. D. Jackson. *Classical electrodynamics*. Wiley, New York, NY, 3rd ed. edition, 1999. ISBN 9780471309321.

[95] D. A. Church and H. G. Dehmelt. Radiative Cooling of an Electrodynamically Contained Proton Gas. *Journal of Applied Physics*, 40(9):3421–3424, 1969.

[96] S. Stahl. *Aufbau eines Experimentes zur Bestimmung elektronischer g-Faktoren einzelner wasserstoffähnlicher Ionen*. PhD thesis, Johannes Gutenberg-Universität, Mainz, 1998.

[97] P. Horowitz and W. Hill. *The Art of Electronics*. Cambridge University Press, New York, NY, USA, 1989. ISBN 0-521-37095-7.

[98] W. M. Itano, J. C. Bergquist, J. J. Bollinger, and D. J. Wineland. Cooling methods in ion traps. *Physica Scripta*, 1995(T59):106, 1995.

[99] J. Ketter. *Theoretical treatment of miscellaneous frequency-shifts in Penning traps with classical perturbation theory*. PhD thesis, Ruprecht-Karls-Universität, Heidelberg, 2015.

[100] M. Schuh. *Simulations of the image charge effect in high-precision Penning traps and the new IGISOL ion buncher*. PhD thesis, Ruprecht-Karls-Universität, Heidelberg, 2015.

[101] M. Schuh, F. Heiße, T. Eronen, J. Ketter, F. Köhler-Langes, S. Rau, T. Segal, W. Quint, S. Sturm, and K. Blaum. Image charge shift in high-precision Penning traps. *Phys. Rev. A*, 100:023411, 2019.

[102] V. Natarajan. *Penning Trap Mass Spectroscopy at 0.1 ppb*. PhD thesis, Massachusetts Institute Of Technology, 1993.

[103] J. Ekin. *Experimental Techniques for Low-Temperature Measurements*. Oxford University Press, 2006.

[104] Anonymous. Minutes of the Philadelphia Meeting December 28, 29, 30, 1926. *Phys. Rev.*, 29:350–373, 1927.

[105] J. B. Johnson. Thermal Agitation of Electricity in Conductors. *Phys. Rev.*, 32: 97–109, 1928.

[106] H. Nyquist. Thermal Agitation of Electric Charge in Conductors. *Phys. Rev.*, 32: 110–113, 1928.

[107] W. Nolting. *Grundkurs Theoretische Physik 1*. Springer Berlin Heidelberg, 2013.

[108] E. A. Cornell, K. R. Boyce, D. L. K. Fygenson, and D. E. Pritchard. Two ions in a Penning trap: Implications for precision mass spectroscopy. *Phys. Rev. A*, 45: 3049–3059, 1992.

[109] E. A. Cornell, R. M. Weisskoff, K. R. Boyce, and D. E. Pritchard. Mode coupling in a Penning trap: π pulses and a classical avoided crossing. *Phys. Rev. A*, 41: 312–315, 1990.

[110] H. G. Dehmelt. Entropy reduction by motional sideband excitation. *Nature*, 262 (5571):777, 1976.

[111] M. Kretzschmar. A quantum mechanical model of Rabi oscillations between two interacting harmonic oscillator modes and the interconversion of modes in a Penning trap. *AIP Conference Proceedings*, 457(1):242–251, 1999.

[112] C. J. Foot. *Atomic physics*. Oxford master series in atomic, optical and laser physics. Oxford University Press, Oxford, 2007.

[113] L. Novotny. Strong coupling, energy splitting, and level crossings: A classical perspective. *American Journal of Physics*, 78(11):1199–1202, 2010.

[114] R. S. Van Dyck, P. Ekstrom, and H. G. Dehmelt. Axial, magnetron, cyclotron and spin-cyclotron-beat frequencies measured on single electron almost at rest in free space (geonium). *Nature*, 262(5571):776, 1976.

[115] R. S. Van Dyck, P. B. Schwinberg, and H. G. Dehmelt. *Electron Magnetic Moment from Geonium Spectra*. Springer US, Boston, MA, 1978. ISBN 978-1-4613-2865-0.

[116] W. Gerlach and O. Stern. Der experimentelle Nachweis der Richtungsquantelung im Magnetfeld. *Zeitschrift für Physik*, 9(1):349–352, 1922.

[117] R. S. Van Dyck, P. B. Schwinberg, and H. G. Dehmelt. Electron magnetic moment from geonium spectra: Early experiments and background concepts. *Phys. Rev. D*, 34:722–736, 1986.

[118] H. G. Dehmelt. Continuous Stern-Gerlach effect: Principle and idealized apparatus. *Proceedings of the National Academy of Sciences*, 83(8):2291–2294, 1986.

[119] N. Hermanspahn, H. Häffner, H.-J. Kluge, W. Quint, S. Stahl, J. Verdú, and G. Werth. Observation of the Continuous Stern-Gerlach Effect on an Electron Bound in an Atomic Ion. *Phys. Rev. Lett.*, 84:427–430, 2000.

[120] H. Häffner, T. Beier, S. Djekić, N. Hermanspahn, H.-J. Kluge, W. Quint, S. Stahl, J. Verdú, T. Valenzuela, and G. Werth. Double Penning trap technique for precise g factor determinations in highly charged ions. *The European Physical Journal D-Atomic, Molecular, Optical and Plasma Physics*, 22(2):163–182, 2003.

[121] C. Böhm, S. Sturm, A. Rischka, A. Dörr, S. Eliseev, M. Goncharov, M. Höcker, J. Ketter, F. Köhler, D. Marschall, J. Martin, D. Obieglo, J. Repp, C. Roux, R. Schüssler, M. Steigleder, S. Streubel, T. Wagner, J. Westermann, V. Wieder, R. Zirpel, J. Melcher, and K. Blaum. An ultra-stable voltage source for precision Penning-trap experiments. *Nuclear Instruments and Methods in Physics Research Section A: Accelerators, Spectrometers, Detectors and Associated Equipment*, 828: 125 – 131, 2016.

[122] G. Werth, J. Alonso, T. Beier, K. Blaum, S. Djekic, H. Häffner, N. Hermanspahn, W. Quint, S. Stahl, J. Verdú, T. Valenzuela, and M. Vogel. Highly charged ions, quantum-electrodynamics, and the electron mass. *International Journal of Mass Spectrometry*, 251(2):152 – 158, 2006.

[123] S. Djekic, J. Alonso, H.-J. Kluge, W. Quint, S. Stahl, T. Valenzuela, J. Verdú, M. Vogel, and G. Werth. Temperature measurement of a single ion in a Penning trap. *The European Physical Journal D - Atomic, Molecular, Optical and Plasma Physics*, 31(3):451–457, 2004.

[124] H. G. Dehmelt, W. Nagourney, and J. Sandberg. Self-excited mono-ion oscillator. *Proceedings of the National Academy of Sciences*, 83(16):5761–5763, 1986.

[125] V. Lagomarsino, G. Manuzio, and G. Testera. Stochastic cooling of the radial motion in a Penning trap. *Phys. Rev. A*, 44:5173–5177, 1991.

[126] S. L. Rolston and G. Gabrielse. Cooling antiprotons in an ion trap. *Hyperfine Interactions*, 44(1):233–245, 1989.

[127] B. R. D'Urso. *Cooling and Self-Excitation of a One-Electron Oscillator*. PhD thesis, Harvard University, 2003.

[128] T. Hänsch and A. Schawlow. Cooling of gases by laser radiation. *Optics Communications*, 13(1):68 – 69, 1975.

[129] D. J. Wineland and H. G. Dehmelt. Proposed 1014 delta upsilon less than upsilon laser fluorescence spectroscopy on t1+ mono-ion oscillator iii. In *Bulletin of the American Physical Society*, volume 20, pages 637–637, 1975.

[130] W. Neuhauser, M. Hohenstatt, P. E. Toschek, and H. G. Dehmelt. Optical-Sideband Cooling of Visible Atom Cloud Confined in Parabolic Well. *Physical Review Letters*, 41:233–236, 1978.

[131] D. J. Wineland, R. E. Drullinger, and F. L. Walls. Radiation-Pressure Cooling of Bound Resonant Absorbers. *Physical Review Letters*, 40:1639–1642, 1978.

[132] W. Neuhauser, M. Hohenstatt, P. E. Toschek, and H. G. Dehmelt. Localized visible Ba^+ mono-ion oscillator. *Phys. Rev. A*, 22:1137–1140, 1980.

[133] D. J. Wineland and W. M. Itano. Spectroscopy of a single Mg^+ ion. *Physics Letters A*, 82(2):75 – 78, 1981.

[134] D. J. Wineland and W. M. Itano. Laser cooling of atoms. *Phys. Rev. A*, 20: 1521–1540, 1979.

[135] D. Leibfried, R. Blatt, C. Monroe, and D. J. Wineland. Quantum dynamics of single trapped ions. *Review of Modern Physics*, 75:281–324, 2003.

[136] W. M. Itano and D. J. Wineland. Laser cooling of ions stored in harmonic and Penning traps. *Phys. Rev. A*, 25:35–54, 1982.

[137] R. E. Drullinger, D. J. Wineland, and J. C. Bergquist. High-resolution optical spectra of laser cooled ions. *Applied physics*, 22(4):365–368, 1980.

[138] H. F. Powell, S. R. de Echaniz, E. S. Phillips, D. M. Segal, and R. C. Thompson. Improvement of laser cooling of ions in a Penning trap by use of the axialization technique. *Journal of Physics B: Atomic, Molecular and Optical Physics*, 36(5): 961–970, 2003.

[139] R. Hendricks, E. Phillips, D. Segal, and R. Thompson. Laser cooling in the Penning trap: an analytical model for cooling rates in the presence of an axializing field. *Journal of Physics B: Atomic, Molecular and Optical Physics*, 41(3):035301, 2008.

[140] H. F. Powell, D. M. Segal, and R. C. Thompson. Axialization of Laser Cooled Magnesium Ions in a Penning Trap. *Phys. Rev. Lett.*, 89:093003, 2002.

[141] E. S. Phillips, R. J. Hendricks, A. M. Abdulla, H. Ohadi, D. R. Crick, K. Koo, D. M. Segal, and R. C. Thompson. Dynamics of axialized laser-cooled ions in a Penning trap. *Phys. Rev. A*, 78:032307, 2008.

[142] D. S. Hall and G. Gabrielse. Electron Cooling of Protons in a Nested Penning Trap. *Phys. Rev. Lett.*, 77:1962–1965, 1996.

[143] D. J. Larson, J. C. Bergquist, J. J. Bollinger, W. M. Itano, and D. J. Wineland. Sympathetic cooling of trapped ions: A laser-cooled two-species nonneutral ion plasma. *Phys. Rev. Lett.*, 57:70–73, 1986.

[144] D. J. Heinzen and D. J. Wineland. Quantum-limited cooling and detection of radio-frequency oscillations by laser-cooled ions. *Phys. Rev. A*, 42:2977–2994, 1990.

[145] M. Bohman, A. Mooser, G. Schneider, N. Schön, M. Wiesinger, J. Harrington, T. Higuchi, H. Nagahama, C. Smorra, S. Sellner, K. Blaum, Y. Matsuda, W. Quint, J. Walz, and S. Ulmer. Sympathetic cooling of protons and antiprotons with a common endcap Penning trap. *Journal of Modern Optics*, 65(5-6):568–576, 2018.

[146] M. Bohman. *in Preparation*. PhD thesis, Ruprecht-Karls-Universität, Heidelberg, 202x.

[147] F. Diedrich, E. Peik, J. M. Chen, W. Quint, and H. Walther. Observation of a Phase Transition of Stored Laser-Cooled Ions. *Phys. Rev. Lett.*, 59:2931–2934, 1987.

[148] L. Gruber, J. P. Holder, J. Steiger, B. R. Beck, H. E. DeWitt, J. Glassman, J. W. McDonald, D. A. Church, and D. Schneider. Evidence for Highly Charged Ion Coulomb Crystallization in Multicomponent Strongly Coupled Plasmas. *Phys. Rev. Lett.*, 86:636–639, 2001.

[149] J. W. Britton, B. C. Sawyer, A. C. Keith, C.-C. J. Wang, J. K. Freericks, H. Uys, M. J. Biercuk, and J. J. Bollinger. Engineered two-dimensional Ising interactions in a trapped-ion quantum simulator with hundreds of spins. *Nature*, 484(7395): 489, 2012.

[150] J. G. Bohnet, B. C. Sawyer, J. W. Britton, M. L. Wall, A. M. Rey, M. Foss-Feig, and J. J. Bollinger. Quantum spin dynamics and entanglement generation with hundreds of trapped ions. *Science*, 352(6291):1297–1301, 2016.

[151] M. Gärttner, J. G. Bohnet, A. Safavi-Naini, M. L. Wall, J. J. Bollinger, and A. M. Rey. Measuring out-of-time-order correlations and multiple quantum spectra in a trapped-ion quantum magnet. *Nature Physics*, 13(8):781, 2017.

[152] R. C. Thompson and D. C. Wilson. The motion of small numbers of ions in a Penning trap. *Zeitschrift für Physik D Atoms, Molecules and Clusters*, 42(4): 271–277, 1997.

[153] D. James. Quantum dynamics of cold trapped ions with application to quantum computation. *Applied Physics B*, 66(2):181–190, 1998.

[154] D. R. Crick, H. Ohadi, I. Bhatti, R. C. Thompson, and D. M. Segal. Two-ion Coulomb crystals of Ca^+ in a Penning trap. *Opt. Express*, 16(4):2351–2362, 2008.

[155] D. R. Crick. *Manipulation of Individual Laser Cooled Ca^+ Ions in Penning Traps.* PhD thesis, Imperial College London, 2009.

[156] J. Alonso, K. Blaum, S. Djekic, H.-J. Kluge, W. Quint, B. Schabinger, S. Stahl, J. Verdú, M. Vogel, and G. Werth. A miniature electron-beam ion source for in-trap creation of highly charged ions. *Review of Scientific Instruments*, 77(3): 03A901, 2006.

[157] F. Köhler, S. Sturm, A. Kracke, G. Werth, W. Quint, and K. Blaum. The electron mass fromg-factor measurements on hydrogen-like carbon $^{12}C^{5+}$. *Journal of Physics B: Atomic, Molecular and Optical Physics*, 48(14):144032, 2015.

[158] B. Franzke. The heavy ion storage and cooler ring project ESR at GSI. *Nuclear Instruments and Methods in Physics Research Section B: Beam Interactions with Materials and Atoms*, 24-25:18 – 25, 1987.

[159] H.-J. Kluge, T. Beier, K. Blaum, L. Dahl, S. Eliseev, F. Herfurth, B. Hofmann, O. Kester, S. Koszudowski, C. Kozhuharov, G. Maero, W. Nörtershäuser, J. Pfister, W. Quint, U. Ratzinger, A. Schempp, R. Schuch, T. Stöhlker, R. Thompson,

M. Vogel, G. Vorobjev, D. Winters, and G. Werth. Chapter 7 HITRAP: A Facility at GSI for Highly Charged Ions. In S. Salomonson and E. Lindroth, editors, *Current Trends in Atomic Physics*, volume 53 of *Advances in Quantum Chemistry*, pages 83 – 98. Academic Press, 2008.

[160] J. R. C. López-Urrutia, J. Braun, G. Brenner, H. Bruhns, C. Dimopoulou, I. N. Draganić, D. Fischer, A. J. G. Martínez, A. Lapierre, V. Mironov, R. Moshammer, R. S. Orts, H. Tawara, M. Trinczek, and J. Ullrich. Progress at the Heidelberg EBIT. *Journal of Physics: Conference Series*, 2:42–51, 2004.

[161] A. J. González Martínez, J. R. Crespo López-Urrutia, D. Fischer, R. Soria Orts, and J. Ullrich. The Heidelberg EBIT: Present results and future perspectives. In *Journal of Physics: Conference Series*, volume 72, page 012001. IOP Publishing, 2007.

[162] P. Micke, S. Kühn, L. Buchauer, J. R. Harries, T. M. Bücking, K. Blaum, A. Cieluch, A. Egl, D. Hollain, S. Kraemer, T. Pfeifer, P. O. Schmidt, R. X. Schüssler, C. Schweiger, T. Stöhlker, S. Sturm, R. N. Wolf, S. Bernitt, and J. R. Crespo López-Urrutia. The Heidelberg compact electron beam ion traps. *Review of Scientific Instruments*, 89(6):063109, 2018.

[163] B. M. Penetrante, J. N. Bardsley, D. DeWitt, M. Clark, and D. Schneider. Evolution of ion-charge-state distributions in an electron-beam ion trap. *Phys. Rev. A*, 43:4861–4872, 1991.

[164] S. Kraemer. Aufbau und Charakterisierung eines Geschwindigkeitsfilters für das ALPHATRAP-Experiment. Bachelor's thesis, Ruprecht-Karls-Universität, Heidelberg, 2014.

[165] A. Egl. Commissioning of the online transfer beamline for the ALPHATRAP experiment. Master's thesis, Ruprecht-Karls-Universität, Heidelberg, 2016.

[166] J. R. C. López-Urrutia. Frequency metrology using highly charged ions. *Journal of Physics: Conference Series*, 723:012052, 2016.

[167] C. Schweiger. Construction and commissioning of a room-temperature electron beam ion trap and development of a wire probe injection system. Master's thesis, Ruprecht-Karls-Universität, Heidelberg, 2017.

[168] T. Sailer. A Laser Ion Source for the Alphatrap Experiment. Master's thesis, Ruprecht-Karls-Universität, Heidelberg, 2017.

[169] C. Smorra, K. Blaum, K. Eberhardt, M. Eibach, J. Ketelaer, J. Ketter, K. Knuth, and S. Nagy. A carbon-cluster laser ion source for TRIGA-TRAP. *Journal of Physics B: Atomic, Molecular and Optical Physics*, 42(15):154028, 2009.

[170] W. C. Wiley and I. H. McLaren. Time-of-Flight Mass Spectrometer with Improved Resolution. *Review of Scientific Instruments*, 26(12):1150–1157, 1955.

[171] M. T. Orešković. Development of a cryogenic vacuum valve and anelectromechanical switch for ALPHATRAP. Master's thesis, Ruprecht-Karls-Universität, Heidelberg, 2014.

[172] H. Liebl. *Applied Charged Particle Optics*. Springer, 2007. ISBN 978-3-540-71924-3.

[173] H. Hirzler. Aufbau und Test der Transferbeamline für das ALPHATRAP Projekt. Bachelor's thesis, Ruprecht-Karls-Universität, Heidelberg, 2014.

[174] C. Smorra, K. Blaum, L. Bojtar, M. Borchert, K. Franke, T. Higuchi, N. Leefer, H. Nagahama, Y. Matsuda, A. Mooser, et al. BASE–the baryon antibaryon symmetry experiment. *The European Physical Journal Special Topics*, 224(16):3055–3108, 2015.

[175] C. Carlberg, H. Borgenstrand, G. Rouleau, R. Schuch, F. Söderberg, I. Bergström, R. Jertz, T. Schwarz, J. Stein, G. Bollen, H.-J. Kluge, and R. Mann. The SMILETRAP facility. *Physica Scripta*, T59:196–202, 1995.

[176] G. Gabrielse and J. Tan. Self-shielding superconducting solenoid systems. *Journal of Applied Physics*, 63(10):5143–5148, 1988.

[177] DuPont de Nemours, Inc. *Vespel*. DuPont de Nemours, Inc., Wilmington, DE, USA, 2019.

[178] Ensinger GmbH. *TECAPEEK ELS nano black*. Ensinger GmbH, Rudolf-Diesel-Straße 8, 71154 Nufringen, Germany, 2019.

[179] F. Heiße, F. Köhler-Langes, S. Rau, J. Hou, S. Junck, A. Kracke, A. Mooser, W. Quint, S. Ulmer, G. Werth, K. Blaum, and S. Sturm. High-Precision Measurement of the Proton's Atomic Mass. *Phys. Rev. Lett.*, 119:033001, 2017.

[180] F. Heiße, S. Rau, F. Köhler-Langes, W. Quint, G. Werth, S. Sturm, and K. Blaum. High-precision mass spectrometer for light ions. *Phys. Rev. A*, 100:022518, 2019.

[181] S. Sturm, G. Werth, and K. Blaum. Electron g-factor determinations in Penning traps. *Annalen der Physik*, 525(8-9):620–635, 2013.

[182] S. Sturm, A. Wagner, M. Kretzschmar, W. Quint, G. Werth, and K. Blaum. g-factor measurement of hydrogenlike $^{28}Si^{13+}$ as a challenge to QED calculations. *Phys. Rev. A*, 87:030501, 2013.

[183] VACUUMSCHMELZE GmbH & Co. KG. *VACOFLUX 50*. VACUUMSCHMELZE GmbH & Co. KG, Grüner Weg 37, 63450 Hanau, Germany, 2019.

[184] TOPTICA Photonics AG. *TA-FHG pro Manual*. TOPTICA Photonics AG, Lochhamer Schlag 19, 82166 Graefelfing, Germany, 2019.

[185] TOPTICA Photonics AG. *BR-199-68A Tunable Diode Lasers*. TOPTICA Photonics AG, Lochhamer Schlag 19, 82166 Graefelfing, Germany, 2017.

[186] E. D. Black. An introduction to Pound–Drever–Hall laser frequency stabilization. *American Journal of Physics*, 69(1):79–87, 2001.

[187] HighFinesse GmbH Laser and Electronic Systems. *Wavelength Meter Ångstrom WS Ultimate 2*. HighFinesse GmbH, Wöhrdstraße 4, 72072 Tübingen, Germany, 2019.

[188] Lasertex Co. Ltd. *Iodine stabilised HeNe laser, LJSC-3-11*. Lasertex Co. Ltd., Ul. Swojczycka 26, 51-501 Wrocław, Poland, 2019.

[189] Sirah Lasertechnik GmbH. *Matisse 2 TS*. Sirah Lasertechnik GmbH, Heinrich-Hertz-Strasse 11, 41516 Grevenbroich, Germany, 2019.

[190] Coherent Inc. *Verdi V18*. Coherent Inc., 5100 Patrick Henry Drive, Santa Clara, CA 95054, USA, 2019.

[191] Coherent Inc. *Wavetrain*. Spectra-Physics, 3635 Peterson Way, Santa Clara, CA 95054, USA, 2019.

[192] Anritsu Corporation. *RF/Microwave Signal Generator, MG3694C*. Anritsu Corporation, 5-1-1 Onna, Atsugi-shi, Kanagawa 243-8555, Japan, 2019.

[193] F. Hahne. in Preparation. Master's thesis, Ruprecht-Karls-Universität, Heidelberg, 2020.

[194] T. Steinsberger. Microwave injection for the ALPHATRAP experiment and developments of the multi-reflection time-of-flight technique of the ISOLTRAP experiment. Master's thesis, Ruprecht-Karls-Universität, Heidelberg, 2018.

[195] Thorlabs Inc. *UV Fused Silica Wedged Windows, AR Coating: 245 - 400 nm, VPWW42-UV*. Thorlabs Inc., 56 Sparta Avenue, Newton, New Jersey 07860, USA, 2019.

[196] A. Kramida, Yu. Ralchenko, J. Reader, and NIST ASD Team. NIST Atomic Spectra Database (ver. 5.7.1), National Institute of Standards and Technology, Gaithersburg, MD., USA, 2019. Online available [2019, November 8]: https://www.nist.gov/pml/atomic-spectra-database.

[197] J. J. Bollinger, J. S. Wells, D. J. Wineland, and W. M. Itano. Hyperfine structure of the $2p^2P_{\frac{1}{2}}$ state in $^9Be^+$. *Phys. Rev. A*, 31:2711–2714, 1985.

[198] T. Andersen, K. A. Jessen, and G. Sørensen. Mean-Life Measurements of Excited Electronic States in Neutral and Ionic Species of Beryllium and Boron. *Phys. Rev.*, 188:76–81, 1969.

[199] D. J. Wineland, J. J. Bollinger, and W. M. Itano. Laser-Fluorescence Mass Spectroscopy. *Phys. Rev. Lett.*, 50:628–631, 1983.

[200] N. Shiga, W. M. Itano, and J. J. Bollinger. Diamagnetic correction to the $^{9}Be^{+}$ ground-state hyperfine constant. *Phys. Rev. A*, 84:012510, 2011.

[201] L. R. Brewer, J. D. Prestage, J. J. Bollinger, W. M. Itano, D. J. Larson, and D. J. Wineland. Static properties of a non-neutral $^{9}Be^{+}$-ion plasma. *Phys. Rev. A*, 38: 859–873, 1988.

[202] J. J. Bollinger, D. J. Heinzen, W. M. Itano, S. L. Gilbert, and D. J. Wineland. A 303-MHz frequency standard based on trapped Be^{+} ions. In *Conference on Precision Electromagnetic Measurements*, pages 264–265, 1990.

[203] D. J. Wineland, J. C. Bergquist, W. M. Itano, and R. E. Drullinger. Double-resonance and optical-pumping experiments on electromagnetically confined, laser-cooled ions. *Opt. Lett.*, 5(6):245–247, 1980.

[204] W. M. Itano and D. J. Wineland. Precision measurement of the ground-state hyperfine constant of $^{25}Mg^{+}$. *Phys. Rev. A*, 24:1364–1373, 1981.

[205] Stahl-Electronics. *3-channel ultra high precision voltage sources UM 1-14 LN*. Stahl-Electronics, Kellerweg 23, 67582 Mettenheim, Germany, 2019.

[206] COMSOL, Inc. *COMSOL Multiphysics*. COMSOL, Inc., 100 District Avenue, Burlington, MA 01803, USA, 2019.

[207] A. Christensen, J. Fajans, and J. Wurtele. Patch Potential Induced Particle Loss in an Antimatter Penning-Malmberg Trap. *Bulletin of the American Physical Society*, 2019.

[208] A. Härter, A. Krükow, A. Brunner, and J. Hecker Denschlag. Long-term drifts of stray electric fields in a Paul trap. *Applied Physics B*, 114(1):275–281, 2014.

[209] M. Harlander, M. Brownnutt, W. Hänsel, and R. Blatt. Trapped-ion probing of light-induced charging effects on dielectrics. *New Journal of Physics*, 12(9):093035, 2010.

[210] The MathWorks, Inc. *MATLAB®*. The MathWorks, Inc., 1 Apple Hill Dr, Natick, MA 01760, USA, 2019.

[211] B. Tu et al., 2020. in preparation.

[212] A. Lapierre, U. D. Jentschura, J. R. Crespo López-Urrutia, J. Braun, G. Brenner, H. Bruhns, D. Fischer, A. J. González Martínez, Z. Harman, W. R. Johnson, C. H. Keitel, V. Mironov, C. J. Osborne, G. Sikler, R. Soria Orts, V. Shabaev, H. Tawara, I. I. Tupitsyn, J. Ullrich, and A. Volotka. Relativistic Electron Correlation, Quantum Electrodynamics, and the Lifetime of the $1s^2 2s^2 2p\ ^2P^o_{3/2}$ Level in Boronlike Argon. *Phys. Rev. Lett.*, 95:183001, 2005.

[213] A. Lapierre, J. R. Crespo López-Urrutia, J. Braun, G. Brenner, H. Bruhns, D. Fischer, A. J. González Martínez, V. Mironov, C. Osborne, G. Sikler, R. Soria Orts, H. Tawara, J. Ullrich, V. M. Shabaev, I. I. Tupitsyn, and A. Volotka. Lifetime measurement of the Ar XIV $1s^2 2s^2 2p\ ^2P^o_{3/2}$ metastable level at the Heidelberg electron-beam ion trap. *Phys. Rev. A*, 73:052507, 2006.

[214] D. von Lindenfels, M. Wiesel, D. A. Glazov, A. V. Volotka, M. M. Sokolov, V. M. Shabaev, G. Plunien, W. Quint, G. Birkl, A. Martin, and M. Vogel. Experimental access to higher-order Zeeman effects by precision spectroscopy of highly charged ions in a Penning trap. *Phys. Rev. A*, 87:023412, 2013.

[215] R. Sánchez, M. Lochmann, R. Jöhren, Z. Andelkovic, D. Anielski, B. Botermann, M. Bussmann, A. Dax, N. Frömmgen, C. Geppert, M. Hammen, V. Hannen, T. Kühl, Y. A. Litvinov, R. López-Coto, T. Stöhlker, R. C. Thompson, J. Vollbrecht, W. Wen, C. Weinheimer, E. Will, D. Winters, and W. Nörtershäuser. Laser spectroscopy measurement of the 2s-hyperfine splitting in lithium-like bismuth. *Journal of Physics B: Atomic, Molecular and Optical Physics*, 50(8), 2017.

[216] R. H. Dicke. The Effect of Collisions upon the Doppler Width of Spectral Lines. *Phys. Rev.*, 89:472–473, 1953.

[217] S. Mavadia, G. Stutter, J. F. Goodwin, D. R. Crick, R. C. Thompson, and D. M. Segal. Optical sideband spectroscopy of a single ion in a Penning trap. *Phys. Rev. A*, 89:032502, 2014.

[218] S. Stahl, J. Alonso, S. Djekic, H.-J. Kluge, W. Quint, J. Verdu, M. Vogel, and G. Werth. Phase-sensitive measurement of trapped particle motions. *Journal of Physics B: Atomic, Molecular and Optical Physics*, 38(3):297–304, 2005.

[219] V. A. Agababaev, D. A. Glazov, A. V. Volotka, D. V. Zinenko, V. M. Shabaev, and G. Plunien. g factor of the [(1s)2(2s)22p]2P3/2 state of middle-Z boronlike ions. *X-Ray Spectrometry*, 2019.

[220] K. König, P. Imgram, J. Krämer, T. Ratajczyk, and W. Nörtershäuser. Relative and absolute limitations of wavelength meters for accurate laser stabilization. Presentation at the 83rd Annual Conference of the DPG and DPG Spring Meeting, Rostock, Germany, 2019.

[221] W. Demtröder. *Laserspektroskopie 2*. Springer Berlin Heidelberg, 2013.

[222] The MathWorks, Inc. *binofit - Binomial parameter estimates*. The MathWorks, Inc., 1 Apple Hill Dr, Natick, MA 01760, USA, 2019.

[223] I. Draganić, J. R. Crespo López-Urrutia, R. DuBois, S. Fritzsche, V. M. Shabaev, R. S. Orts, I. I. Tupitsyn, Y. Zou, and J. Ullrich. High Precision Wavelength Measurements of QED-Sensitive Forbidden Transitions in Highly Charged Argon Ions. *Phys. Rev. Lett.*, 91:183001, 2003.

[224] R. Soria Orts, J. R. Crespo López-Urrutia, H. Bruhns, A. J. González Martínez, Z. Harman, U. D. Jentschura, C. H. Keitel, A. Lapierre, H. Tawara, I. I. Tupitsyn, J. Ullrich, and A. V. Volotka. Zeeman splitting and g factor of the $1s^2 2s^2 2p\ ^2P_{3/2}$ and $^2P_{1/2}$ levels in Ar^{13+}. *Phys. Rev. A*, 76:052501, 2007.

[225] V. Mäckel, R. Klawitter, G. Brenner, J. R. Crespo López-Urrutia, and J. Ullrich. Laser Spectroscopy on Forbidden Transitions in Trapped Highly Charged Ar^{13+} Ions. *Phys. Rev. Lett.*, 107:143002, 2011.

[226] A. N. Artemyev, V. M. Shabaev, I. I. Tupitsyn, G. Plunien, A. Surzhykov, and S. Fritzsche. Ab initio calculations of the $2p_{3/2} - 2p_{1/2}$ fine-structure splitting in boronlike ions. *Phys. Rev. A*, 88:032518, 2013.

[227] Max-Planck-Institut für Kernphysisk. Stored and Cooled Ions Division, Max-Planck-Institut für Kernphysisk, Saupfercheckweg 1, 69117 Heidelberg, Germany, 2020.

[228] M. S. Safronova, V. A. Dzuba, V. V. Flambaum, U. I. Safronova, S. G. Porsev, and M. G. Kozlov. Highly Charged Ions for Atomic Clocks, Quantum Information, and Search for α variation. *Phys. Rev. Lett.*, 113:030801, 2014.

[229] P. O. Schmidt, T. Rosenband, C. Langer, W. M. Itano, J. C. Bergquist, and D. J. Wineland. Spectroscopy Using Quantum Logic. *Science*, 309(5735):749–752, 2005.

[230] I. Klaft, S. Borneis, T. Engel, B. Fricke, R. Grieser, G. Huber, T. Kühl, D. Marx, R. Neumann, S. Schröder, P. Seelig, and L. Völker. Precision Laser Spectroscopy of the Ground State Hyperfine Splitting of Hydrogenlike $^{209}Bi^{82+}$. *Phys. Rev. Lett.*, 73:2425–2427, 1994.

[231] M. Lochmann, R. Jöhren, C. Geppert, Z. Andelkovic, D. Anielski, B. Botermann, M. Bussmann, A. Dax, N. Frömmgen, M. Hammen, V. Hannen, T. Kühl, Y. A. Litvinov, R. López-Coto, T. Stöhlker, R. C. Thompson, J. Vollbrecht, A. Volotka, C. Weinheimer, W. Wen, E. Will, D. Winters, R. Sánchez, and W. Nörtershäuser. Observation of the hyperfine transition in lithium-like bismuth $^{209}Bi^{80+}$: Towards a test of QED in strong magnetic fields. *Phys. Rev. A*, 90:030501, 2014.

[232] P. Beiersdorfer, A. L. Osterheld, J. H. Scofield, J. R. Crespo López-Urrutia, and K. Widmann. Measurement of QED and Hyperfine Splitting in the $2s_{1/2}$- $2p_{3/2}$ X-Ray Transition in Li-like $^{209}Bi^{80+}$. *Phys. Rev. Lett.*, 80:3022–3025, 1998.

[233] J. Vollbrecht, Z. Andelkovic, A. Dax, W. Geithner, C. Geppert, C. Gorges, M. Hammen, V. Hannen, S. Kaufmann, K. König, Y. Litvinov, M. Lochmann, B. Maass, J. Meisner, T. Murboeck, W. Nörtershäuser, R. Sánchez, S. Schmidt, M. Schmidt, M. Steck, T. Stöhlker, R. C. Thompson, J. Ullmann, and C. Weinheimer. Laser spectroscopy of the ground-state hyperfine structure in H-like and Li-like bismuth. *Journal of Physics: Conference Series*, 583:012002, 2015.

[234] S. Schiller and V. Korobov. Tests of time independence of the electron and nuclear masses with ultracold molecules. *Phys. Rev. A*, 71:032505, 2005.

[235] W. Ubachs, J. Koelemeij, K. Eikema, and E. Salumbides. Physics beyond the Standard Model from hydrogen spectroscopy. *Journal of Molecular Spectroscopy*, 320:1 – 12, 2016.

[236] E. G. Myers. CPT tests with the antihydrogen molecular ion. *Phys. Rev. A*, 98: 010101, 2018.

[237] V. I. Korobov, L. Hilico, and J.-P. Karr. Hyperfine structure in the hydrogen molecular ion. *Phys. Rev. A*, 74:040502, 2006.

Acknowledgments

An dieser Stelle möchte ich die Gelegenheit nutzen verschiedenen Leuten zu danken, die mich während meiner Zeit der Promotion begleitet haben.

Lieber Klaus. Deine Begeisterung, Motivation und Arbeitseifer sind einfach unglaublich ansteckend. Das Arbeitsumfeld, das du in deiner Abteilung geschaffen hast, ist wunderbar und einzigartig. Ich schätze es sehr, dass du in dieser Zeit für alle Belange permanent erreichbar warst und man sich einem offenen Ohr und deiner Unterstützung sicher sein kann. Vielen Dank, dass du bereit warst mich zu einem Aufenthalt in die Gruppe von Manas am CQT in Singapur zu schicken. Ebenso bin ich froh, dass du meine Bewerbungen zur Winter School on Trapped Charged Particles in Les Houches und zum 69^{th} Lindau Nobel Laureate Meeting unterstützt und meine Teilnahmen ermöglicht hast. Diese Erfahrungen waren wirklich einzigartig und ich konnte dort wissenschaftlich sehr viel lernen. Danke für dein Vertrauen, Förderung und die schöne Zeit, die ich am Institut verbringen durfte.

Lieber Sven. Auch dir gilt mein allergrößter Dank. Mit dir zusammenarbeiten zu dürfen war mir ein unheimliches Privileg. Dein Zugang zu und das Durchdenken von Problemen nicht nur zur Physik, sondern Themen aller Art ist wirklich eindrucksvoll und einzigartig. Vielen Dank für deine schier endlose Geduld im Erklären von technischen und physikalischen Zusammenhängen, deinen Ausführungen beizuwohnen ist einfach unglaublich interessant und bereichernd. Du bist immer offen für neue Ideen und lässt uns an Entscheidungsprozessen über Alphatrap teilhaben, was wirklich zeigt, dass du die Meinungen deiner Doktoranden und Studenten wertschätzt und respektierst.

Darüber hinaus gilt mein Dank Selim Jochim für die Übernahme der Rolle des Zweitgutachters.

Also I would like to thank Manas Mukherjee and his group for their friendly welcome and hospitality during my stay with them. You gave me valuable insights into the work in a laser lab and your highly interesting field of research. Your support and help was very much appreciated.

Ebenso danke ich Wilfried Nörtershäuser und seinen Doktoranden Tim und Kristian von der TU Darmstadt für ihre Kollaboration und Unterstützung mit dem Spektroskopielasersystem für die Argonmessungen. Eure Hilfestellung in der Bedienung des Lasersystems waren unerlässlich.

Dear *ALPHATRAP*-Team, the current and also the past members with which I had the pleasure to work with. First the postdocs Robert, Martin, Bingsheng and, for short time after their PhD at Alphatrap, Andreas and Ioanna. Thanks for all your hard

work and contributions to the experiment. Everyone of you was always so helpful and supporting. I could learn so much from the experience and knowledge you were always sharing patiently with me. I really liked and enjoyed the time we had together in- and outside the lab. Besondere Dank auch an meinen Doktorandenkollegen Tim. Mit dir zusammenzuarbeiten hat mir jeden Tag aufs neue Spaß bereitet und du hast es immer wieder geschafft mich auf das Neue zu motivieren. Vielen Dank für deine unkomplizierte Art, die gemeinsame Zeit auf Konferenzen und unzählige Gespräche über alles Mögliche. Für die Zukunft wünsche ich dem Team, verstärkt durch Felix als Masterstudent und Fabian als Postdoc alles Gute für die Zukunft und gutes Gelingen.

Ein großer Dank auch an die Kollegen von PENTATRAP, THe und 3He in Heidelberg als auch an die Mitglieder in Mainz bei LIONTRAP und dem Protonexeperiment für ihre tatkräftige Unterstützung und Hilfe am und ums Experiment. Die gemeinsame Zeit die ich auch mit einigen von euch auf diversen Konferenzen, MATS-Tagen oder Workshops verbringen durfte war sehr schön. Auch für eure Experimente und Vorhaben wünsche ich euch nur das Beste für die Zukunft.

Vielen Dank auch an alle anderen Kollegen am MPIK besonders aus den Elektronik- und Mechanikwerkstätten, für ihre große Hilfsbereitschaft und den stets freundlichen Umgang. Auch die Mithilfe von Kollegen aus anderen Abteilungen war großartig. Besonderen Dank vor allem in laserspezifischen Angelegenheiten an Patrick, Nils, Janko und Jan-Hendrik für das Ausleihen von Material und Hilfe.

Meine Freunde in Heidelberg. Die meisten von euch kenne ich seit dem ersten Semester. Für alles Erlebte und Durchgemachte sowie euere bedingungslose Unterstützung und Freundschaft in den letzten zehn Jahren bin ich euch für immer dankbar.

Zu guter Letzt danke ich meiner Familie und vor allem meinen Eltern sowie meiner Schwester und ihrer Familie für ihre selbstlose Unterstützung, Vertrauen und dass ihr immer für mich da seid.

Ale, you are by far the best that could have happened to me during this time. You make me genuinely happy and I am deeply grateful for every day with you. Without your support all this would not have been possible. Thank you for your unconditional support and love.